学 位 論 文

Galaxy Evolution and Cosmic Reionization History
Studied by Subaru Lyman α Emitter Surveys

(すばる望遠鏡ライマンアルファ輝線天体探査による
銀河進化と宇宙再電離史の研究)

平成28年12月博士 (理学) 申請

東京大学大学院理学系研究科
天文学専攻

今 野 彰

Ph.D. Thesis Committee:
Dr. Mamoru Doi (Institute of Astronomy, University of Tokyo); Chair
Dr. Akio Inoue (College of General Education, Osaka Sangyo University)
Dr. Toshitaka Kajino (Theoretical Astronomy Division, National Astronomical Observatory of Japan)
Dr. Nobunari Kashikawa (Optical and Infrared Astronomy Division, National Astronomical Observatory of Japan)
Dr. Kentaro Motohara (Institute of Astronomy, University of Tokyo)
—alphabetical order—

Thesis Adviser:
Dr. Masami Ouchi (Institute for Cosmic Ray Research, School of Science, University of Tokyo)

This thesis is based on the following papers:

Paper I: A. Konno, M. Ouchi, Y. Ono, K. Shimasaku, T. Shibuya, H. Furusawa, K. Nakajima, Y. Naito, R. Momose, S. Yuma, and M. Iye, "Accelerated Evolution of the Lyα Luminosity Function at $z \gtrsim 7$ Revealed by the Subaru Ultra-Deep Survey for Lyα Emitters at $z = 7.3$", The Astrophysical Journal, Volume 797, Issue 1, article id. 16, 15 pp., 2014

Paper II: A. Konno, M. Ouchi, K. Nakajima, F. Duval, H. Kusakabe, Y. Ono, and K. Shimasaku, "Bright and Faint Ends of Lyα Luminosity Functions at $z = 2$ Determined by the Subaru Survey: Implications for AGNs, Magnification Bias, and ISM HI Evolution", The Astrophysical Journal, Volume 823, Issue 1, article id. 20, 17 pp., 2016

Paper III: A. Konno, M. Ouchi, T. Shibuya, et al., "First Results of Subaru/Hyper Suprime-Cam 21 deg^2 Narrowband Survey: Lyα Luminosity Functions at $z = 5.7$ and 6.6" (in preparation), To be submitted to Publications of the Astronomical Society of Japan, 2017

ACKNOWLEDGMENTS

First of all, I would like to express my sincere gratitude to three advisors, Associate Prof. Masami Ouchi, Assistant Prof. Yoshiaki Ono, and Associate Prof. Kazuhiro Shimasaku. I deeply appreciate my thesis adviser, Associate Prof. Masami Ouchi, for his extensive instruction, scientific discussion, and support. I learned from him how to construct the structure of a paper and how to give a presentation effectively as well as how to tackle scientific problems. The research activities with him extended to the outside of our institute. We went to Subaru and Keck observatories in Hawaii, and learned the procedures of observations. We had an opportunity to go to Optical Coatings Japan, which manufactures the HSC narrowband filters, and were able to know how to produce the narrowband filters. Moreover, he gave me a chance of press release in the Subaru Telescope website about our $z = 7.3$ LAE studies. It was difficult for me to write the article that can be easily understood by non-specialists, but this experience is one of the most impressive one in my life. I am grateful to Assistant Prof. Yoshiaki Ono for his invaluable instruction, discussion, and support. He especially taught me the basics of the astronomical research, e.g., data reduction, programming, statistics, and so on. When I struggled with my research activities, he kindly heard my troubles, and advised me what to do. I also appreciate Associate Prof. Kazuhiro Shimasaku for his kind instruction, discussion and support. He taught me the methodology of giving a presentation and the attitude to the research. When I wrote a paper, he gave me objective and valuable comments to improve our paper.

I would like to thank Dr. Takatoshi Shibuya and Dr. Kimihiko Nakajima for completing our work as the thesis. Dr. Shibuya helped me to conduct our LAE studies such as the measurement of the HSC/*NB921* filter transmission, the sample construction of $z \gtrsim 6$ LAEs with Subaru/Suprime-Cam and Hyper Suprime-Cam (HSC) data, and so on. When I worked hard on the thesis, he kindly presented me with snack food. Dr. Nakajima kindly provided the $z = 2.2$ LAE data, which is a key sample in the thesis. I sometimes discussed the data reduction and our LAE studies with him directly, because he belonged to the Kavli Institute for the Physics and Mathematics of the Universe (Kavli IPMU), which is next to our institute. I appreciate Dr. Florent Duval for computing the Lyα radiative transfer with MCLya. I acknowledge Dr. Hisanori Furusawa, Dr. Rieko Momose, Dr. Suraphong Yuma, and Mr. Yoshiaki Naito for the Subaru/Suprime-Cam narrowband and broadband

observation. Especially, Dr. Furusawa and Mr. Naito kindly provided the ultradeep COSMOS z'-band data to study $z = 7.3$ LAEs. I am grateful to Ms. Haruka Kusakabe for providing the $z = 2.2$ LAE data in the CDFS field. I thank Prof. Masanori Iye for the useful discussion and comments in our $z = 7.3$ LAE paper.

I would like to appreciate the Ph.D. thesis refereeing committee, Prof. Mamoru Doi (chair), Associate Prof. Akio Inoue, Associate Prof. Toshitaka Kajino, Associate Prof. Nobunari Kashikawa, and Associate Prof. Kentaro Motohara, for their helpful comments and suggestions, which improve the thesis and our preparing journal paper (Paper III).

I thank Prof. Martin Haehnelt, Dr. Koki Kakiichi, Dr. Lucia Guaita, Prof. Masayuki Umemura, Prof. Kentaro Nagamine, and Dr. Masao Hayashi for useful discussions and comments on our $z = 7.3$ LAE studies. I am grateful to Dr. Tirthanker Roy Choudhury for providing his simulation data of the $x_{\rm HI}$ and $\tau_{\rm el}$ evolution in Figures 7.4 and 7.5. The funds for Suprime-Cam/*NB101* filter, which is a key of our $z = 7.3$ LAE studies, is provided by the Carnegie Observatories and the director, Wendy Freedman. I appreciate Dr. Hajime Sugai, Prof. Daniel Kunth, Prof. Tohru Nagao, Dr. Jorryt Matthee, and Dr. Shun Saito for valuable discussions and comments for our $z = 2.2$ LAE studies.

The HSC collaboration includes the astronomical communities of Japan and Taiwan, and Princeton University. The HSC instrumentation and software development have been conducted by the National Astronomical Observatory of Japan (NAOJ), the Kavli IPMU, the University of Tokyo, the High Energy Accelerator Research Organization (KEK), the Academia Sinica Institute for Astronomy and Astrophysics in Taiwan (ASIAA), and Princeton University. The funds for HSC has been contributed by the FIRST program from Japanese Cabinet Office, the Ministry of Education, Culture, Sports, Science and Technology (MEXT), the Japan Society for the Promotion of Science (JSPS), Japan Science and Technology Agency (JST), the Toray Science Foundation, NAOJ, Kavli IPMU, KEK, ASIAA, and Princeton University.

This thesis makes use of software developed for the Large Synoptic Survey Telescope (LSST). We thank the LSST Project for making their code available as free software at http://dm.lsstcorp.org.

The Pan-STARRS1 Surveys (PS1) have been made possible through contributions of the Institute for Astronomy, the University of Hawaii, the Pan-STARRS Project Office, the Max-Planck Society and its participating institutes, the Max Planck In-

stitute for Astronomy, Heidelberg and the Max Planck Institute for Extraterrestrial Physics, Garching, The Johns Hopkins University, Durham University, the University of Edinburgh, Queen's University Belfast, the Harvard-Smithsonian Center for Astrophysics, the Las Cumbres Observatory Global Telescope Network Incorporated, the National Central University of Taiwan, the Space Telescope Science Institute, the National Aeronautics and Space Administration under Grant No. NNX08AR22G issued through the Planetary Science Division of the NASA Science Mission Directorate, the National Science Foundation under Grant No. AST-1238877, the University of Maryland, and Eotvos Lorand University (ELTE).

I would like to thank Dr. Tomoki Saito, Dr. Mariko Kubo, and Dr. Yi-Kuan Chang, who were the former postdocs in our research group, for the productive discussion and kind supports. I discussed our high-z galaxy studies with them in the internal meeting (Kashiwa meeting). They also helped us to manage the Kashiwa meeting and the open campus events in Kashiwa. I appreciate Dr. Takuya Hashimoto for his dedicated support. I did not collaborate with him on our papers, but we conducted the Subaru/IRCS observations in April 2012. When I was a first-year student of the Master course, I was worried whether or not I would continue my research activity in the Doctor course. I talked to Dr. Hashimoto about that, and he encouraged me in my studies. Thanks to his words, I had a lot of precious experiences in the Doctor course. I am grateful to Dr. Hideaki Fujiwara and Associate Prof. Saeko Hayashi for coordinating and supporting the preparation for our press release. I also thank Dr. Hayato Shimabukuro, Mr. Shintaro Yoshiura, and Associate Prof. Keitaro Takahashi, who invited me to Kumamoto University and gave me an opportunity for the seminars in December 2015.

I am grateful to Prof. Toru Yamada, who is a present professor in the Institute of Space and Astronautical Science, and a former professor in Tohoku University. When I was in the the Bachelor course of the Astronomical Institute in Tohoku University, Prof. Yamada was my supervisor. In seminars with him, I read the textbook "*Astrophysics of Gaseous Nebulae and Active Galactic Nuclei*", and learned the radiative transfer in the interstellar medium of a galaxy and an AGN. He kindly taught me the basic skills of astronomical data analysis, e.g., the usage of IRAF software, the reduction of Suprime-Cam data, statistics, and so on. Through the fruitful discussion in the seminars and meetings with him, I had a great interest in high-z galaxies, and decided to study them in the graduate course.

I appreciate the students in my research group of the Institute for Cosmic Ray Research (ICRR), Mr. Masafumi Ishigaki, Mr. Yuichi Harikane, Mr. Seiji Fujimoto, Mr. Haibin Zhang, Mr. Takashi Kojima, Mr. Yuma Sugahara, Mr. Shiro Mukae, Mr. Ryo Higuchi, and Mr. Miftaful Hilmi, as well as the students in Hongo campus, Mr. Ryota Kawamata, and Mr. Taku Okamura, for active discussions in meetings. Especially, I and Mr. Ishigaki participated in the ICRR spring school as teaching assistants in March 2014, and deeply discussed cosmic reionization history. Mr. Harikane and Mr. Higuchi helped me to analyze the HSC narrowband data.

I am also thankful to my colleagues, Mr. Ryosuke Goto, Dr. Daichi Kashino, and Mr. Rhythm Shimakawa for useful discussions and comments on our LAE studies. I appreciate the participants of young scientist workshop held in Kyoto University in December 2015, Ms. Natsuki Hayatsu, Dr. Takuma Izumi, Mr. Taiki Kawamuro, Mr. Takanobu Kirihara, Mr. Yutaro Kitagawa, Ms. Minju Lee, Ms. Kyoko Onishi, Mr. Toshiki Saito, Mr. Akifumi Seko, and Mr. Daisuke Toyouchi, for their active discussions and encouragement.

I thank Ms. Momoko Ogino, Mr. Yuichiro Tada, Ms. Hiroko Tamazawa, and Mr. Takanao Tsuyuki, who are the former and present members of ICRR. We sometimes went to the sea, and also held drinking parties. Climbing to the top of Mt. Fuji in August 2016 is a good memory for us. I am also thankful to Mr. Tomoyuki Morimitsu, Mr. Takatoshi Sammori, Mr. Yushi Sato, Mr. Shota Shibagaki, and Mr. Takashi Shibata, who are the colleagues of the Bachelor course in Tohoku University, for their encouragement. I appreciate the present and former secretaries of our group, Ms. Takako Idomura, Ms. Chieko Mashima, and Ms. Ritsuko Sato, as well as the ICRR staffs for supporting my graduate student's life. I would like to mention that I always listen music (e.g., Muse, Gorillaz, Blur, Arctic Monkeys, Radiohead, and Dempagumi.inc) in my research activity, and the music is also my emotional mainstay. I acknowledge support from the Japan Society for the Promotion of Science (JSPS) through JSPS Research Fellowships for Young Scientists, as well as support from Hayakawa Fund of the Astronomical Society of Japan and from Foundation for Promotion of Astronomy.

Finally, I would like to express my deep thanks to my parents, Hiroyuki Konno and Mayumi Konno, my grandmother, Kachiko Karakama, and my uncle, Risei Karakama, who induced me to have a great interest in science. I sincerely appreciate their worm caring, financial support, and kind understanding.

ABSTRACT

We investigate galaxy evolution and cosmic reionization history with Lyα luminosity functions (LFs) of Lyα emitters (LAEs) at $z = 2.2$, 5.7, 6.6, and 7.3 identified by the wide-field and ultra-deep Subaru narrowband imaging surveys. In order to construct large samples of the high-z LAEs with a wide range of the Lyα luminosity, we have developed new custom narrowband filters, *NB387* and *NB101*, which are installed on Subaru/Suprime-Cam, and identified LAEs at $z = 2.2$ and 7.3, respectively. Similarly, we have used the Subaru/Hyper Suprime-Cam (HSC) survey data taken with narrowband filters, *NB816* and *NB921*, to detect $z = 5.7$ and 6.6 LAEs, respectively. In the Suprime-Cam and HSC imaging surveys, the effective total areas are ~ 1 and $\sim 10 - 20$ deg^2, respectively. Based on these narrowband images, we identify 3137, 1081, 1273, and 7 LAEs at $z = 2.2$, 5.7, 6.6, and 7.3, respectively. We derive the Lyα LFs from these large LAE samples.

Because the sample of $z = 2.2$ LAEs covers a very wide Lyα luminosity range of $\log L_{\rm Ly\alpha}$ [erg s^{-1}] $= 41.7 - 44.4$, we constrain the faint and bright ends of $z = 2.2$ Lyα LF simultaneously. We find that the best-fit Schechter parameters of the $z = 2.2$ Lyα LF are $L^*_{\rm Ly\alpha} = 5.29^{+1.67}_{-1.13} \times 10^{42}$ erg s^{-1}, $\phi^*_{\rm Ly\alpha} = 6.32^{+3.08}_{-2.31} \times 10^{-4}$ Mpc^{-3}, and $\alpha = -1.75^{+0.10}_{-0.09}$ indicative of a steep faint-end slope. Moreover, we identify a significant hump at the bright end of the $z = 2.2$ Lyα LF ($\log L_{\rm Ly\alpha}$ [erg s^{-1}] > 43.4), and confirm that a majority of the LAEs in the bright-end hump have (a) bright counterpart(s) either in the X-ray, UV, or radio data. This indicates that the bright-end hump is not made by gravitational lensing magnification bias, but AGNs.

We identify LAEs at $z = 5.7$ and 6.6, the epoch of reionization (EoR), with $\log L_{\rm Ly\alpha}$ [erg s^{-1}] $= 43.0 - 44.0$, and determine the bright ends of Lyα LFs at the EoR. Fixing the faint-end slope to $\alpha = -1.8$ that is the best-fit Schechter parameter of our $z = 2.2$ Lyα LF, we find the best-fit Schechter parameters of $L^*_{\rm Ly\alpha} = 8.92^{+0.99}_{-0.89} \times 10^{42}$ erg s^{-1} and $\phi^*_{\rm Ly\alpha} = 2.21^{+0.68}_{-0.50} \times 10^{-4}$ Mpc^{-3} for our $z = 5.7$ Lyα LF, and $L^*_{\rm Ly\alpha} = 6.42^{+0.74}_{-0.59} \times 10^{42}$ erg s^{-1} and $\phi^*_{\rm Ly\alpha} = 2.51^{+0.83}_{-0.68} \times 10^{-4}$ Mpc^{-3} for our $z = 6.6$ Lyα LF. From our $z = 5.7$ and 6.6 Lyα LFs derived with the Subaru/HSC survey data, we find that the Lyα LF at $z = 6.6$ has a significant hump at the bright end ($\log L_{\rm Ly\alpha}$ [erg s^{-1}] > 43.5), while there is no such bright-end hump found at $z = 5.7$. The emergence of the bright-end hump in our $z = 6.6$ Lyα LF implies the existence of AGNs and/or the emergence of large ionized bubbles around bright LAEs.

We have reached $L(\mathrm{Ly}\alpha) = 2.4 \times 10^{42}$ erg s^{-1} (5σ) with our $z = 7.3$ LAE sample, about 4 times deeper than previous Subaru $z \gtrsim 7$ studies, which allows us to reliably investigate the evolution of the Lyα LF at $z \gtrsim 7$ for the first time. For the $z = 7.3$ Lyα LF, we obtain the best-fit Schechter parameters of $L^*_{\mathrm{Ly}\alpha} = 3.23^{+25.0}_{-1.63} \times 10^{42}$ erg s^{-1}, $\phi^*_{\mathrm{Ly}\alpha} = 1.97^{+12.3}_{-1.89} \times 10^{-4}$ Mpc^{-3} with the fixed $\alpha = -1.8$.

We investigate the evolution of Lyα LF at $z = 0 - 6$. With a combination of our and previous studies, the Lyα LF increases from $z \sim 0$ to 3, while there is no evolution of the Lyα LF at $z = 3 - 6$. Estimating the Lyα escape fractions, $f_{\mathrm{esc}}^{\mathrm{Ly}\alpha}$, from the Ly$\alpha$ luminosity densities given by the Lyα LFs, we find the increase of Lyα escape fraction by two orders of magnitude at $z = 0 - 6$. The large $f_{\mathrm{esc}}^{\mathrm{Ly}\alpha}$ increase can be explained neither by the evolution of stellar population nor outflow alone. Our uniform expanding shell models suggest that the typical neutral hydrogen (HI) column density decreases from $N_{\mathrm{HI}} \sim 7 \times 10^{19}$ ($z \sim 0$) to $\sim 1 \times 10^{18}$ cm^{-2} ($z \sim 6$) to explain the large $f_{\mathrm{esc}}^{\mathrm{Ly}\alpha}$ increase. Thus, the physical origins of the large $f_{\mathrm{esc}}^{\mathrm{Ly}\alpha}$ increase will be the decrease of HI density in the interstellar medium from $z \sim 0$ to ~ 6 that enhances dust attenuation for Lyα by resonance scattering.

We confirm that our Lyα LFs decrease from $z = 5.7$ to 6.6, as suggested by previous studies. At $z \sim 7$, the evolution of the Lyα LF is clearly accelerated beyond the measurement uncertainties including cosmic variance. The decreases of Lyα LF at $z = 5.7 - 7.3$ could be explained by cosmic reionization. Based on the Lyα LF evolution at $z = 5.7 - 6.6$ and $5.7 - 7.3$, we estimate the neutral hydrogen fraction of intergalactic medium, x_{HI}, to be $x_{\mathrm{HI}} = 0.0 - 0.3$ and $0.3 - 0.8$ at $z = 6.6$ and 7.3, respectively. From our x_{HI} values, we constrain the cosmic reionization history, and suggest that the cosmic reionization history can explain the Thomson scattering optical depth of free electrons found in cosmic microwave background that is determined by the latest *Planck* 2016 data.

TABLE OF CONTENTS

CHAPTER 1
INTRODUCTION

Lyα luminosity functions (LFs) are important to understand the history of galaxy evolution and cosmic reionization. Lyα LFs are defined as number densities of Lyα emitters (LAEs) as a function of Lyα luminosity. We first describe the recent progresses of studies of Lyα LFs and cosmic reionization in Section 1.1 and 1.2, respectively.

1.1 Observational Studies for Lyα Luminosity Function

1.1.1 Physical Properties of Lyα Emitters

Most LAEs are continuum-faint galaxies with a prominent Lyα emission line. LAEs are young star-forming galaxies, and have a number of early-type stars with a high effective temperature such as O- and B-type stars. These hot young stars emit ionizing photons whose energy is greater than 13.6 eV, and form HII regions in the interstellar medium (ISM) of a galaxy. Lyα photons are produced by recombination of hydrogen following photoionization in the HII regions, and escape from a galaxy through the ISM by resonance scattering of HI. The presence of such galaxies with a strong Lyα emission line in the high-z universe have been originally predicted by Partridge & Peebles (1967). After several decades from the prediction, high-z LAEs are first discovered by Cowie & Hu (1998) and Hu et al. (1998), and a large number of systematic observations have identified to date more than ten thousand LAEs at a wide redshift range of $z \sim 0 - 9$ (e.g., Rhoads et al. 2000; Steidel et al. 2000; Malhotra & Rhoads 2002; Ouchi et al. 2003; Hayashino et al. 2004; Matsuda et al. 2004; Taniguchi et al. 2005; Iye et al. 2006; Kashikawa et al. 2006; Shimasaku et al. 2006; Dawson et al. 2007; Gronwall et al. 2007; Murayama et al. 2007; Ouchi et al. 2008; Finkelstein et al. 2009; Guaita et al. 2010; Adams et al. 2011; Kashikawa et al. 2012; Shibuya et al. 2012; Yamada et al. 2012; Cassata et al. 2015; Oesch et al. 2015; Sobral et al. 2015; Zitrin et al. 2015).

There are two approaches to identify LAEs; photometric and spectroscopic observations. Deep narrowband and broadband imaging surveys are conducted in photometric observations, and find LAEs by the combination of narrowband color excess and ultraviolet (UV) continuum break by the intergalactic medium (IGM) absorption

(e.g., Ouchi et al. 2003; Gronwall et al. 2007; Hu et al. 2010). LAEs are also identified by blank-field spectroscopic survey and follow-up observations of continuum-selected galaxies (i.e., dropout galaxies; e.g., Kashikawa et al. 2011; Cassata et al. 2011; Blanc et al. 2011). Note that most of observational studies define LAEs as galaxies with a rest-frame Lyα equivalent width, EW_0, of $\mathrm{EW}_0 \gtrsim 20$Å.

Based on LAE samples identified by the above-mentioned methods, stellar population and ISM physics of LAEs are revealed by photometric and spectroscopic properties. From analyses of spectral energy distribution (SED) of LAE with multiwavelength data, LAEs are young ($\lesssim$ 100 Myr), less massive ($\sim 10^7 - 10^{10}\ M_\odot$), relatively low star-formation rate (SFR; $\sim 1 - 10\ M_\odot\ \mathrm{yr}^{-1}$), and less dust extinction ($A_V \sim 0$) (e.g., Gawiser et al. 2006; Pirzkal et al. 2007; Lai et al. 2008; Finkelstein et al. 2009; Ono et al. 2010a,b; Guaita et al. 2011; Cowie et al. 2011; Hayes et al. 2014; Kusakabe et al. 2015). Moreover, rest-frame UV and optical spectroscopic observations have revealed the ISM physics of LAEs; high ionization state ($q \sim 10^8 - 10^9$ cm^{-1} s; e.g., Nakajima & Ouchi 2014; Song et al. 2014; Inoue et al. 2016), and strong outflow ($v_{\mathrm{out}} \sim 200$ km s^{-1}; e.g., Hashimoto et al. 2013; Wofford et al. 2013; Erb et al. 2014; Shibuya et al. 2014; Stark et al. 2015; Rivera-Thorsen et al. 2015). Thus, LAEs are thought to be in the early stage of the galaxy evolution.

1.1.2 Bright and Faint Ends of Lyα Luminosity Function

In this subsection, we describe characteristics and previous observational studies of bright and faint ends of Lyα LFs.

Galaxies at the faint end dominate in abundance, and faint-end slopes of Lyα LFs are determined by mass, star-formation activities, physical conditions of ISM, and feedback effects that are key for understanding galaxy evolution (e.g., Santos et al. 2004; Rauch et al. 2008). Although Lyα LFs at various redshifts have been derived by previous observations (see Section 1.1.3), faint-end slopes of the Lyα LFs are poorly constrained in contrast with those of UV LFs (e.g., Reddy & Steidel 2009; Oesch et al. 2010; Hathi et al. 2010; Sawicki 2012; Alavi et al. 2014; Bouwens et al. 2015; Parsa et al. 2016). The faint-end LF slopes are quantified with α, one of the three Schechter function parameters (Schechter 1976), depending on the rest of two parameters, characteristic Lyα luminosity $L^*_{\mathrm{Ly}\alpha}$ and density $\phi^*_{\mathrm{Ly}\alpha}$. With these

parameters, the Schechter function is defined by

$$\begin{aligned}&\phi_{\mathrm{Ly}\alpha}(L_{\mathrm{Ly}\alpha})dL_{\mathrm{Ly}\alpha}\\&= \phi^*_{\mathrm{Ly}\alpha}\left(\frac{L_{\mathrm{Ly}\alpha}}{L^*_{\mathrm{Ly}\alpha}}\right)^{\alpha}\exp\left(-\frac{L_{\mathrm{Ly}\alpha}}{L^*_{\mathrm{Ly}\alpha}}\right)d\left(\frac{L_{\mathrm{Ly}\alpha}}{L^*_{\mathrm{Ly}\alpha}}\right).\end{aligned} \tag{1.1}$$

Previous observational studies report α values for $z = 2-3$ Lyα LFs (e.g., Cassata et al. 2011), assuming a fixed parameter of $L^*_{\mathrm{Ly}\alpha}$ or $\phi^*_{\mathrm{Ly}\alpha}$. There are some studies that constrain α values with no assumptions (e.g., Gronwall et al. 2007; Hayes et al. 2010), but the uncertainties of the Schechter parameters are very large due to the small number of LAEs. Although α is a parameter depending on $L^*_{\mathrm{Ly}\alpha}$ and $\phi^*_{\mathrm{Ly}\alpha}$, so far, none of the observational studies have determined α simultaneously with $L^*_{\mathrm{Ly}\alpha}$ and $\phi^*_{\mathrm{Ly}\alpha}$ due to the small statistics of LAEs whose Lyα luminosity range is limited. In theoretical studies, Gronke et al. (2015) predict the three Schechter function parameters of Lyα LFs at $z = 3-6$, based on the measurements of UV LFs and Lyα EW probability distribution functions (PDFs), and argue that the faint-end slopes of the Lyα LFs are steeper than those of the UV LFs.

Another important characteristics of Lyα LFs is found at the bright end. The bright-end LFs are key for understanding massive-galaxy formation as well as faint active galactic nucleus (AGN; e.g., Gawiser et al. 2006; Ouchi et al. 2008; Zheng et al. 2013). Here, we define faint AGNs as AGNs whose LFs overlap with non-AGN galaxy LFs in the luminosity ranges. The faint AGNs may play an important role in contributing to the UV radiation background (e.g., Giallongo et al. 2015). Faint AGNs are useful probes for quasar fueling lifetime, feedback, and duty cycle (e.g., Hopkins et al. 2006; Fiore et al. 2012). Faint AGNs are spectroscopically identified for most LAEs at $z \sim 3-4$ in the bright-end Lyα LF at $\log L_{\mathrm{Ly}\alpha}$ [erg s^{-1}] $\gtrsim 43.5$ (Gawiser et al. 2006; Ouchi et al. 2008). The bright-end LF includes an interesting physical effect, magnification bias. The magnification bias effect boosts luminosities of high-z galaxies by the gravitational lensing magnification given by foreground massive galaxies, and flattens the bright-end LFs (e.g. Mason et al. 2015; see Figure 3 of Wyithe et al. 2011). In the observational studies, humps of the bright-end Lyα LF are found at $z = 3-7$ (Gawiser et al. 2006; Ouchi et al. 2008; Matthee et al. 2015). In order to estimate the contributions of faint AGNs to the bright end LFs, it is important to investigate the properties of the bright-end galaxies with deep multiwavelength data

such as X-ray, UV, and radio images.

1.1.3 Evolution of Lyα Luminosity Function

It is interesting that how Lyα LFs and Schechter parameters (i.e., $L^*_{\rm Ly\alpha}$, $\phi^*_{\rm Ly\alpha}$, and α) evolve. With the increase of systematic surveys for LAEs at $z \sim 0-8$, the evolution of Lyα LFs at the redshift range is examined intensively. Here, we describe the Lyα LF evolution from $z \sim 0$ to ~ 8 revealed by previous studies.

At a redshift range of $z \sim 0-1$, Lyα emission falls in the UV observing window. It is impossible to detect the Lyα emission at $z \sim 0-1$ with ground-based telescopes because it is out of the observable atmospheric window. Thus, Lyα LFs at $z \sim 0-1$ are investigated by space telescopes such as *GALEX*. From *GALEX* spectra, Deharveng et al. (2008) have successfully found 96 nearby LAEs ($0.2 < z < 0.35$) from five independent fields, whose total survey area is 5.65 deg^2. They derive the Lyα LF at $z \sim 0.3$ based on the low-z LAE sample and find that there is a large increase of Lyα LFs from $z \sim 0.3$ to ~ 3 (see below for details of the $z \sim 3$ Lyα LFs). Following the Deharveng et al.'s study, Cowie et al. (2010, 2011) construct samples of LAEs at $z = 0.195-0.44$ and $0.65-1.25$ larger than that of Deharveng et al. (2008) (see also Barger et al. 2012; Wold et al. 2014). They obtain the Lyα LFs at $z = 0.3$ and 0.9 from these LAE samples, and conclude a significant increase in $L^*_{\rm Ly\alpha}$ at $z = 0.3-0.9$ and a rapid increase in $\phi^*_{\rm Ly\alpha}$ between $z = 0.9$ and ~ 2 (see also Hayes 2015; see Section 1.3 for details of the $z \sim 2$ Lyα LFs).

Lyα LFs at $z \sim 3-6$ are also obtained by previous studies intensively. Most of the studies show that there is no evolution of Lyα LF between $z \sim 3$ to ~ 6 within the errors of measurements (e.g., Kudritzki et al. 2000; Rhoads & Malhotra 2001; Hu et al. 2004; van Breukelen et al. 2005; Ajiki et al. 2006; Shimasaku et al. 2006; Tapken et al. 2006; Dawson et al. 2007; Gronwall et al. 2007; Murayama et al. 2007; Wang et al. 2009; Hu et al. 2010; Zheng et al. 2013; Santos et al. 2016). Some of these measurements suffer field-to-field variance and/or statistical uncertainties due to the small-area and/or shallow survey. To overcome the uncertainties, Ouchi et al. (2008) conduct wide-area (1 deg^2) narrowband surveys for LAE at $z = 3.1, 3.7$ and 5.7 in the Subaru/*XMM-Newton* Deep Survey (SXDS), and conclude no significant evolution of Lyα LFs at $z = 3.1-5.7$.

Previous studies also examine Lyα LFs beyond $z \sim 6$ (e.g., Kashikawa et al. 2006,

2011; Hu et al. 2010; Ouchi et al. 2010; Matthee et al. 2015; see also Nakamura et al. 2011). The evolution of Lyα LFs at $z \sim 6-7$ can be a probe of cosmic reionization, since by the Lyα damping wing absorption, neutral hydrogen in the IGM attenuates Lyα fluxes of LAEs at $z \gtrsim 6$, where cosmic reionization took place (see Section 1.2.4 for details of the Lyα damping wing). Most of these studies show that Lyα LFs at $z = 6.6$ decrease from those of $z = 5.7$.

In summary, previous studies of the Lyα LF evolution reveal that; (1) Lyα LFs increase rapidly from $z \sim 0$ to ~ 3 (e.g., Deharveng et al. 2008), (2) there is no evolution of Lyα LFs at $z \sim 3-6$ (e.g., Ouchi et al. 2008), and (3) Lyα LFs decrease at $z \gtrsim 6$ (e.g., Kashikawa et al. 2006).

1.2 Observational Studies for Cosmic Reionization

1.2.1 Overview of Cosmic Reionization

The universe was born with the Big Bang in a very high temperature and high density state. When the temperature of the universe decreased due to the cosmic expansion, particles (e.g., protons, electrons, and photons) were produced in the universe. At $z \sim 1300$, the number of neutral hydrogen atom increased rapidly by the recombination of protons and electrons, and photons that interacted with electrons decoupled from matter at $z \sim 1100$. The last scattered photons at the redshift are observed as cosmic microwave background (CMB) at present. After the recombination and decoupling phases, early galaxies with first stars formed at $z \sim 10-30$. Because these galaxies included hot and young stars, a large number of high-energy photons were emitted from the galaxies. These photons ionized the neutral IGM surrounding the galaxies, and a number of ionized bubbles were formed in the IGM. A large fraction of neutral hydrogen in the IGM, which was originally produced by the recombination, was ionized by overlapping the ionized bubbles. This event is referred to as cosmic reionization. Because cosmic reionization is related to galaxy formation and IGM physics, it is important to reveal the history and process of cosmic reionization by observations. In order to study the cosmic reionization history, most observational studies define the neutral hydrogen fraction at a given redshift, $x_{\rm HI}$, as a volume-

averaged fraction of neutral hydrogen in the IGM, i.e.,

$$x_{\rm HI} = n_{\rm HI}/n_{\rm H}, \tag{1.2}$$

where $n_{\rm HI}$ and $n_{\rm H}$ are the cosmic-average volume number density of neutral hydrogen and all hydrogen atoms, respectively.

There are three observational approaches to investigate when and how cosmic reionization occurred; (1) absorption lines in spectra of quasars (QSOs), (2) Thomson scattering optical depth, $\tau_{\rm el}$, of CMB, and (3) the Lyα damping wing absorption by IGM neutral hydrogen. We introduce how to constrain the cosmic reionization history by observations from next subsections.

1.2.2 HI *Fraction Obtained by absorption lines in QSO spectra*

We assume that the clumpy neutral IGM are distributed randomly in the line of sight between an observer and a distant QSO. When the observer obtains the spectrum of the QSO, the observed spectrum has a number of absorption lines in their UV continuum bluer than the Lyα line of the QSO. This is because the emission blueward of a QSO Lyα line is attenuated at the wavelength corresponding to that of the redshifted Lyα line in the observed-frame of a clumpy neutral IGM cloud. The set of absorption lines is referred to as Lyman α forest. The larger neutral hydrogen fraction of the IGM is, the more strongly the UV continuum of a QSO are absorbed. Thus, these absorption lines in QSO spectra can be a probe of neutral hydrogen fraction of the IGM.

The optical depth of the uniform neutral IGM for Lyα photons (Gunn-Peterson optical depth) is defined by

$$\tau_{\rm GP}(z) = \frac{\pi e^2}{m_e c}\, f_\alpha\, \lambda_\alpha\, H(z)^{-1}\, n_{\rm HI} \tag{1.3}$$

$$= 4.9 \times 10^5 \left(\frac{\Omega_{\rm m} h^2}{0.13}\right)^{-1/2} \left(\frac{\Omega_{\rm b} h^2}{0.02}\right) \left(\frac{1+z}{7}\right)^{3/2} \left(\frac{n_{\rm HI}}{n_{\rm H}}\right), \tag{1.4}$$

where e is electron charge, m_e is electron mass, c is speed of light, f_α is the oscillator strength of Lyα, λ_α is the wavelength of Lyα, $H(z)$ is Hubble parameter, $\Omega_{\rm m}$ and $\Omega_{\rm b}$ are density parameters of matter and baryon, respectively, and h is dimension-less Hubble constant. From the equation, the QSO spectrum is completely attenuated at

$x_{\rm HI} \gtrsim 10^{-4}$. Thus, it is useful to estimate the neutral hydrogen fraction at the end of epoch of reionization (EoR) by absorption lines in QSO spectra.

Fan et al. (2006) have obtained 19 spectra of QSOs at $5.74 < z < 6.42$, which is found in Sloan Digital Sky Survey (SDSS). They calculate the Gunn-Peterson optical depth from the absorption line in the QSO spectra, and find that the optical depth increases rapidly beyond $z = 5.5$. Based on Equations (1.3) and (1.4), the neutral hydrogen fraction of the IGM at $z \sim 6$ can be estimated. Fan et al. (2006) indicate $x_{\rm HI} \sim 10^{-4}$ at $z \sim 6$ suggesting that cosmic reionization has been completed at this redshift.

1.2.3 Epoch of Reionization Constrained by Cosmic Microwave Background

After the recombination and decoupling phase, CMB photons transmit through the IGM in the universe. When the cosmic reionization is taking place, CMB photons are scattered by electrons which is produced by ionization of neutral hydrogen (i.e., Thomson scattering). CMB is observed as the temperature and polarization fluctuation, and the power spectrum of temperature fluctuation is affected by the Thomson scattering. In the case of instantaneous reionization, which indicates that the neutral IGM became ionized instantaneously at $z = z_{\rm reion}$ (or $t = t_{\rm reion}$), the optical depth of Thomson scattering is explained by

$$\begin{aligned} \tau(z_{\rm reion}) &= \int_{t_{\rm reion}}^{t_0} n_e(t')\sigma_{\rm T} dt' \\ &= \int_0^{z_{\rm reion}} c\langle n_{\rm H}\rangle \sigma_{\rm T} f_{\rm e} Q_{\rm HII}(z') H(z')(1+z')^2 dz', \end{aligned} \tag{1.5}$$

where t_0 is the present time (i.e., $z = 0$), $n_e(t)$ is number density of electron, $\sigma_{\rm T}$ is Thomson scattering cross section, $\langle n_{\rm H}\rangle (= X_{\rm p}\Omega_{\rm b}\rho_{\rm c})$ is comoving number density of hydrogen atoms ($X_{\rm p}$ is the primordial mass-fraction of hydrogen, $\rho_{\rm c} \equiv 3H_0^2/(8\pi G)$ is the critical density, H_0 is Hubble constant at $z = 0$, G is the gravitational constant), $f_{\rm e}$ is the number of free election per a hydrogen nucleus in the ionized IGM, and $Q_{\rm HII}(z)$ is ionized hydrogen fraction in the IGM (see also Robertson et al. 2013). The temperature fluctuation at the recombination phase reduces by $\exp(-\tau)$, and the power spectrum is attenuated by $\exp(-2\tau)$. Moreover, because this attenuation

cannot affect the power spectrum beyond the horizon at the EoR, the attenuation can be occurred at the small angular scale (i.e., large multipole moment) of the power spectrum. Thus, the Thomson scattering optical depth and the redshift at which cosmic reionization took place can be measured from the observed temperature fluctuation power spectrum of CMB.

Because CMB photons are polarized by the Thomson scattering, electrons in the ionized IGM can also affect the polarization angular power spectrum or the temperature-polarization cross-power spectrum. In that case, a peak of the angular power spectra emerges at a multipole moment corresponding to the horizon length at the EoR. Thus, one can examine when cosmic reionization has took place based on the position of the peak in the angular power spectra.

Measurements of the polarization of CMB by *WMAP* constrain the optical depth of Thomson scattering, $\tau_{\rm el} = 0.081 \pm 0.012$, and indicate that the universe would be reionized at $z_{\rm re}^{\rm inst} = 10.1 \pm 1.0$ for the case of instantaneous reionization (Hinshaw et al. 2013; Bennett et al. 2013). Recent observational studies with *Planck* show that the electron scattering optical depth is $\tau_{\rm el} = 0.058 \pm 0.009$, and that the instantaneous reionization redshift is $z_{\rm re}^{\rm inst} = 8.1 \pm 0.9$ (Planck Collaboration et al. 2016).

1.2.4 HI *Fraction Estimated with the Lyα Damping Wing*

The Lyα damping wing is the broad absorption at the wavelength of Lyα caused by quantum-mechanical effect. Here, we formularize the Lyα damping wing profile following Miralda-Escudé (1998) and Totani et al. (2006). We assume that one observes an object at $z = z_{\rm source}$, and there exists the homogeneous neutral IGM with $x_{\rm HI}$ at $z_{\rm IGM,l} < z < z_{\rm IGM,u}$ ($\lesssim z_{\rm source}$) between the observer and the object. The scattering cross section of the Lyα resonance line is given by the Lorentzian profile;

$$\sigma_\alpha(\nu) = \frac{3\lambda_\alpha^2}{8\pi} f_\alpha \, \Lambda_{{\rm cl},\alpha} \frac{\Lambda_\alpha \, (\nu/\nu_\alpha)^4}{4\pi^2 \, (\nu - \nu_\alpha)^2 + (\Lambda_\alpha^2/4) \, (\nu/\nu_\alpha)^6}, \tag{1.6}$$

where λ_α, ν_α ($= c/\lambda_\alpha$) are the Lyα wavelength (1215.668Å) and frequency, respectively, $f_\alpha = 0.4162$ is the absorption oscillator strength, $\Lambda_{{\rm cl},\alpha} = (8\pi^2 e^2)/(3 m_e c \lambda_\alpha^2)$ is the classical damping constant of the Lyα resonance, $\Lambda_\alpha = 3 \, (g_u/g_l)^{-1} f_\alpha \Lambda_{{\rm cl},\alpha}$ is the damping constant. Note that for Lyα, the ratio of the statistical weights for the upper level to lower level is $g_u/g_l = 3$. The scattering cross section of the Lyα resonance

line has a broad distribution as a function of frequency, and thus, the Lyα resonance scattering can be occurred at a wavelength redder than that of Lyα. Because we are interested in the profile far from the Lyα wavelength (i.e., $|\nu - \nu_\alpha| \gg \Lambda_\alpha$), the second term in the denominator of Equation (1.6) can be negligible. The optical depth of the neutral IGM at a wavelength of $\lambda_{\rm obs} > (1 + z_{\rm IGM,u})\lambda_\alpha$ is given by

$$\tau_{\rm IGM}(\lambda_{\rm obs}) = \int_{z_{\rm IGM,l}}^{z_{\rm IGM,u}} dz\, c \left(\frac{dz}{dt}\right)^{-1} n_{\rm H,0}(1+z)^3 \sigma_\alpha[(1+z)\nu_{\rm obs}], \tag{1.7}$$

where $n_{\rm H,0}$ is the comoving number density of neutral hydrogen in the IGM. Based on Equations (1.6) and (1.7), we obtain

$$\tau_{\rm IGM}(\lambda_{\rm obs}) = \frac{R_\alpha\ \tau_{\rm GP}(x_{\rm HI}, z_{\rm source})}{\pi} \left(\frac{1+z_{\rm obs}}{1+z_{\rm source}}\right)^{3/2} \times \left[I\left(\frac{1+z_{\rm IGM,u}}{1+z_{\rm obs}}\right) - I\left(\frac{1+z_{\rm IGM,l}}{1+z_{\rm obs}}\right) \right], \tag{1.8}$$

where $(1 + z_{\rm obs})$ and R_α are defined by $(1 + z_{\rm obs}) \equiv \lambda_{\rm obs}/\lambda_\alpha$ and $R_\alpha \equiv \Lambda_\alpha\lambda_\alpha/(4\pi c)$, respectively. The Gunn-Peterson optical depth, $\tau_{\rm GP}(x_{\rm HI}, z_{\rm source})$, in Equation (1.8) is given by

$$\tau_{\rm GP}(x_{\rm HI}, z) = x_{\rm HI}\ \frac{3 f_\alpha \Lambda_{{\rm cl},\alpha}\ \lambda_\alpha^3\ \rho_c\ \Omega_{\rm b}(1-Y_{\rm p})}{8\pi\ m_{\rm p}\ H_0\ \Omega_{\rm m}^{1/2}}(1+z)^{3/2}, \tag{1.9}$$

where $Y_{\rm p}$ is the primordial helium mass fraction in the total cosmic baryon, and $m_{\rm p}$ is the proton mass. The function $I(x)$ in Equation (1.8) is defined by

$$I(x) = \frac{x^{9/2}}{1-x} + \frac{9}{7}x^{7/2} + \frac{9}{5}x^{5/2} + 3x^{3/2} + 9x^{1/2} - \frac{9}{2}\ln\frac{1+x^{1/2}}{1-x^{1/2}}. \tag{1.10}$$

From Equation (1.8), one obtains a spectrum of the object at $z = z_{\rm source}$, which is attenuated by $\exp(-\tau_{\rm IGM})$, and can estimate the neutral hydrogen fraction of the IGM at $z_{\rm IGM,l} < z < z_{\rm IGM,u}$ from the spectrum.

The $x_{\rm HI}$ estimate with the Lyα damping wing is adopted in spectra of the gamma-ray bursts (GRBs) and QSOs. Totani et al. (2006) estimate $x_{\rm HI}$ with the shape of Lyα damping wing absorption found in the optical afterglow spectrum of GRB 050904 at $z \sim 6.3$, and obtain $x_{\rm HI} < 0.17$ (68% confidence level) at this redshift. In the recent study with a GRB, the unprecedentedly bright optical afterglow spectrum of GRB

130606A at $z \sim 5.9$ suggests $x_{\rm HI} = 0.1 - 0.5$ (Totani et al. 2014), which shows relatively high neutral hydrogen fraction at $z \sim 6$ (see Section 1.2.2). Mortlock et al. (2011) report observations of a QSO at $z = 7.085$, ULAS J1120+0641, and claim $x_{\rm HI} > 0.1$ at this redshift from the near-zone transmission profile. Bolton et al. (2011) use radiative transfer simulations with model absorptions of the inhomogeneous IGM around ULAS J11201+0641, and obtain $x_{\rm HI} \gtrsim 0.1$.

The neutral hydrogen fraction of the IGM would be constrained by the evolution of the Lyα LF at the epoch of $x_{\rm HI} \sim 0.1 - 1.0$ (Malhotra & Rhoads 2004; Hu et al. 2005; Iye et al. 2006; Kashikawa et al. 2006, 2011; Ota et al. 2008, 2010; Ouchi et al. 2010; Shibuya et al. 2012; see also Section 1.1.3), since the Lyα damping wing of neutral hydrogen in the IGM around galaxies attenuates Lyα photons from the galaxies significantly. The evolution of the Lyα luminosity density (LD) between $z = 5.7$ and 6.6 suggests $x_{\rm HI} = 0.2 \pm 0.2$ at $z = 6.6$ that is corrected for the intrinsic UV luminosity evolution effect with the cosmic star formation rate density change (Ouchi et al. 2010). A Lyα emitting fraction of UV-continuum selected galaxies is similarly used for a probe of cosmic reionization. Previous studies report that the Lyα emitting fraction of Lyman break galaxies (LBGs) decreases from $z \sim 6$ to 7 in contrast to the increase of the Lyα emitting fraction from $z \sim 3$ to 6, and claim that the neutral hydrogen fraction increases from $z \sim 6$ to 7. (Pentericci et al. 2011; Schenker et al. 2012; Ono et al. 2012; Treu et al. 2012; Caruana et al. 2012, 2014; Pentericci et al. 2014; Schenker et al. 2014). By the comparison with theoretical models, these studies suggest $x_{\rm HI} \gtrsim 0.5$ at $z \sim 7$.

1.3 Open Questions about Lyα Luminosity Functions

As we overview the observational characteristics of Lyα LFs in Section 1.1.2, the shape of Lyα LFs has been poorly constrained. For instance, there is no studies that the faint-end slope of Lyα LFs, α, is strongly determined with no assumptions. Furthermore, it has not been clearly concluded whether or not (faint) AGNs are dominated in the bright end of Lyα LF.

The intermediate redshift range of $z \sim 2-3$ is the best for investigating faint- and bright-end Lyα LFs. This is because $z \sim 2-3$ is the lowest redshift range where Lyα emission falls in the optical observing window, which allows us to identify very faint LAEs as well as a large number of bright LAEs by fast optical surveys. Moreover,

because the number densities of AGNs peak at $z \sim 2-3$, the effect of faint AGNs would clearly appear at the Lyα LF bright end. By these reasons, in the past few years, various surveys have been conducted to study LAEs at $z \sim 2-3$. Although the Lyα LFs at $z \sim 3$ are well determined (e.g. Gronwall et al. 2007; Ouchi et al. 2008), those at $z \sim 2$ are derived with uncertainties larger than those at $z \sim 3$ due to difficulties of $\mathcal{U}$-band observations at $\sim 3000-4000$Å to which Lyα emission lines of $z \sim 2$ objects are redshifted. Thus, the evolution of Lyα LFs from $z \sim 2$ to 3 is under debate. Nilsson et al. (2009) first claim that there is a possible evolution of LAE number densities between $z = 2.25$ and ~ 3 albeit with the large uncertainties originated from the small sample. Subsequent studies have identified $z \sim 2$ LAEs by narrowband imaging and spectroscopic observations, and discussed the evolution of Lyα LFs and the integrations of Lyα LFs, LDs, at $z = 2-3$. Cassata et al. (2011) and Blanc et al. (2011) have carried out blank-field spectroscopy for LAEs at $2 < z < 6.6$ and $1.9 < z < 3.8$, respectively, and concluded no evolution of the Lyα LDs from $z = 2$ to 3. On the other hand, Ciardullo et al. (2012) show that the Lyα LF evolves from $z = 2.1$ to 3.1 significantly by the narrowband imaging surveys in ECDF-S (see also Guaita et al. 2010). Because the $z \sim 2$ LAE samples of these studies are limited in the LAE numbers (that are equal to or less than several hundreds), the survey areas (less than 1000 arcmin^2), and the Lyα luminosity dynamic range (that is a factor of ~ 10), these discrepancies may be raised by the sample variances and the differences of Lyα luminosity coverages.

Evolution of Lyα LFs at $z \lesssim 2-3$ is also discussed extensively. Deharveng et al. (2008) claim that there is a substantial drop in the Lyα LFs from $z \sim 3$ to ~ 0.3 (see also Cowie et al. 2010, 2011; Barger et al. 2012; Wold et al. 2014). A similar evolutionary trend can be found in the Lyα escape fraction at $z \sim 0-6$ (e.g., Hayes et al. 2011, Blanc et al. 2011, Zheng et al. 2013) that is defined by the ratio of the observed to the intrinsic Lyα fluxes. The physical origin of the rapid evolution may be dust attenuation within galaxies. From the observations of UV-continuum slope of LBGs, dust extinction, $E(B-V)$, decreases toward higher redshift (e.g., Bouwens et al. 2015). Because the Lyα escape fraction clearly depends on $E(B-V)$ (e.g., Kornei et al. 2010; Atek et al. 2014), dust extinction would explain the rapid evolution of the Lyα LF and Lyα escape fraction. To understand the major physical mechanisms related to the Lyα escape processes at high-z and its dependence on redshift, determining Lyα LFs at $z \sim 2$ is important.

While we describe the Lyα LF evolution at $0 < z < 7$ in Section 1.1.3, a large number of systematic narrowband imaging surveys have been carried out for LAEs at $z \sim 7$ (Iye et al. 2006; Ota et al. 2008, 2010; Shibuya et al. 2012) and beyond $z \sim 8$ (Willis & Courbin 2005; Cuby et al. 2007; Willis et al. 2008; Sobral et al. 2009; Hibon et al. 2010; Tilvi et al. 2010; Clément et al. 2012; Krug et al. 2012; Matthee et al. 2014). In these studies, it is under debate whether the Lyα LF evolves from $z = 6.6$ or not, while no evolution of the Lyα LF in $z = 3.1 - 5.7$ (Ouchi et al. 2008) and a decrease from $z = 5.7$ to 6.6 (Kashikawa et al. 2006, 2011; Ouchi et al. 2010; Hu et al. 2010) have been identified. Hibon et al. (2010), Tilvi et al. (2010) and Krug et al. (2012) conclude that there is no evolution of the Lyα LF from $z = 6.6$ to 7.7. On the other hand, Clément et al. (2012) place the upper limit on the Lyα LF based on their result of no detection of $z = 7.7$ LAE, and rule out no evolution of the Lyα LF in $z = 6.6 - 7.7$. Moreover, the observations for $z = 7.0$ and 7.3 LAEs have been conducted by Ota et al. (2010) and Shibuya et al. (2012), and these studies find that the number density and the Lyα LD decrease from $z = 5.7$ to $7.0 - 7.3$. However, they cannot clearly find whether the Lyα LF evolves from $z = 6.6$ to $7.0 - 7.3$ due to the large uncertainties of their LF measurements. Their large uncertainties are originated from the relatively shallow imaging that just reaches the bright Lyα luminosity limit of $L(\mathrm{Ly}\alpha) \sim 10^{43}$ erg s^{-1}. The contradicted results of the Lyα LF evolution may be caused by small statistics and systematic uncertainties such as contamination and cosmic variance. To reliably investigate the evolution of the Lyα LF at $z \gtrsim 7$, one needs an ultra-deep narrowband imaging survey in large areas down to the Lyα luminosity limit comparable to those of $z \leq 6.6$ LAE samples.

In Section 1.2, we describe some observational results to constrain cosmic reionization history with QSOs, CMB, GRBs, and LAEs. However, the history of cosmic reionization has been poorly understood. Although the CMB observations rule out the instantaneous reionization at a late epoch, it is difficult to understand how the reionization proceeds in the cosmic history. As illustrated in Figure 23 of Ouchi et al. (2010), there are large uncertainties of the x_{HI} estimates from the previous observational studies, and one cannot distinguish between various models of reionization history. A redshift of ~ 7 is the observational limit of optical instruments that enable us to conduct a deep and wide-field imaging survey. The differences of reionization history in models are relatively large at $z \gtrsim 7$ (see Figure 23 of Ouchi et al. 2010). Because the Gunn-Peterson trough in QSO spectra will be saturated at $x_{\mathrm{HI}} \gtrsim 10^{-4}$,

the $x_{\rm HI}$ estimate with Gunn-Peterson trough is not useful at $z \gtrsim 7$, where $x_{\rm HI} \gg 10^{-4}$. The Lyα damping wing appeared in QSOs and GRB afterglow will be useful to constrain the $x_{\rm HI}$ value at $z \gtrsim 7$. However, the number density of QSOs and the event rate of GRBs are quite small at $z \gtrsim 7$. On the other hand, previous studies have found LAEs in such high-z universe, and the number of LAEs is larger than those of QSOs and GRBs at $z \gtrsim 7$. Thus, a measurement of the Lyα LF at $z \sim 7$ with a good statistical accuracy is useful to constrain $x_{\rm HI}$ near the observational limit and to address this issue of cosmic reionization history. Moreover, even at $z \lesssim 7$, the $x_{\rm HI}$ constraint from the Lyα LF evolution is poor due to the small statistics of LAEs. As described in Section 1.2.4, Ouchi et al. (2010) estimate $x_{\rm HI} = 0.2 \pm 0.2$ at $z = 6.6$ based on 207 LAEs at the redshift. To understand the cosmic reionization history accurately, it is also important to constrain the $x_{\rm HI}$ value with $z \sim 6-7$ LAE samples larger than those of previous studies, and to check the consistency between the $x_{\rm HI}$ evolution and the Thomson scattering optical depth of CMB.

In summary, we have three open questions about galaxy evolution;

- The shape of Lyα LFs is poorly determined. How steep are the faint ends of Lyα LFs? Is the bright end of Lyα LFs dominated by AGN?
- The evolution of Lyα LF is not clearly concluded not only at $z = 2-3$ but also at $z \gtrsim 7$.
- What is the physical mechanisms of the Lyα LF evolution at $z = 0-6$?

and two questions about cosmic reionization;

- What is the neutral hydrogen fraction $x_{\rm HI}$ at $z \gtrsim 7$?
- How do $x_{\rm HI}$ values evolve at $z \sim 6-7$? Is the cosmic reionization history extended? Is the $x_{\rm HI}$ evolution consistent with the Thomson scattering optical depth of CMB?

1.4 Goals of the Thesis

To address the issues mentioned in Section 1.3, one needs wide-area and deep narrow-band imaging survey to construct LAE samples larger than those of previous studies,

and to derive Lyα LFs with the wide Lyα luminosity range. We have carried out deep large-area narrowband imaging surveys with Subaru/Suprime-Cam (Miyazaki et al. 2002) for $z = 2.2$ and 7.3 LAEs, and with Subaru/Hyper Suprime-Cam (HSC; Miyazaki et al. 2012) for $z = 5.7$ and 6.6 LAEs. Because $z \sim 2$ is the lowest redshift range where Lyα emission fall in the optical observing window, we can identify very faint LAEs as well as a large number of bright LAEs by fast optical surveys. Based on the $z = 2.2$ LAE sample, we examine the bright- and faint-end of Lyα LF, and the evolution of Lyα LF at $z = 2 - 3$. Furthermore, from the Lyα LFs derived by the samples of $z = 2.2$ and 5.7 LAEs, we investigate the evolution of Lyα LFs at $z \sim 0 - 6$ to study physical mechanisms of the Lyα LF evolution. As mentioned in Section 1.2.4, the neutral hydrogen fraction at $z = 6.6$ is $x_{\rm HI} = 0.2 \pm 0.2$ constrained by the evolution of Lyα LFs at $z = 5.7 - 6.6$ (Ouchi et al. 2010). The uncertainty of the neutral hydrogen fraction is dominated by the errors of the Lyα LF measurements due to the small statistics of LAEs. Thus, to reduce the uncertainties, one needs narrowband images wider than previous studies by using HSC whose field-of view (FoV) is about seven times larger than that of Suprime-Cam. For observations of $z = 7.3$ LAEs, we have developed a new custom narrowband filter, *NB101*. The filter transmission of *NB101* is centered at $\lambda_{\rm c} = 10095$Å and *NB101* is designed to have a narrow and sharp FWHM of $\Delta\lambda = 90$Å. The *NB101* filter identifies LAEs in the redshift range of $z = 7.302 \pm 0.037$. We show the filter response curve of our *NB101* in Figure 1.1. Note that there is a Suprime-Cam narrowband filter, *NB1006*, at a similar wavelength (Shibuya et al. 2012). The *NB1006* filter has a central wavelength of $\lambda_{\rm c} = 10052$Å slightly bluer than that of our *NB101* and an FWHM of $\Delta\lambda = 214$Å about 2-3 times broader than that of our *NB101*. Similarly, there is another Suprime-Cam narrowband filter of *NB973* targeting $z = 7.0$ LAEs with a central wavelength of $\lambda_{\rm c} = 9755$Å and an FWHM of $\Delta\lambda \sim 200$Å (Iye et al. 2006; Ota et al. 2008, 2010) that is also much broader than the FWHM of our *NB101* filter. Since our *NB101* filter has a significantly narrower/shaper FWHM than the *NB1006* and *NB973* filters, our *NB101* filter is more sensitive to an emission line than the *NB1006* and *NB973* filters. Although the survey volume is smaller for *NB101* than for *NB1006* and *NB973*, the line sensitivity is more important for the observational studies of $z \gtrsim 7$ sources whose LF's exponential edge is near the observational limit. At $z = 7.3$, our *NB101* filter allows us to reach a Lyα flux limit faster than the previous Shibuya et al.'s *NB1006* surveys by $\sim 160\%$. Thus, we can reach the Lyα luminosity limit of LAEs much

fainter than the previous Subaru studies for $z \sim 7$ LAEs. From the samples of LAEs at $z = 5.7$, 6.6, and 7.3, we estimate the $x_{\rm HI}$ values at $z = 6.6$ and 7.3, and constrain the cosmic reionization history.

The outline of the thesis is as follows. We describe the details of our observations with Suprime-cam (for LAEs at $z = 2.2$ and 7.3) and HSC (for LAEs at $z = 5.7$ and 6.6) in Chapter 2. We construct LAE samples at $z = 2.2$, 5.7, 6.6, and 7.3 in Chapter 3. The sample contains 3,137 LAEs at $z = 2.2$ with a wide Lyα luminosity range of $41.7 \leqslant \log L_{{\rm Ly}\alpha}$ [erg s^{-1}] $\leqslant 44.4$, and enables us to examine the faint+bright ends and the evolution of Lyα LFs. Using the sample of $z = 7.3$ LAEs, we derive the Lyα LF with accuracies significantly better than those of previous $z \gtrsim 7$ studies. We derive the Lyα LFs at $z = 2.2$, 5.7, 6.6, and 7.3, and compare the LFs with those of previous studies in Chapter 4. We investigate the Lyα LF and LD evolution from $z \sim 0$ to ~ 7 in Chapter 5 and 6, respectively. We finally discuss the physical origins of the bright-end of our Lyα LFs, and the Lyα LF and LD evolution at $z \sim 0-7$ in Chapter 7. We also estimate the neutral hydrogen fraction at $z = 6.6$ and 7.3, and discuss the cosmic reionization history with the constraints of the electron scattering optical depth measurements of CMB in this chapter. We give a summary of the thesis in Chapter 8.

1.5 Magnitude Systems and Cosmological Parameters

Throughout this paper, we adopt AB magnitudes (Oke 1974):

$$m = -2.5 \log f_\nu - 48.60, \tag{1.11}$$

where m is the magnitude of objects and f_ν is the flux of objects in units of erg s^{-1} cm^{-2} Hz^{-1}.

The cosmological parameter set in this thesis is (h, $\Omega_{\rm m}$, Ω_Λ, σ_8) = (0.7, 0.3, 0.7, 0.8), which is consistent with the nine-year *WMAP* and *Planck* 2015 results (Hinshaw et al. 2013; Planck Collaboration et al. 2015).

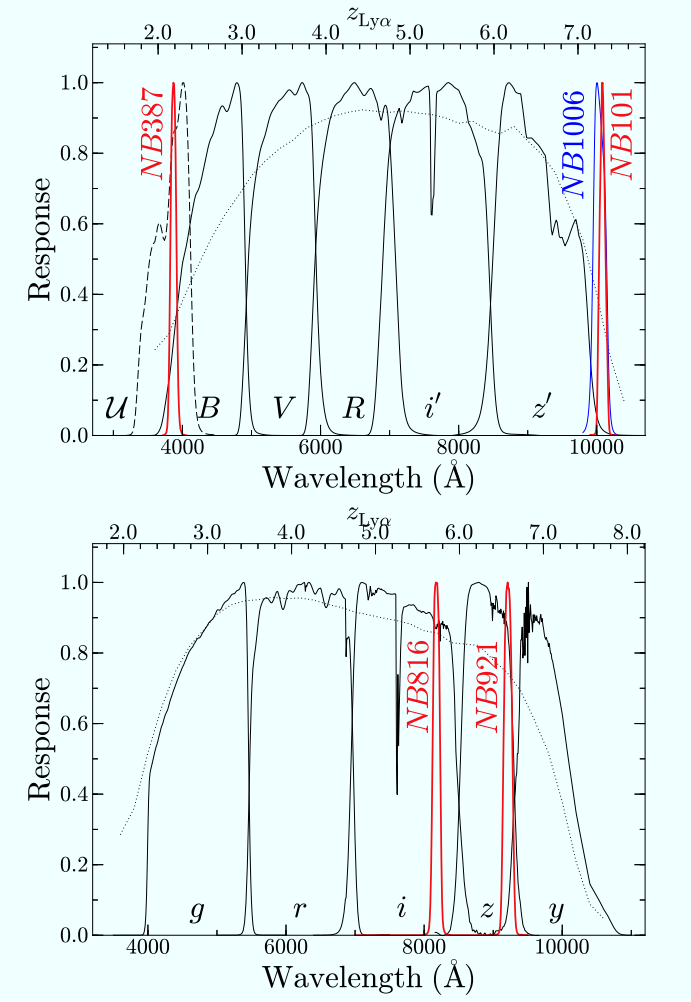

Figure 1.1 *Top:* Filter response curves for Subaru/Suprime-Cam filter set. The red lines at the wavelength of $\sim$ 4000Å and $\sim$ 10000Å are the transmission curves of *NB387* and *NB101*, respectively. The blue line represents the response curve of *NB1006*. The black solid curves denote the curves for Suprime-Cam broadband filters (B, V, R, i', and z'), while the black dashed line is that for CFHT/MegaCam u^* filter. This u^* filter is shown as the representative of the $\mathcal{U}$ filter. These response curves are based on actual lab measurements, and include the quantum efficiency of Suprime-Cam CCDs (the dotted line; Kamata et al. 2008), airmass, transmission+reflection of instrument, and telescope optics. For clarity, peaks of these curves are normalized to 1.0. The upper abscissa axis indicates a redshift of Lyα that corresponds to the wavelength. Note that *NB1006* widely covers a redshift range of $z = 7.2 - 7.3$, and that *NB101* targets a narrow redshift range centered at $z = 7.3$. *Bottom:* Same as the top figure, but for Subaru/Hyper Suprime-Cam filter set of broadbands (g, r, i, z, and y) and narrowbands (*NB816* and *NB921*). The black dotted curve shows the quantum efficiency of HSC CCDs.

CHAPTER 2
OBSERVATIONS AND DATA REDUCTION

2.1 Observations

2.1.1 Suprime-Cam/NB387, NB101 Observations

We have conducted a deep and large-area narrowband imaging survey for $z = 2.2$ LAEs with Subaru/Suprime-Cam. For these observations, we have developed a new narrowband filter, *NB387*, with a central wavelength, λ_c, of 3870Å and an FWHM of 94Å to identify LAEs in the redshift range of $z = 2.14 - 2.22$. With our *NB387* filter, we have observed five independent blank fields, the SXDS field (Furusawa et al. 2008), the Cosmic Evolution Survey (COSMOS) field (Scoville et al. 2007), the *Chandra* Deep Field South (CDFS; Giacconi et al. 2001), the *Hubble* Deep Field North (HDFN; Capak et al. 2004), and the SSA22 field (e.g., Steidel et al. 2000), in 2009 July 20 and December $14 - 16$, $19 - 20$. The SXDS field is located at $02^{\rm h}18^{\rm m}00^{\rm s}.0$, $-05^{\rm d}00'00''$ (J2000) (Furusawa et al. 2008; Ouchi et al. 2008, 2010), and consists of five subfields of ~ 0.2 deg^2, SXDS-C, -N, -S, -E, and -W (Furusawa et al. 2008). We cover these five SXDS subfields, COSMOS, CDFS, HDFN, and SSA22 by one pointing of Suprime-Cam whose field of view is ~ 0.2 deg^2. We thus have *NB387* imaging data in a total of nine pointing positions of Suprime-Cam. We summarize the details of our observations as well as image qualities in Table 2.1. In this study, we do not use the data of the SXDS-E subfield due to the poor seeing size of $\simeq 2''$ in FWHM of point-spread function (PSF; see Table 2.1). During our observations, we have taken spectrophotometric standard stars Feige34, LDS749B, and G93-48 (Oke 1990) for photometric calibration. Each standard star has been observed more than twice under the photometric condition with air masses of 1.1−1.3. In our analysis and selection for $z = 2.2$ LAEs, we use archival $\mathcal{U}$- and B-band data as well as our *NB387* images. Here, $\mathcal{U}$ generically indicates u^* or U described below. In the SXDS field, the u^*- and B-band data are taken with CFHT/MegaCam (S. Foucaud et al., in preparation) and Subaru/Suprime-Cam (Furusawa et al. 2008), respectively. The u^*- and B-band images in the COSMOS field are obtained with CFHT/MegaCam (McCracken et al. 2010) and Subaru/Suprime-Cam (Capak et al. 2007), respectively. We use VLT/VIMOS U-band (Nonino et al. 2009) and MPG 2.2m Telescope/WFI B-band (Hildebrandt et al. 2006) images in CDFS (see Kusakabe et al. 2015 for

more details), and KPNO 4m Telescope/MOSAIC prime focus camera U-band and Subaru/Suprime-Cam B-band images in HDFN (Capak et al. 2004). In SSA22 field, we use the u^*-band data of CFHT/MegaCam and B-band data of Subaru/Suprime-Cam (Hayashino et al. 2004). The properties of these optical broadband data are also summarized in Table 2.1. Note that in CDFS, Nakajima et al. (2013) do not use the VLT/VIMOS U-band image, but only the MPG 2.2m Telescope/WFI U-band image (Gawiser et al. 2006; Cardamone et al. 2010) that is significantly shallower than the VLT/VIMOS U-band data. The deep VLT/VIMOS U-band image allows us to remove foreground contamination efficiently, although the area coverage of VLT/VIMOS U-band data is smaller than that of MPG 2.2m Telescope/WFI U-band data. We thus use the deep VLT/VIMOS U-band image.

With our new *NB101* filter (see Section 1.4), we observed two independent fields, the SXDS and COSMOS fields. We choose a field of ~ 0.2 deg^2 to cover the southern half of SXDS-C and the northern half of SXDS-S, where bright stars do not exist and *HST* CANDELS (Grogin et al. 2011; Koekemoer et al. 2011), *UKIRT* UKIDSS (Lawrence et al. 2007), *Spitzer* SpUDS (PI: J. Dunlop), and SEDS (PI: G. Fazio) data are also available (see Figure 2 in Ota et al. 2010). The target field of COSMOS is an area of ~ 0.2 deg^2 centered at $10^{\rm h}00^{\rm m}28^{\rm s}.6$, $+02^{\rm d}12'21''.0$ (J2000) (Scoville et al. 2007). In the COSMOS field, there exist CANDELS and UltraVISTA (PI: J. Dunlop) imaging data. Each of the SXDS and COSMOS field is covered by one pointing of Suprime-Cam. Our observations were conducted in 2010 − 2013. The total on-source integration time is 106 hours where 36.3 and 69.5-hour data were obtained in the SXDS and COSMOS fields, respectively. We summarize the details of our observations as well as image qualities in Table 2.2. In addition to these *NB101* images, we use archival data of deep broadband (B, V, R, i' and z') images of the SXDS and COSMOS projects (Furusawa et al. 2008 and Capak et al. 2007 for SXDS and COSMOS fields, respectively). The properties of these broadband-data are also listed in Table 2.2.

2.1.2 Hyper Suprime-Cam/NB816, NB921 Observations

In our sample construction for $z = 5.7$ and 6.6 LAEs, we use narrowband (*NB816*, *NB921*) imaging data as well as broadband (g, r, i, z, y) imaging data, which are taken with Subaru/HSC. The narrowband filters, *NB816* and *NB921*, have central

wavelengths of 8170 Å and 9210 Å, and FWHMs of 113 Å and 134 Å to identify LAEs in the redshift range of $z = 5.67 - 5.77$ and $z = 6.52 - 6.63$, respectively. These narrow- and broad-band images are obtained in our ongoing HSC legacy survey under the Subaru Strategic Program (SSP; PI: S.Miyazaki, see also M. Takada et al., in preparation and M. Tanaka et al., in preparation). The HSC SSP has been allocated 300 nights over 5 years, and started in March 2014. The HSC-SSP survey has three layers with different sets of area and depth, the Wide, Deep, and Ultradeep layers. These layers will cover the sky area of ~ 1400, ~ 30, and ~ 4 deg^2, and will reach the 5σ limiting magnitudes (in r band) of ~ 26, ~ 27, and ~ 28 mag, respectively. While broadband images are taken in all three layers, narrowband images are obtained in the Deep and Ultradeep layers. We use early datasets of the HSC-SSP survey taken from March 2014 to April 2016 (S16A). With our *NB816* filter, the HSC-SSP collaboration has observed two blank fields in the Deep layer, the D-DEEP2-3 ($23^{\rm h}30^{\rm m}00^{\rm s}$, $+00^{\rm d}00'00\farcs0$) and D-ELAIS-N1 ($16^{\rm h}10^{\rm m}00^{\rm s}$, $+54^{\rm d}00'00\farcs0$) fields, and two blank fields in the Ultradeep layer, the UD-COSMOS ($10^{\rm h}00^{\rm m}29^{\rm s}$, $+02^{\rm d}12'21\farcs0$) and UD-SXDS ($02^{\rm h}18^{\rm m}00^{\rm s}$, $+05^{\rm d}00'00\farcs0$) fields. For *NB921* filter, a blank field of the D-COSMOS ($10^{\rm h}00^{\rm m}29^{\rm s}$, $+02^{\rm d}12'21\farcs0$) field in the Deep layer has been also observed as well as four fields described above. Each field in the Deep layer is covered by three or four pointing positions of HSC, and in the Ultradeep layer, each field is covered by one pointing of HSC. The details of our HSC-SSP survey is listed in Table 2.3.

2.2 Data Reduction

Our narrowband data of *NB387* and *NB101* are reduced with the Suprime-Cam Deep field REDuction package (SDFRED; Yagi et al. 2002; Ouchi et al. 2004). In this reduction process, we perform bias subtraction, flat-fielding, distortion+atmospheric-dispersion correction, sky subtraction, image alignments, and stacking. Before the image alignments, we mask out areas contaminated by spurious signals and meteor+satellite trails. We remove cosmic rays with a rejected-mean algorithm. For *NB387* data, we use *LA.COSMIC* (van Dokkum 2001) to reject cosmic rays because cosmic rays cannot remove by the stacking due to the small number of imaging shot. For *NB101* data, we make composite images from each one-night data set. Then, we stack all of these one-night composite images with weights based on signal-to-noise ratios of these images to make the final images. To obtain the weights, we measure

the photometric-zero point and the limiting magnitude for each one-night composite image.

After the stacking process, we align the reduced *NB387* and *NB101* images with the broadband images based on hundreds of bright stellar objects commonly detected in the *NB387* (*NB101*) and broadband images. We calculate photometric zero points of the *NB387* images from the standard-star data (see Section 2.1.1). We estimate the errors in the photometric zero points based on colors of stellar objects in the two-color diagram of *NB387* and two adjacent broadbands in the blue and red sides of *NB387* (e.g., u^*-*NB387* and $B-$*NB387* in SXDS). We compare the colors of stellar objects and the template 175 Galactic stars (Gunn & Stryker 1983), and regard the offsets as the uncertainties. The inferred uncertainties are $\lesssim 0.05$ mag, which are negligibly small for our study. We match the PSF sizes of broadband and *NB387* images in each field, referring to these stellar objects. We also calculate the photometric-zero points of the *NB101* images from our standard star data. Estimating the photometric-zero points, we took data of spectrophotometric standard stars of G191-B2B and GD153 (Bohlin et al. 1995) with *NB101*. We check these photometric-zero points with stellar sequences of observed stellar objects in our fields and 175 Galactic stars of Gunn & Stryker (1983) on a two-color diagram of $z' -$ *NB101* vs. $i' - z'$. After the check of the photometric-zero points, we estimate the limiting magnitudes of our images.

All of the *NB387* images, except for the SXDS-E data, have the PSF FWHM of $0\farcs7-1\farcs2$, and reach the 5σ limiting magnitudes of $24.9-26.5$ in a $2\farcs0$-diameter circular aperture. We summarize the qualities of these reduced *NB387* images in Table 2.1. We mask out the imaging regions that are contaminated with halos of bright stars, CCD blooming, and the low signal-to-noise ratio pixels near the edge of the images. After the masking, the total survey area is 5,138 arcmin^2, i.e. $\simeq 1.43$ deg^2. If we assume a simple top-hat selection function for LAEs whose redshift distribution is defined by the FWHM of *NB387*, this total survey area corresponds to the comoving volume of $\simeq 1.32 \times 10^6$ Mpc^3.

The final *NB101* images of SXDS and COSMOS have the seeing size of $\simeq 0\farcs8$, and reach the 5σ magnitude of $\simeq 25.0$ mag. We summarize the qualities of our final *NB101* images in Table 2.2. We use pixels of the imaging data neither contaminated with halos of bright stars, CCD blooming, nor low signal-to-noise ratio region near the edge of Suprime-Cam field of view. These low-quality regions are masked out, and the effective survey areas are 7.9×10^2 and 8.4×10^2 arcmin^2 in the SXDS

and COSMOS fields, respectively. Thus, our total survey area is 1.6×10^3 arcmin^2, i.e. $\simeq 0.5$ deg^2. If we assume a simple top-hat selection function for LAEs whose redshift distribution is defined by the FWHM of *NB101*, these effective survey areas correspond to the comoving survey volumes of 1.2×10^5 and 1.3×10^5 Mpc^3 for the SXDS and COSMOS fields, respectively.

The HSC data are reduced by the HSC-SSP collaboration with `hscPipe` (J. Bosch et al., in preparation), which is a branch of the Large Synoptic Survey Telescope pipeline (Ivezic et al. 2008; Axelrod et al. 2010; Jurić et al. 2015). This HSC pipeline performs CCD-by-CCD reduction, calibrates astrometry, mosaic-stacking, and photometric zeropoints, and generates catalogs for sources detected and photometrically measured in the stacked images. The photometric and astrometric calibrations are based on the data from Panoramic Survey Telescope and Rapid Response System 1 imaging survey (Schlafly et al. 2012; Tonry et al. 2012; Magnier et al. 2013). In the stacked images, we mask regions contaminated with diffraction spikes and halos of bright stars by using the mask extension outputs from the HSC pipeline. After the masking, the total effective survey areas in S16A data are 13.8 deg^2 and 21.2 deg^2 for *NB816* and *NB921*, respectively. These survey areas are $\sim 2-50$ and $\sim 4-100$ times larger than those of previous studies for LAEs at $z = 5.7$ (e.g., Shimasaku et al. 2006; Ouchi et al. 2008; Santos et al. 2016) and 6.6 (e.g., Ouchi et al. 2010; Kashikawa et al. 2011; Matthee et al. 2015), respectively. Under the assumption of a simple top-hat selection function for LAEs whose redshift distribution is defined by the FWHM of a narrowband filter, these survey areas correspond to comoving volumes of $\simeq 1.16 \times 10^7$ Mpc^3 and $\simeq 1.91 \times 10^7$ Mpc^3 for *NB816* and *NB921*, respectively. The narrowband images reach the 5σ limiting magnitudes in a $1''.5$-diameter circular aperture of $24.9-25.3$ in the Deep layer, and $25.5-25.7$ in the Ultradeep layer. Note that the PSF sizes of the HSC images are typically $0''.8$, which is sufficiently smaller than the aperture diameter of $1''.5$ (see also M. Tanaka et al., in preparation). We summarize the qualities of *NB816* and *NB921* images in Table 2.3.

Table 2.1. Summary of Suprime-Cam/*NB387* Observations and Data

Band	Field	Exposure Time (hr)	PSF size[a] (arcsec)	Area[b] (arcmin^2)	$m_{\rm lim}$[c] (mag)	Date of Observations	Reference[d]
NB387	SXDS-C	3.2	0.88	587	25.7	2009 Dec 14−16	(1), (2)
	SXDS-N	2.5	0.70	409	25.6	2009 Dec 16	(1), (2)
	SXDS-S	2.5	0.85	775	25.7	2009 Dec 16	(1), (2)
	SXDS-E[e]	3.3	1.95	···	···	2009 Dec 19, 20	(1), (2)
	SXDS-W	1.8	1.23	232	25.1[f]	2009 Dec 16, 19	(1), (2)
	COSMOS	4.5	0.97	845	26.1	2009 Dec 14−16	(2)
	CDFS	8.0	0.85	577	26.4	2009 Dec 14−15	(2), (3)
	HDFN	9.3	0.90	913	26.5	2009 Dec 14−16	(2)
	SSA22	1.0	0.91	800	24.9	2009 Jul 20	(2)
	Total	36.1	···	5138	···	···	···
			Archival Broadband Data				
$\mathcal{U}$	SXDS-C		0.85		26.9		(4)
	SXDS-N		0.85		26.9		(4)
	SXDS-S		0.85		26.9		(4)
	SXDS-E		0.85		26.9		(4)
	SXDS-W		0.85		26.9		(4)
	COSMOS		0.90		27.2		(5)
	CDFS		0.80		28.0		(6)
	HDFN		1.29		26.4[f]		(7)
	SSA22		1.00		26.3		(8)
B	SXDS-C		0.80		27.5		(9)
	SXDS-N		0.84		27.8		(9)
	SXDS-S		0.82		27.8		(9)
	SXDS-E		0.82		27.5		(9)
	SXDS-W		0.78		27.7		(9)
	COSMOS		0.95		27.5		(10)
	CDFS		0.97		26.9		(11)
	HDFN		0.77		26.3[f]		(7)
	SSA22		1.02		26.7		(8)

[a] We homogenize the PSF sizes of broadband and narrowband images in each field (see Section 2.2).

[b]The effective area for the $z = 2.2$ LAE selection. The effective areas of SXDS-C, -N, -S, -E, and -W are limited by the u^* image which covers 77% of SXDS (see Nakajima et al. 2012 for details). The area of CDFS is constrained by the deep U-band image taken with VLT/VIMOS (Nonino et al. 2009).

[c]The 5σ limiting magnitude in a circular aperture with a diameter of $2\farcs0$.

[d](1) Nakajima et al. (2012); (2) Nakajima et al. (2013); (3) Kusakabe et al. (2015); (4) S. Foucaud et al., in preparation (see also Nakajima et al. 2012); (5) McCracken et al. (2010); (6) Nonino et al. (2009); (7) Capak et al. (2004); (8) Hayashino et al. (2004); (9) Furusawa et al. (2008); (10) Capak et al. (2007); (11) Hildebrandt et al. (2006).

[e]We do not use the *NB387* image of SXDS-E since the PSF FWHM is relatively large.

[f]We use $2\farcs5$ and $3\farcs0$ diameter apertures for *NB387* of SXDS-W and *UB* of HDFN, respectively, due to bad seeings.

Table 2.2. Summary of Suprime-Cam/*NB101* Observations and Data

Field	Band	Exposure Time (hr)	PSF size[a] (arcsec)	Area (arcmin^2)	$m_{\rm lim}$[b] (5σ AB mag)	Date of Observations
SXDS	*NB101*	16.0	0.78		24.6	2010 Dec 29−2011 Jan 1
	NB101	20.3	0.86		24.3	2012 Dec 11−14
	NB101 (Final)	36.3	0.80	7.9×10^2	24.9	—
COSMOS	*NB101*	23.2	0.72		24.8	2010 Dec 29−2011 Jan 2
	NB101	17.0	0.99		23.7	2012 Dec 11−14
	NB101	29.3	0.90		24.4	2013 Feb 9−12
	NB101 (Final)	69.5	0.77	8.4×10^2	25.1	—
Archival Broadband Data[c]						
SXDS	B		0.84	7.9×10^2	28.1	
	V		0.84		27.7	
	R		0.84		27.6	
	i'		0.84		27.3	
	z'		0.80		26.9	
COSMOS	B		0.95	8.4×10^2	27.7	
	V		1.32		26.4	
	R		1.05		26.9	
	i'		0.95		26.6	
	z'		0.84		26.8	

[a]The FWHM value of PSF.

[b]The 5σ limiting magnitude in a circular aperture with a diameter of $2\times$ PSF FWHM.

[c]The Broadband images are archival data presented in Furusawa et al. (2008) for SXDS and Capak et al. (2007) for COSMOS. The SXDS and COSMOS z' data include the images taken by the Subaru intensive program conducted in $2009-2011$ (PI: H. Furusawa).

Table 2.3. Summary of HSC/*NB816* and *NB921* Observations and Data[a]

Band	Field	Area[b] (arcmin^2)	$m_{\rm lim}$[c] (5σ AB mag)
NB816	UD-COSMOS	7087	25.7
	UD-SXDS	6941	25.5
	D-DEEP2-3	15737	25.2
	D-ELAIS-N1	19998	25.3
NB921	UD-COSMOS	7368	25.6
	UD-SXDS	7260	25.5
	D-COSMOS	19099	25.3
	D-DEEP2-3	20740	24.9
	D-ELAIS-N1	21892	25.3
g	UD-COSMOS		26.9
	UD-SXDS		26.9
	D-COSMOS		26.5
	D-DEEP2-3		26.6
	D-ELAIS-N1		26.7
r	UD-COSMOS		26.6
	UD-SXDS		26.4
	D-COSMOS		26.1
	D-DEEP2-3		26.2
	D-ELAIS-N1		26.0
i	UD-COSMOS		26.2
	UD-SXDS		26.3
	D-COSMOS		26.0
	D-DEEP2-3		25.9
	D-ELAIS-N1		25.7
z	UD-COSMOS		25.8
	UD-SXDS		25.6
	D-COSMOS		25.5
	D-DEEP2-3		25.2
	D-ELAIS-N1		25.0
y	UD-COSMOS		25.1
	UD-SXDS		24.9
	D-COSMOS		24.7
	D-DEEP2-3		24.5
	D-ELAIS-N1		24.1

[a]The narrowband and broadband data are obtained in the HSC-SSP survey.

[b]The total effective areas of *NB816* and *NB921* are 49,763 and 76,359 arcmin^2, which correspond to 13.8 and 21.2 deg^2, respectively.

[c]The 5σ limiting magnitude in a circular aperture with a diameter of $1\farcs5$.

CHAPTER 3
PHOTOMETRIC SAMPLES OF LYα EMITTERS

3.1 Photometric Samples of Lyα Emitters at $z = 2.2$ and 7.3 with Suprime-Cam

Our source detection and photometry in *NB387* images are performed with SExtractor (Bertin & Arnouts 1996). We use the PSF-homogenized images (Section 2.2) to measure colors of objects. We identify sources that are made of contiguous > 5 pixels whose counts are above the $> 2\sigma$ brightness of the background fluctuations in our *NB387* images. We obtain a circular aperture magnitude of SExtractor's `MAG_APER` with an aperture's diameter of $2\farcs5$ in the SXDS-W field, $3\farcs0$ in the HDFN field, and $2\farcs0$ in the other fields, and define a 5σ-detection limit magnitude with the aperture size in each field. The different aperture diameters are applied, because the PSF sizes of the homogenized images in the SXDS-W and HDFN are large, $1\farcs23$ and $1\farcs29$, respectively. We use the aperture magnitudes to calculate colors of the sources, and adopt `MAG_AUTO` of SExtractor for our total magnitudes. All magnitudes of the sources are corrected for Galactic extinction of $E(B-V) = 0.020$, 0.018, 0.008, 0.012, and 0.08 in the SXDS, COSMOS, CDFS, HDFN, and SSA22 fields, respectively (Schlegel et al. 1998). We thus obtain source catalogs that contain 42995 (SXDS), 31401 (COSMOS), 24451 (CDFS), 36236 (HDFN), and 8942 (SSA22) objects with the aperture magnitudes brighter than the 5σ-detection limit magnitudes.

We select $z = 2.2$ LAE candidates based on narrowband excess colors of $\mathcal{U}-NB387$ and $B-NB387$, in the same manner as Nakajima et al. (2012) who present the first results of the *NB387* observations in the SXDS field. Figure 3.1 presents two color diagrams of $B-NB387$ versus $\mathcal{U}-NB387$. In this figure, we plot colors of model galaxies and Galactic stars to define the selection criteria for $z = 2.2$ LAE candidates. These tracks of model galaxies slightly change among the survey fields, because the transmission curves of $\mathcal{U}$- and B-bands are different among the using telescopes (see Section 2.1.1). Based on Figure 3.1, we apply the color criteria (Nakajima et al. 2012, 2013; Kusakabe et al. 2015)

$$\mathcal{U} - NB387 > 0.5 \text{ and } B - NB387 > 0.2 \tag{3.1}$$

to obtain $z = 2.2$ LAE candidates whose EW_0 are $EW_0 \gtrsim 20 - 30$Å. After the visual inspection to remove spurious sources, such as ghosts, bad pixels, surviving cosmic rays (see Nakajima et al. 2012 for more details), we identify 3137 LAE candidates in our survey fields. The sample of these LAE candidates is referred to as the full sample. This is so far the largest LAE sample in the large area field surveys (cf. 187 and 250 LAEs at $z \simeq 2.2$ with $EW_0 > 20$Å observed by Nilsson et al. 2009 and Guaita et al. 2010, respectively). We summarize the details of the full sample in Table 3.1.

We make a subsample with the uniform criterion of Lyα $EW_0 > 60$Å to compare the Lyα LF at $z = 3.1$ of Ouchi et al. (2008) (see Sections 5.1 and 6.1), and refer to the subsample as the EWgt60 sample. We apply the color criteria of

$$u^* - NB387 > 0.9 \text{ and } B - NB387 > 0.2 \text{ in SXDS, COSMOS, and SSA22,} \tag{3.2}$$

$$U - NB387 > 0.8 \text{ and } B - NB387 > 0.2 \text{ in CDFS,} \tag{3.3}$$

$$U - NB387 > 1.0 \text{ and } B - NB387 > 0.2 \text{ in HDFN} \tag{3.4}$$

for the EWgt60 sample. After the visual inspection, we obtain 985 LAE candidates for the EWgt60 sample that is summarized in Table 3.1.

Similarly, we identify sources on *NB101* images with SExtractor. We conduct the source detection in our *NB101* images, and obtain the broadband photometry at the positions of the sources. We detect a total of 69387 objects in the SXDS and COSMOS fields down to the 5σ limits of aperture magnitudes that are *NB101* = 24.9 (SXDS) and 25.1 (COSMOS). Here, we define the aperture magnitude of `MAG_APER` of SExtractor with an aperture size of 2× PSF FWHM, and use the aperture magnitude for measuring colors of objects. For total magnitude estimates, we apply an aperture correction value of 0.3 to the aperture magnitudes. Because `MAG_AUTO` of SExtractor gives biased magnitude measurements for faint objects around the detection limits, we use this aperture correction technique. Ono et al. (2012) study z-dropout galaxies at $z \sim 7$ using Subaru/Suprime-Cam data, and derive the aperture correction value of ~ 0.3 mag. We apply the same aperture correction value as Ono et al. (2012) because the PSF FWHM of the Ono et al's data ($\sim 0''.8 - 0''.9$) is similar to that of

our *NB101* data. The reliability of this technique is investigated below.

We isolate $z = 7.3$ LAE candidates from all of the objects detected above based on a narrowband excess of Lyα emission and no detection of blue continuum flux. Figures 3.2 and 3.3 show the color-magnitude diagrams of the *NB101* magnitude and the narrowband excess color, $z' -$ *NB101*, for the objects detected in SXDS and COSMOS fields. The detected objects have a color of $z' -$*NB101* $\simeq +0.2$ on average in the magnitude range of 22 $<$ *NB101* $<$ 24. To determine the $z' -$ *NB101* color criterion for our LAE candidate selection, we assume a model spectrum of $z = 7.3$ LAE that has a Lyα line and a flat ultraviolet (UV) continuum (i.e., $f_\nu = $ const.) with an IGM absorption (Madau 1995). Based on the model spectrum, we adopt the criterion that $z' -$ *NB101* $\geqslant 3.0$, which corresponds to LAEs with EW$_0 \gtrsim 0$Å, which is similar to the criterion adopted by Shibuya et al. (2012). Note that this small limit of the EW$_0$ criterion gives a chance to select high-z dropout galaxies and foreground red objects, due to photometric errors, which are the potential contamination sources. Because this EW$_0$ limit gives a more complete sample, we apply this EW$_0$ limit. We discuss the effect of this small EW$_0$ limit in Section 5.2.

Adding other criterion of no detectable continuum flux bluer than Lyα, we define the selection criteria of $z = 7.3$ LAEs:

$$\begin{aligned} &NB101 < NB101_{5\sigma} \text{ and } B > B_{3\sigma} \\ &\text{and } V > V_{3\sigma} \text{ and } R > R_{3\sigma} \text{ and } i' > i'_{3\sigma} \\ &\text{and } [(z' - NB101 \geqslant 3.0) \text{ or } (z' > z'_{3\sigma})] , \end{aligned} \tag{3.5}$$

where the indices of 5σ and 3σ denote the 5σ and 3σ detection limits of the images, respectively.

We apply these photometric criteria to all of our detected objects, and identify three and four $z = 7.3$ LAE candidates in the SXDS and COSMOS fields, respectively. We show the snapshot images of these LAE candidates in Figure 3.4. In our *NB101* ultra-deep survey, we have reached a 5σ limiting flux of $\simeq 6.5 \times 10^{-18}$ erg s^{-1} cm^{-2} corresponding to a limiting luminosity of $L_{\mathrm{Ly}\alpha} \simeq 4.1 \times 10^{42}$ erg s^{-1} in the SXDS field, and $\simeq 3.8 \times 10^{-18}$ erg s^{-1} cm^{-2} equivalent to $L_{\mathrm{Ly}\alpha} \simeq 2.4 \times 10^{42}$ erg s^{-1} in the COSMOS field. These limiting luminosities are derived from the 5σ limiting magnitudes of *NB101* and the 1σ limiting magnitudes of z'. These are conservative estimates, because the limiting luminosity values are larger than those calculated with

the $> 1\sigma$ limiting magnitudes of z'. In the calculations for the Lyα luminosities, we assume that Lyα emission is placed at the central wavelength of the narrow band. Ouchi et al. (2008) derive the Lyα luminosities in the same manner as ours, and compare these Lyα luminosities with spectroscopic luminosities. They find that both measurements agree well within the error bars, and that the difference of these values is small (see Section 4.4 for the effects of the Lyα luminosity uncertainties in Lyα LF derivation). The *NB101* image of COSMOS field is the deepest image in our *NB101* data. The 5σ limiting luminosity in the COSMOS field is about 4 times deeper than previous Subaru studies for LAEs at $z \sim 7$ (Ota et al. 2008, 2010; Shibuya et al. 2012). Moreover, the 5σ limiting luminosity is comparable with those of previous Subaru $z = 3.1 - 6.6$ LAE surveys (Shimasaku et al. 2006; Kashikawa et al. 2006, 2011; Ouchi et al. 2008, 2010).

We present the photometric properties of our $z = 7.3$ LAE candidates in Table 3.2. The total magnitudes listed in Table 3.2 are obtained by the aperture-correction technique explained above. We compare the total magnitude and `MAG_AUTO` of SExtractor for the most luminous LAE candidate that probably includes a negligible bias in the `MAG_AUTO` estimate, and find that these two magnitudes are consistent within the errors. Thus, it is reasonable to use the total magnitudes given by the aperture-correction technique that requires the assumption that $z = 7.3$ LAEs are point sources (Ono et al. 2010a, 2012).

We investigate our $z = 7.3$ LAE candidates in the J and H images of *HST* CANDELS fields that are subfields of our COSMOS and SXDS survey areas. Two out of seven LAE candidates, NB101-COSMOS-37050 and NB101-COSMOS-37548, fall in the CANDELS field of COSMOS. We detect NB101-COSMOS-37050 both in the J and H images (Figure 3.4), but NB101-COSMOS-37548 neither in the J nor H data. We obtain the J and H magnitudes of NB101-COSMOS-37050, and present the magnitudes in Table 3.2. Because all LAE candidates in the SXDS field exist out of the CANDELS field of SXDS, there are no counterparts of LAE candidates found in the CANDELS-SXDS field.

We examine whether $z = 7.2 - 7.3$ LAEs found by Shibuya et al. (2012) are identified in our *NB101* data. Shibuya et al. (2012) have observed the SXDS subfield same as our survey area with their *NB1006* filter (Section 1.4), and obtained two photometric LAE candidates, SXDS-NB1006-1 and SXDS-NB1006-2. However, both of two LAEs of Shibuya et al. (2012) are not detected in our *NB101* images. Because

Shibuya et al. (2012) report that their spectroscopy indicates that one of them, SXDS-NB1006-2, resides at $z = 7.215$, the redshift of SXDS-NB1006-2 is out of our survey redshift range of $z = 7.302 \pm 0.037$ where *NB101* has a sensitivity for a Lyα emission line. Thus, the reason for no detection of SXDS-NB1006-2 is clear, while the reason for another object, SXDS-NB1006-1, is unknown. Since SXDS-NB1006-1 is not confirmed by their spectroscopic follow-up observations, it is possible that the Lyα emission of SXDS-NB1006-1 also falls in the wavelength where *NB101* does not cover. Note that the FWHM of *NB1006* is 214Å, while *NB101* is only 90Å (Section 1.4).

3.2 Photometric Samples of Lyα Emitters at $z = 5.7$ and 6.6 with Hyper Suprime-Cam

We construct $z = 5.7$ and 6.6 LAE samples from the HSC database in which the source detection and photometry are performed with the HSC pipeline (`hscPipe`; see Section 2.2). In this pipeline, there are two procedures of the photometry, the meas and forced photometry. The meas photometry is performed for each source on individual band images, and the forced photometry is conducted at the same positions for sources on all band images. We use the forced photometry for the magnitude measurements of sources, and apply both the meas and forced photometry for the color calculation of sources. Note that the forced photometry is similar to that performed with SExtractor described in Section 3.1. For photometric source measurements, we use the aperture magnitudes with an aperture diameter of $1''.5$, and the `cmodel` magnitudes as our total magnitudes. The `cmodel` magnitudes are derived by light profile fitting. We apply both the aperture and `cmodel` magnitudes for the magnitude measurements, and choose `cmodel` magnitudes for the color calculations. The magnitudes for each source are corrected for Galactic extinction (Schlegel et al. 1998).

We select LAE candidates at $z = 5.7$ and 6.6 based on narrowband excess colors by Lyα emission, $i - NB816$ and $z - NB921$, respectively, and no detection of blue continuum fluxes, in the same manner as Ouchi et al. (2008, 2010). We apply the

following selection criteria to the objects in the HSC database;

$$
\begin{aligned}
&(NB816^{\rm total}_{\rm forc} < NB816_{5\sigma} \text{ or } NB816^{\rm aper}_{\rm forc} < NB816_{5\sigma}) \\
&\text{and } (g^{\rm total}_{\rm forc} > g_{3\sigma} \text{ or } g^{\rm aper}_{\rm forc} > g_{3\sigma}) \\
&\text{and } \left(i^{\rm total}_{\rm forc} - NB816^{\rm total}_{\rm forc} > 1.2 \text{ or } i^{\rm total}_{\rm meas} - NB816^{\rm total}_{\rm meas} > 1.2\right) \\
&\text{and } \Big(\left[(r^{\rm total}_{\rm forc} < r_{3\sigma} \text{ or } r^{\rm aper}_{\rm forc} < r_{3\sigma}) \text{ and } (r^{\rm total}_{\rm forc} - i^{\rm total}_{\rm forc} > 1.0 \text{ or } r^{\rm total}_{\rm meas} - i^{\rm total}_{\rm meas} > 1.0)\right] \\
&\text{ or } (r^{\rm total}_{\rm forc} > r_{3\sigma} \text{ or } r^{\rm aper}_{\rm forc} > r_{3\sigma}) \Big) ,
\end{aligned}
\tag{3.6}
$$

for $z = 5.7$ LAEs, and

$$
\begin{aligned}
&(NB921^{\rm total}_{\rm forc} < NB921_{5\sigma} \text{ or } NB921^{\rm aper}_{\rm forc} < NB921_{5\sigma}) \\
&\text{and } (g^{\rm total}_{\rm forc} > g_{3\sigma} \text{ or } g^{\rm aper}_{\rm forc} > g_{3\sigma}) \text{ and } (r^{\rm total}_{\rm forc} > r_{3\sigma} \text{ or } r^{\rm aper}_{\rm forc} > r_{3\sigma}) \\
&\text{and } \left(z^{\rm total}_{\rm forc} - NB921^{\rm total}_{\rm forc} > 1.0 \text{ or } z^{\rm total}_{\rm meas} - NB921^{\rm total}_{\rm meas} > 1.0\right) \\
&\text{and } \Big(\left[(z^{\rm total}_{\rm forc} < z_{3\sigma} \text{ or } z^{\rm aper}_{\rm forc} < z_{3\sigma}) \text{ and } (i^{\rm total}_{\rm forc} - z^{\rm total}_{\rm forc} > 1.3 \text{ or } i^{\rm total}_{\rm meas} - z^{\rm total}_{\rm meas} > 1.3)\right] \\
&\text{ or } (z^{\rm total}_{\rm forc} > z_{3\sigma} \text{ or } z^{\rm aper}_{\rm forc} > z_{3\sigma}) \Big) ,
\end{aligned}
\tag{3.7}
$$

for $z = 6.6$ LAEs, where the indices of total and aper represent the `cmodel` and aperture magnitude, respectively, and the indices of forc and meas are the forced and meas photometry, respectively (see also T. Shibuya et al. in preparation). In addition to the color selection, we use the `countinputs` parameter, which represents the number of exposure for each object. We apply `countinputs` ≥ 3 for the narrowband images. We also remove objects affected by bad pixels, proximity to bright stars, or poor photometric measurement by using the following flag; `flags_pixel_edge`, `flags_pixel_interpolated_center`, `flags_pixel_saturated_center`, `flags_pixel_cr_center`, and `flags_pixel_bad`. After the visual inspection for the rejection of spurious sources and cosmic rays, we identify 1081 and 1273 LAE candidates at $z = 5.7$ and 6.6, respectively. The samples of these LAE candidates are referred to as the HSC full samples. The HSC full samples are $\sim 2-6$ times larger than photometric samples in previous studies (e.g., Ouchi et al. 2008, 2010; Matthee et al. 2015; Santos et al. 2016). Note that the color selection criterion for $z = 5.7$ LAEs (i.e., $i - NB816 > 1.2$ in Equation 3.6) corresponds to $\mathrm{EW}_0 \gtrsim 10$Å in the case of $f_\nu =$ const. with an IGM absorption (Madau 1995). This EW limit is similar to those of previous studies ($\mathrm{EW}_0 \gtrsim 10-30$Å; e.g., Shimasaku et al. 2006; Ouchi et al. 2008;

Santos et al. 2016). On the other hand, the color criterion of $z - NB921 = 1.0$ in Equation (3.7) for $z = 6.6$ LAEs corresponds to the EW_0 limit significantly lower than those of previous studies (e.g., Ouchi et al. 2010; Matthee et al. 2015). This is because the relative wavelength position of *NB921* to z' (or z) band filter is different between Suprime-Cam and HSC (see Figure 1.1). For the consistency of the $z = 6.6$ LAE selection between our and previous studies, we adopt a new color criterion of $z - NB921 > 1.8$. This criterion corresponds to $\mathrm{EW}_0 > 14$Å (f_ν = const.), which is the same one of Ouchi et al. (2010). Moreover, for the derivation of Lyα LFs, we use only the forced photometry for the color selection in Equations (3.6) and (3.7) in order to apply the photometry similar to that of previous studies using SExtractor. After adopting the new color criterion and only the forced photometry, we find 880 and 328 LAEs at $z = 5.7$ and 6.6, respectively. We refer to these LAE samples as the HSC Lyα LF samples. We use the HSC Lyα LF samples to derive Lyα LFs at $z = 5.7$ and 6.6 in Sections 4.4.2 and 4.4.3. Our samples of LAE candidates at $z = 5.7$ and 6.6 are listed in Table 3.3.

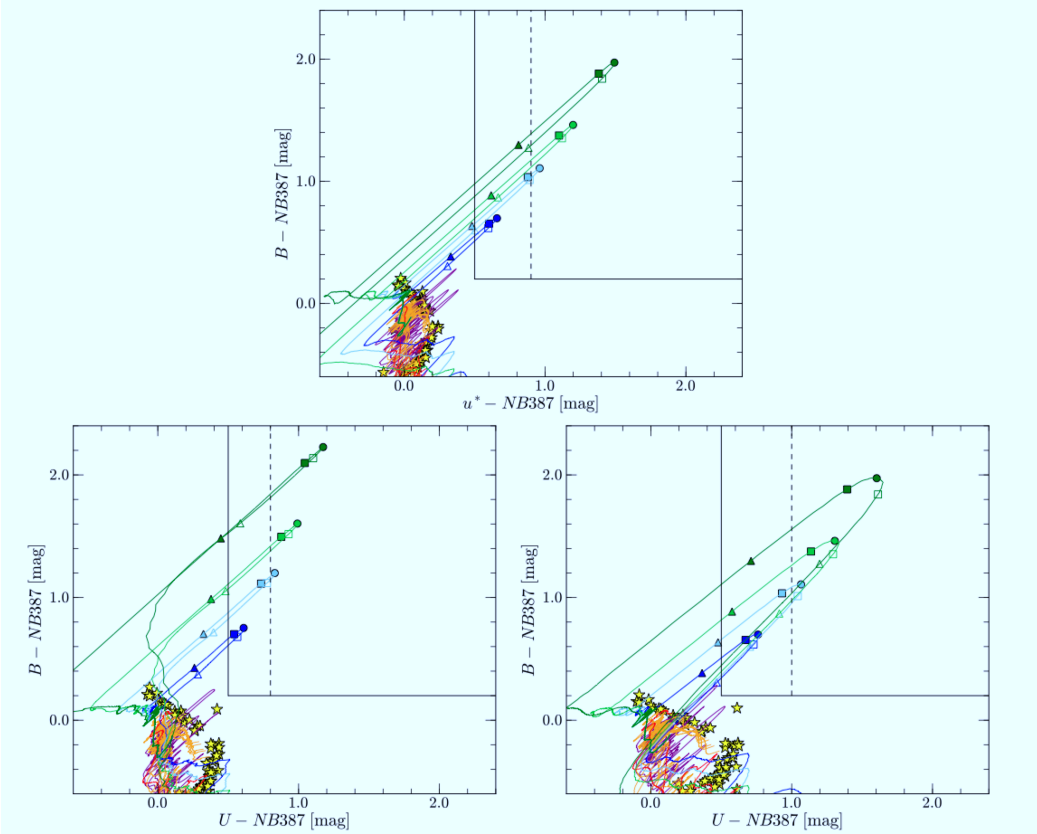

Figure 3.1 Two color diagrams for the selection of $z = 2.2$ LAEs: $B-NB387$ vs. $u^*-NB387$ for SXDS, COSMOS, and SSA22 (top); $B-NB387$ vs. $U-NB387$ in CDFS (bottom left); $B-NB387$ vs. $U-NB387$ in HDFN (bottom right). The solid lines in blue, light blue, light green, and green represent the color tracks of redshifted model LAE SEDs with Lyα EW$_0$ = 30, 60, 100, and 200Å, respectively. These models are produced by using the Bruzual & Charlot (2003) population synthesis model where we adopt a 30 Myr simple stellar population with Salpeter IMF and adding a Lyα emission. We apply the Madau (1995) prescription to take into account the IGM absorption. The symbols on these tracks correspond to $z = 2.14$ (filled triangles), 2.16 (filled squares), 2.18 (filled circles), 2.20 (open squares), and 2.22 (open triangles). The red and orange curves show the tracks of three elliptical (age of 2, 5, 13 Gyr) and six spiral (S0, Sa, Sb, Sc, Sd, and Sdm) galaxies from the SWIRE template library (Polletta et al. 2007), respectively. The purple solid lines indicate six templates of nearby starburst galaxies (Kinney et al. 1996). These elliptical, spiral and starburst template galaxies are redshifted from $z = 0.0$ up to 2.0 with a step of $\Delta z = 0.001$. The yellow star marks are 175 Galactic stars given by Gunn & Stryker (1983). The black solid and dashed lines represent the color criteria to select our $z = 2.2$ LAE candidates whose Lyα EWs are larger than $20 - 30$Å and 60Å, respectively.

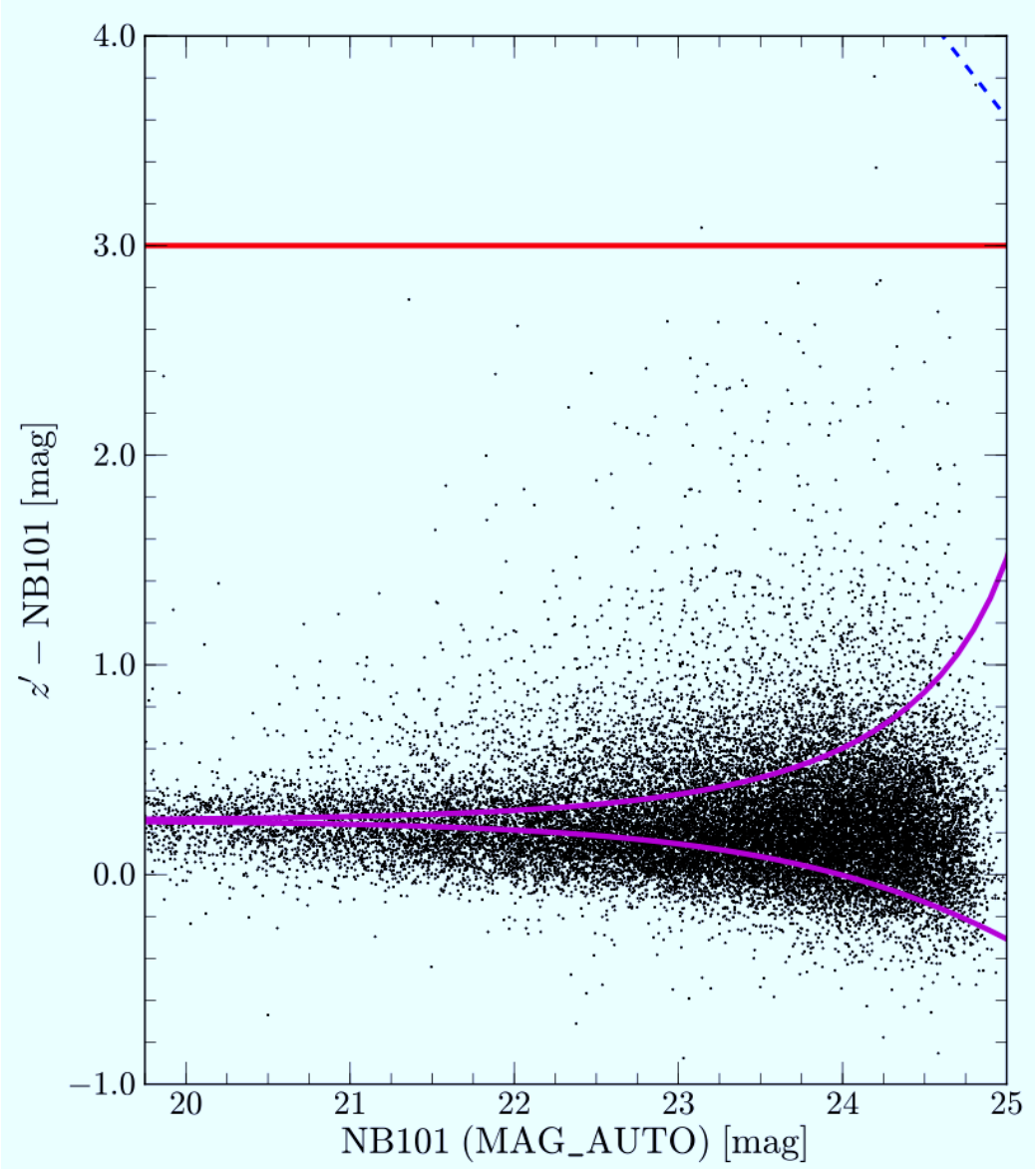

Figure 3.2 Color-magnitude diagram of $z' - NB101$ vs. $NB101$ for objects detected in the SXDS field. The black dots show all of the detected objects. The blue-dashed and magenta-solid lines indicate the 1σ limit of the z' magnitude and the 3σ error of the $z' - NB101$ color, respectively. The red line represents the $z' - NB101$ color criterion for the selection of our $z = 7.3$ LAEs.

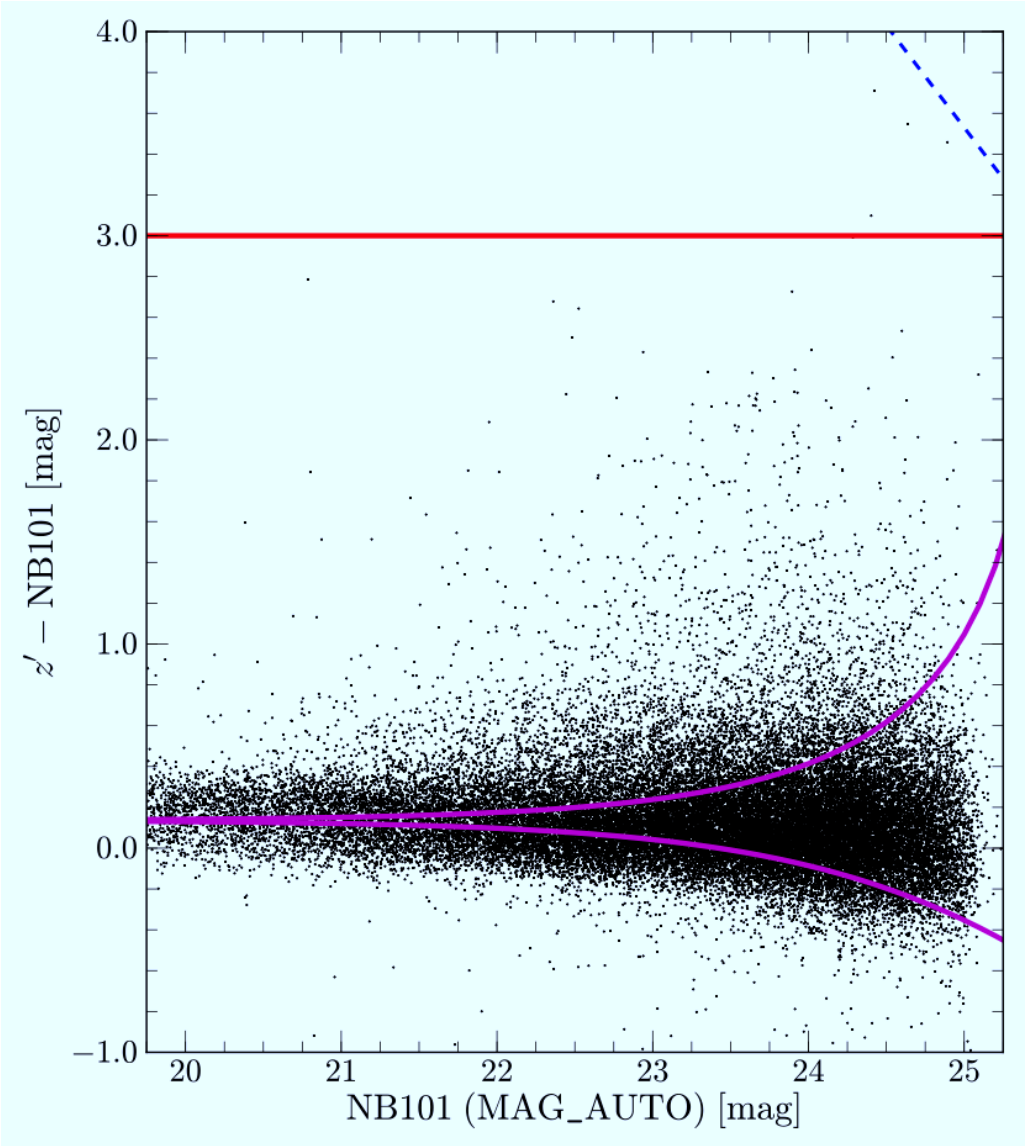

Figure 3.3 Same as Figure 3.2, but for the COSMOS field.

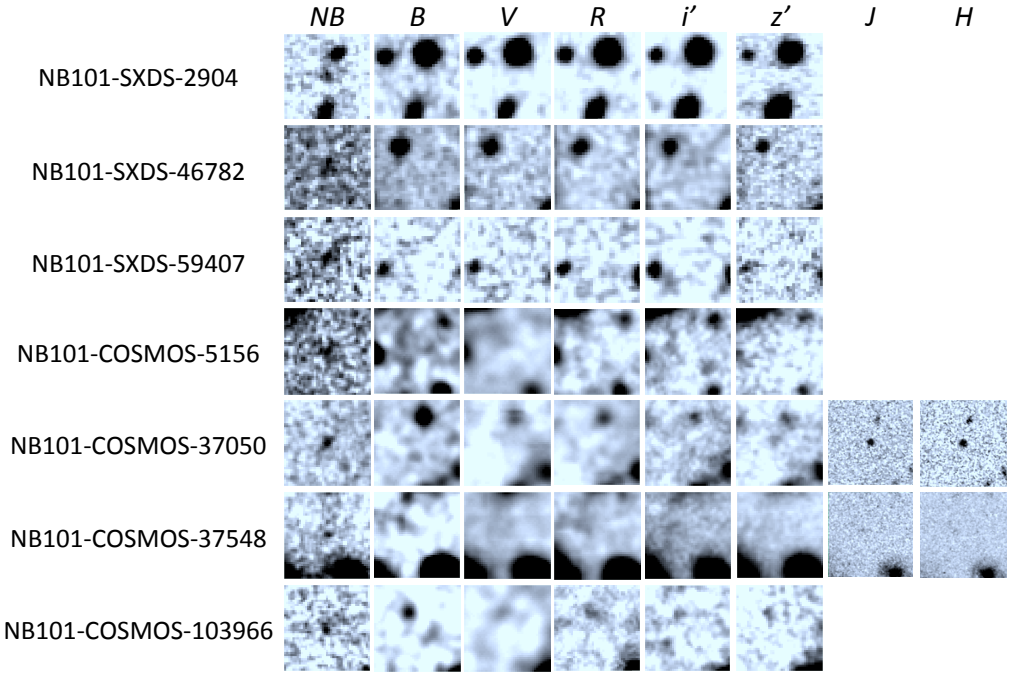

Figure 3.4 Snapshots of our $z = 7.3$ LAE candidates. The size of each image is $6'' \times 6''$. North is up and east is to the left.

Table 3.1. Photometric Sample of $z = 2.2$ LAEs

Field	All LAE sample[a]	X-ray detection[b]	UV detection[c]	Radio detection[d]	Culled sample[e]
		The full sample			
SXDS-C	277	3 [3]	3 [3]	0 [0]	274
SXDS-N	239	4 [4]	5 [4]	0 [0]	234
SXDS-S	374	5 [3]	5 [4]	1 [1]	367
SXDS-W[f]	44	0 [0]	0 [0]	0 [0]	44
COSMOS	642	20 [10]	10 [10]	7 [5]	619
CDFS	423	6 [4]	···	6 [4]	415
HDFN	967	7 [1]	11 [1]	···	950
SSA22	171	···	3 [···]	···	168
Total[g]	3137 (1576)	45	37	14	3071 (1538)
		The EWgt60 sample			
SXDS-C	103	2 [2]	2 [2]	0 [0]	101
SXDS-N	69	0 [0]	0 [0]	0 [0]	69
SXDS-S	129	1 [0]	1 [0]	0 [0]	127
SXDS-W[f]	6	0 [0]	0 [0]	0 [0]	6
COSMOS	194	9 [4]	4 [4]	3 [3]	184
CDFS	142	3 [2]	···	2 [2]	139
HDFN	298	2 [0]	0 [0]	···	296
SSA22	44	···	1 [···]	···	43
Total	985	17	8	5	965

[a]The numbers of $z = 2.2$ LAE candidates after the color selection and rejection of spurious objects.

[b]The numbers of $z = 2.2$ LAE candidates detected in the X-ray data. The values in square brackets represent the numbers of objects that are also detected in the UV and/or radio data.

[c]The numbers of $z = 2.2$ LAE candidates detected in the UV data taken by *GALEX*. The values in square brackets show the numbers of objects that are also detected in the X-ray and/or radio data.

[d]The numbers of $z = 2.2$ LAE candidates detected in the radio data. The values in square brackets show the numbers of objects that are also detected in the X-ray and/or UV data.

[e]The numbers of $z = 2.2$ LAE candidates with no counterpart detection(s) in multiwavelength data of X-ray, UV, and radio.

[f] The numbers of LAEs are small in SXDS-W. This is because the limiting magnitude in SXDS-W is brighter than those in the other fields by ~ 0.5 mag, and the effective area of SXDS-W is smaller than those of the other fields by a factor of ~ 3 (Table 2.1). The combination of the bright limiting magnitude and the small area reduces the number of LAEs in SXDS-W.

[g]The total numbers of $z = 2.2$ LAE candidates. The values in parentheses indicate the total numbers of LAEs found in the SXDS and COSMOS fields.

Table 3.2. Our $z = 7.3$ LAE Candidates

ID	B	V	R	i'	z'	$NB101$[a]	$NB101$(total)[b]	J[a]	H[a]	L(Lyα) (10^{42} erg s^{-1})
NB101-SXDS-2904	> 28.6	> 28.3	> 28.1	> 27.8	> 27.4	$24.50^{+0.16}_{-0.14}$	$24.20^{+0.12}_{-0.11}$	—	—	9.68
NB101-SXDS-46782	> 28.6	> 28.3	> 28.1	> 27.8	> 27.4	$24.84^{+0.23}_{-0.19}$	$24.54^{+0.17}_{-0.15}$	—	—	5.72
NB101-SXDS-59407	> 28.6	> 28.3	> 28.1	> 27.8	> 27.4	$24.80^{+0.22}_{-0.18}$	$24.50^{+0.16}_{-0.14}$	—	—	6.13
NB101-COSMOS-5156	> 28.3	> 27.0	> 27.4	> 27.2	> 27.3	$24.98^{+0.21}_{-0.18}$	$24.68^{+0.16}_{-0.14}$	—	—	3.82
NB101-COSMOS-37050	> 28.3	> 27.0	> 27.4	> 27.2	> 27.3	$24.84^{+0.19}_{-0.16}$	$24.54^{+0.14}_{-0.12}$	$25.42^{+0.05}_{-0.05}$	$25.39^{+0.06}_{-0.05}$	5.11
NB101-COSMOS-37548	> 28.3	> 27.0	> 27.4	> 27.2	> 27.3	$25.03^{+0.23}_{-0.19}$	$24.73^{+0.17}_{-0.14}$	> 27.6	> 27.5	3.39
NB101-COSMOS-103966	> 28.3	> 27.0	> 27.4	> 27.2	> 27.3	$25.07^{+0.23}_{-0.19}$	$24.77^{+0.17}_{-0.15}$	—	—	3.01

[a]The magnitudes with the 1σ error measured with an aperture whose diameter is $2\times$ PSF FWHM.

[b]The total magnitudes which are obtained by the aperture-correction technique explained in Section 3.1

Table 3.3. Photometric Sample of $z = 5.7$ and 6.6 LAEs

Field	HSC full sample[a]	HSC Lyα LF sample[b]
The $z = 5.7$ LAE sample		
UD-COSMOS	202	193
UD-SXDS	224	205
D-DEEP2-3	423	328
D-ELAIS-N1	232	154
Total	1081	880
The $z = 6.6$ LAE sample		
UD-COSMOS	435	154
UD-SXDS	60	28
D-COSMOS	249	52
D-DEEP2-3	178	39
D-ELAIS-N1	351	55
Total	1273	328

[a]The numbers of LAE candidates after the color selection (Equations 3.6 and 3.7) and rejection of spurious objects.

[b]The numbers of LAE candidates after the selection of only the forced photometry and a new color criterion for $z = 6.6$ LAEs (see text for details).

CHAPTER 4
LUMINOSITY FUNCTIONS

4.1 Contamination

4.1.1 Contamination of Suprime-Cam LAEs at $z = 2.2$ and 7.3

We investigate the contamination sources of our $z = 2.2$ LAE samples that are low-z emitters whose emission lines are redshifted to the bandpass of *NB387*. The major strong emission that enters into the *NB387* bandpass is [OII]λ3727. However, our survey area of 5,138 arcmin^2 (Section 2.2) corresponds to the comoving volume of 1.22×10^3 Mpc^3 for [OII] emitters at $z = 0.04$, which is three orders of magnitude smaller than the survey volume of our $z = 2.2$ LAEs (1.32×10^6 Mpc^3). Moreover, the color criterion defined by Equation (3.1) corresponds to a relatively large rest-frame EW limit of $\gtrsim 70$Å for $z = 0.04$ [OII] emitters. Ciardullo et al. (2013) examine [OII] LFs and EW distributions at $z \sim 0.1$ and find that the [OII] EW distribution has an exponential scale of 8.0Å, which is significantly smaller than our selection criterion for [OII] emitters (i.e., $EW_0 \sim 70$Å). Based on our survey parameters (see Sections 2.2 and 3.1) and the Ciardullo et al.'s [OII] LF and EW distribution, the expected number of [OII] emitters at $z = 0.04$ in our full sample is $\sim 3 \times 10^{-2}$. Therefore, the probability of the [OII] emitter contamination would be very small. We further discuss the possibility that our bright sources would include CIVλ1548 and CIII]λ1909 emitters at $z \sim 1.5$. These CIV and CIII] emitters should be mostly AGNs, because these emitters have to have a CIV or CIII] EW greater than 30Å to pass our selection criterion. This EW value is significantly larger than the one of the star-forming galaxies. Because in Section 7.2, we find that our AGN UV LF is consistent with the previous SDSS measurements, only a negligibly small fraction of the $z \sim 1.5$ AGNs include our sample.

Nevertheless, spectroscopic follow-up observations for our LAEs have been conducted with Magellan/IMACS, MagE, and Keck/LRIS by Nakajima et al. (2012), Hashimoto et al. (2013), Shibuya et al. (2014) and M. Rauch et al., in preparation. A total of 43 LAEs are spectroscopically confirmed. These spectroscopic observations find no foreground interlopers such as [OII] emitters at $z = 0.04$ that show [OIII]5007 emission at 5200Å (see e.g. Nakajima et al. 2012). We note that these spectroscopic redshift confirmations are limited to the bright LAEs with *NB387* $\lesssim 24.5$, and that

the number of the faint LAEs confirmed by spectroscopy is small. However, the contamination rate at the faint end is probably not high. This is because the EW criterion of our selection corresponds to ~ 70Å for the major foreground faint emitters of $z = 0.04$ [OII] emitters. Most of these potential contamination sources do not pass this large EW limit, as discussed above. Thus, the effects of contamination sources are negligibly small in our LAE samples.

We also investigate the contamination of our $z = 7.3$ LAE sample. The sources of possible contamination are spurious objects, transients, and foreground interlopers. First, our *NB101* images of the SXDS and COSMOS fields are taken in 2010−2012 and 2010−2013, respectively (see Table 2.2). We stack *NB101* data of SXDS field observed in 2010−2011 and 2012, and obtain *NB101* images for the two epochs. Similarly, we make three *NB101* stacked images of COSMOS field at three epochs, 2010−2011, 2012, and 2013. The 5σ limiting magnitudes of these epoch images are summarized in Table 2.2. The results of independent photometry at the different epochs of our observations are shown in Table 4.1. All of the magnitudes of our LAE candidates in the multi-epochs are consistent within the $\simeq 95\%$-significance levels of the photometric errors. The UV continuum fluxes of AGNs (or QSOs) are variable (e.g., de Vries et al. 2005). However, we find no variable signatures of AGNs (or QSOs) in our LAEs. Because our LAEs are selected from narrowband images taken over 3-4 years, a fraction of transient contamination (e.g., supernovae) in our LAE sample is very small. Similarly, all of our LAEs, except for NB101-SXDS-46782 and NB101-COSMOS-37050, are detected at the > 3 sigma levels in the ≥ 2 epoch images. Thus, our LAEs, except for NB101-SXDS-46782 and NB101-COSMOS-37050, are not spurious sources. NB101-SXDS-46782 and NB101-COSMOS-37050 are found only at the $\simeq 2\sigma$ levels in the 2012 and 2012-2013 epoch images, respectively. However, we have identified the sources of NB101-SXDS-46782 and NB101-COSMOS-37050 in these epoch images by visual inspection. It is likely that NB101-SXDS-46782 and NB101-COSMOS-37050 are also not spurious sources. Second, spectroscopic follow-up observations for one of our candidates, NB101-SXDS-2904, were conducted with Keck/NIRSPEC, LRIS and MOSFIRE, and a single emission line that is probably Lyα is clearly detected from this object by all of these Keck spectroscopic observations (M. Ouchi et al. in preparation). Although only one LAE in our sample is observed by spectroscopy, no foreground interlopers are, so far, found by spectroscopic observations. Note that in Section 5.2, we discuss our sample biases due to the choice of

Lyα EW_0 limit.

4.1.2 Contamination of HSC LAEs at $z = 5.7$ and 6.6

We investigate the contamination sources in our $z = 5.7$ and 6.6 LAE samples. Spectroscopic follow-up observations for some LAE candidates in our HSC full samples have been conducted with Subaru/FOCAS (PI: T. Shibuya). A total of 16 LAE candidates at $z = 5.7$ and 6.6 with $NB = 22.0 - 24.0$ have been observed, so far, and 11 out of 16 objects have been confirmed as LAEs. The other 5 objects will be low-z emitters, which show Hα, [OIII]λ5007, or [OII]$\lambda\lambda$3726, 3729 emission (see T. Shibuya et al. in preparation). Thus, we find that the contamination rate, $f_{\rm cont}$, in our LAE samples is $f_{\rm cont} \simeq 30\%$ ($= 5/16$). This $f_{\rm cont}$ value is similar to that obtained in Ouchi et al. (2008, 2010) and Kashikawa et al. (2011), who conduct the Subaru/Suprime-Cam imaging survey for LAEs at $z \sim 3 - 7$. Here, we adopt the $f_{\rm cont}$ value for the contamination correction of the Lyα LF measurements (see Section 4.4).

4.2 Detection Completeness

4.2.1 Suprime-Cam images

We estimate detection completeness as a function of the *NB387* (*NB101*) magnitude by Monte Carlo simulations. We distribute a number of pseudo LAEs with various magnitudes in our *NB387* (*NB101*) images, and detect the pseudo LAEs in the same manner as our source extraction for real sources with SExtractor (Section 3.1). Here, we assume that high-z LAEs are point sources whose profiles are obtained by the stack of bright point sources in our narrowband images. We define the detection completeness as the fraction of the numbers of the extracted pseudo LAEs to all of the input pseudo LAEs, and obtain the detection completeness presented in Figures 4.1 and 4.2. We find that the detection completeness is typically $\gtrsim 90\%$ for luminous sources with *NB387* < 24.5 (or *NB101* $\lesssim 24.5$) and nearly 50% at around the 5σ limiting magnitude of narrowband images (see Tables 2.1 and 2.2).

4.2.2 HSC images

We use the `SynPipe` software (S. Huang et al. in preparation) in order to estimate detection completeness in HSC/*NB816* and *NB921* images by Monte Carlo simulations. The `SynPipe` software can add synthetic objects in HSC images, and perform source detection and photometry. These source detection and photometry are the same procedures as the HSC pipeline (`hscPipe`; see Section 2.2). Using the `SynPipe` software, we distribute ~ 18000 pseudo LAEs with various magnitudes in *NB816* and *NB921* images. These pseudo LAEs have a Sérsic profile with the index of $n = 1.5$, and the half-light radius of $r_{\rm e} \sim 0.9$ kpc. These values are similar to the average ones of $z \sim 6$ LBGs with $L_{\rm UV} = 0.3 - 1 L^*_{z=3}$ (Shibuya et al. 2015). We detect these input objects with `SynPipe`, and calculate the detection completeness whose definition is shown in Section 4.2.1. Figure 4.3 shows the detection completeness for HSC/*NB816* and *NB921* images. We find that the detection completeness is typically $\gtrsim 80\%$ for objects with $NB \lesssim 24.5$, and $\sim 40\%$ at the 5σ limiting magnitudes of narrowband images. These results are similar to those for Suprime-Cam data (Section 4.2.1). We note that for bright objects ($NB \lesssim 24.5$), the detection completeness of Suprime-Cam images reaches $\sim 100\%$, while the detection completeness of HSC images is only $\sim 80 - 90\%$. The difference of detection completeness is caused by that of the procedures for distributing pseudo LAEs between Suprime-Cam and HSC images. In Suprime-Cam images, we distribute pseudo LAEs in the blank region where real objects do not exist. On the other hand, we allow pseudo LAEs to be distributed near (or on) real objects in HSC images. Thus, the detection completeness of HSC images is slightly lower than that of Suprime-Cam images. We estimate the Suprime-Cam and HSC survey volumes (Section 2.2) based on the areas in which we distribute pseudo LAEs.

4.3 Cosmic Variance

To include field-to-field variation in the error bar of our Lyα LFs, we calculate the dimensionless cosmic variance uncertainty, $\sigma_{\rm g}$, with

$$\sigma_{\rm g} = b_{\rm g} \sigma_{\rm DM}(z, R), \tag{4.1}$$

where $b_{\rm g}$ and $\sigma_{\rm DM}(z, R)$ are the bias parameter of galaxies and the density fluctuation of dark matter in a sphere with a radius R at a redshift z, respectively. We estimate $\sigma_{\rm DM}(z, R)$ with the growth factor, following Carroll et al. (1992) with the transfer function given by Bardeen et al. (1986) (see also Mo & White 2002). Because our survey volume for $z = 2.2$ LAEs is 1.32×10^6 Mpc^{-3} (Section 2.2), the radius at $z = 2.2$ is $R = 68$ Mpc. The value of $\sigma_{\rm DM}(z, R)$ at $z = 2.2$ is estimated to be 0.055. Since Guaita et al. (2010) find the bias parameter of $b_{\rm g} = 1.8 \pm 0.3$ from the clustering analysis of $z = 2.1$ LAEs in the ECDF-S field, we adopt this value for $b_{\rm g}$ in Equation (4.1). We thus obtain the cosmic variance uncertainty of $\sigma_{\rm g} \simeq 0.099$ at $z = 2.2$. Similarly, the radius at $z = 7.3$ is $R = 39$ Mpc, and the value of $\sigma_{\rm DM}(z, R)$ at $z = 7.3$ is estimated to be 0.041. Because the bias parameter of $b_{\rm g} = 3.6 \pm 0.7$ is obtained for $z = 6.6$ LAEs (Ouchi et al. 2010), we adopt $b_{\rm g} \simeq 4$ for $z = 7.3$ LAEs under the assumption that $b_{\rm g}$ does not significantly evolve at $z = 6.6 - 7.3$. With this procedure, we estimate the cosmic variance uncertainty to be $\sigma_{\rm g} \simeq 0.16$. Note that the cosmic variance uncertainties at $z = 5.7$ and 6.6 will be negligibly small, because the survey areas of *NB816* and *NB921* are significantly large (13.8 and 21.2 deg^2, respectively; see Section 2.2). Thus, we do not calculate the cosmic variance at these redshifts.

4.4 Lyα Luminosity Functions and Comparison with Previous Studies

In this section, we present Lyα LFs at $z = 2.2$, 5.7, 6.6, and 7.3 based on LAE samples shown in Sections 3.1 and 3.2. Here, we first describe the procedures for the Lyα LF calculation. Because our Lyα LFs are derived with procedures common to all redshifts, one expects no systematic errors raised by the analysis technique for the comparison of the Lyα LF measurements. We calculate the Lyα EW$_0$ of LAEs from the aperture magnitudes of narrowband and broadband, and estimate the Lyα luminosities of LAEs with these EW$_0$ and the total magnitudes of narrowband. In the calculation of Lyα luminosities, we use (*NB*, *BB*) filter sets of (*NB387*, *B*), (*NB816*, *z*), (*NB921*, *z*), and (*NB101*, *z'*) for LAEs at $z = 2.2$, 5.7, 6.6, and 7.3, respectively. For the errors of the Lyα luminosities, we carry out Monte Carlo simulations under the assumption that the spectrum of LAEs has a Lyα line and $f_\nu = $ const. with the IGM absorption of Madau (1995), following the methods applied in Shimasaku et al. (2006); Ouchi et al. (2008, 2010). In the calculations for the Lyα luminosities, we

assume that Lyα emission is placed at the central wavelength of the narrow band. We derive the Lyα LFs of $z = 2.2$, 5.7, 6.6 and 7.3 LAEs in the same manner as Ouchi et al. (2008, 2010). We calculate the volume number densities of LAEs in each Lyα luminosity bin, dividing the numbers of observed LAEs by our survey volumes based on a top-hat filter transmission curve assumption. We correct these number densities for the detection completeness estimated in Sections 4.2.1 and 4.2.2. The error bars of the Lyα LF at $z = 2.2$ and 7.3 include uncertainties from Poisson statistics and cosmic variance obtained in Section 4.3. For the Poisson errors, we use the values in columns "0.8413" in Table 1 and 2 of Gehrels (1986) for the upper and lower limits of the Poisson errors, respectively. These values in columns "0.8413" correspond to the 1σ confidence levels for Gaussian statistics. We include only the Poisson errors in the Lyα LFs at $z = 5.7$ and 6.6, because the survey areas at these redshifts are very large (see Section 4.3). This procedure of Lyα LF derivation is known as the classical method. Note that there are two uncertainties of the Lyα LFs derived by the classical method. (1) A Lyα flux of an LAE at the fixed narrowband magnitude varies by the LAE's redshift. (2) A redshift distribution of LAEs depends on a Lyα EW. In order to evaluate such uncertainties, Shimasaku et al. (2006) and Ouchi et al. (2008) perform Monte Carlo simulations. In these simulations, they generate a mock catalog of LAEs with a set of Schechter parameters (ϕ^*, L^*, α) and a Gaussian σ for a probability distribution of Lyα EW_0, and uniformly distribute the LAEs of the mock catalog in a comoving volume over the redshift range that a narrowband covers. They "observe" these LAEs with the narrow and broad bands to be the same as the real band response. They select LAEs using the same criteria as was used for selecting the actual LAEs and derive the number densities and color distributions from the mock catalog. By comparing the results of these simulations with the observational results, they find the best-fit Schechter parameters of Lyα LFs (see Shimasaku et al. 2006; Ouchi et al. 2008, for more details of the simulations). They confirm that the LFs estimated from the simulations are consistent with those derived by the classical method.

To parameterize our Lyα LFs, we fit a Schechter function (Schechter 1976) to our $z = 2.2$, 5.7, 6.6, and 7.3 Lyα LFs by minimum χ^2 fitting. The Schechter function is defined by Equation (1.1) in Section 1.1.2. In the calculations for the χ^2 values, we adopt an upper error as 1σ in the case that models are beyond the data point of our LF. Similarly, a lower error is adopted in the case that models are below the data point

of our LF. We determine three parameters of the Schechter function simultaneously for our $z = 2.2$ Lyα LFs, while we fix the faint-end slope, α in Equation (1.1), for the Lyα LFs at $z = 5.7$, 6.6, and 7.3. Because, except at $z = 2.2$, the Lyα LFs do not reach a Lyα luminosity limit fainter than $\sim L^*_{\rm Ly\alpha}$ at $z \sim 2-6$, we cannot strongly constrain the α values of our $z = 5.7$, 6.6, and 7.3 Lyα LFs. Thus, in the fitting of the Schechter function to Lyα LFs at $z = 5.7-7.3$, we fix the faint-end slope of $\alpha = -1.8$, which is consistent with that obtained with our $z = 2.2$ Lyα LF (see Section 4.4.1). We summarize best-fit Schechter parameters of Lyα LFs at $z = 2.2$, 5.7, 6.6, and 7.3 in Table 4.2. From next subsections, we describe the details of our Lyα LFs at each redshift.

4.4.1 Redshift 2.2

We derive the Lyα LFs at $z = 2.2$ from the full and EWgt60 samples, adopting the classical method of the Lyα LF derivation (Ouchi et al. 2010) whose accuracy is confirmed by Monte Carlo simulations (Shimasaku et al. 2006; Ouchi et al. 2008), as described above.

The top panel of Figure 4.4 presents the best estimate of our Lyα LF at $z = 2.2$ from the full sample. We also plot the Lyα LF measurements derived from each-field data. The best estimate Lyα LF covers a Lyα luminosity range of $\log L_{\rm Ly\alpha}$ [erg s^{-1}] $= 41.7 - 44.4$. Our Lyα luminosity limit of $\log L_{\rm Ly\alpha}$ [erg s^{-1}] = 41.7 (5.0×10^{41} erg s^{-1}) is one order of magnitude fainter than the $L^*_{\rm Ly\alpha}$ values at $z = 3-6$ ($\log L^*_{{\rm Ly\alpha},z=3-6}$ [erg s^{-1}] ~ 42.8; Shimasaku et al. 2006; Gronwall et al. 2007; Ouchi et al. 2008).

For our fitting with the Schechter function, we use Lyα LF measurements from the studies of ours, Blanc et al. (2011), and Cassata et al. (2011). We do not include the results from the other studies, because there exist unknown systematics that is discussed below. We determine three parameters of the Schechter function simultaneously, and obtain the best-fit Schechter parameters of $\alpha = -1.75^{+0.10}_{-0.09}$, $L^*_{\rm Ly\alpha} = 5.29^{+1.67}_{-1.13} \times 10^{42}$ erg s^{-1} and $\phi^*_{\rm Ly\alpha} = 6.32^{+3.08}_{-2.31} \times 10^{-4}$ Mpc^{-3}. This is the first time to determine three Schechter function parameters with no fixed parameter(s), and the faint-end slope of α is reasonably well constrained. Tables 4.2 and 4.3 present these best-fit Schechter parameters. We show the best-fit Schechter function in the top panel of Figure 4.4, and error contours of the Schechter parameters in Figure 4.5.

The top panel of Figure 4.4 shows an excess of the number densities beyond the best-fit Schechter function at the bright-end of $\log L_{\mathrm{Ly}\alpha}$ [erg s^{-1}] $\gtrsim$ 43.4. We refer to this excess as bright-end hump. In our Schechter function fit, we include the data of the bright-end hump. Because the errors of the Lyα LF at the faint end are significantly smaller than those at the bright end, the best-fit parameters are not significantly changed by the inclusion of the bright-end hump data (see footnote of Table 4.3).

Ouchi et al. (2008) find that there is a possible excess of the Lyα LFs at $z = 3.1$ and 3.7 similar to the bright-end hump, and claim that 100% of LAEs host AGNs at the bright ends of $\log L_{\mathrm{Ly}\alpha}$ [erg s^{-1}] > 43.6 and 43.4, respectively, based on the large-area LAE survey with the multiwavelength data set. Thus, the bright-end hump of our $z = 2.2$ Lyα LF may be produced by AGNs. To examine whether our LAEs at the bright end include AGNs, we use the multiwavelength data of X-ray, UV, and radio available in the SXDS, COSMOS, CDFS, HDFN, and SSA22 fields. For the X-ray data, we use the *XMM-Newton* source catalog in the SXDS field (Ueda et al. 2008), the *Chandra* 1.8 Ms catalog in the COSMOS field (Elvis et al. 2009), the *Chandra* 4 Ms source catalog in the CDFS field (Xue et al. 2011), and the *Chandra* 2 Ms catalog in the HDFN field (Alexander et al. 2003). The typical sensitivity limits of these X-ray data are $\sim 10^{-16}$ - 10^{-15} erg cm $^{-2}$ s^{-1} for the SXDS and COSMOS fields, and $\sim 10^{-17}$ - 10^{-16} erg cm $^{-2}$ s^{-1} for the CDFS and HDFN fields. We use *GALEX* FUV and NUV images for the UV data, and obtain these images from the Multimission Archive at STScI (see also Zamojski et al. 2007 for the COSMOS field). The *GALEX* images reach the 3σ detection limit of $\sim$ 25 - 26 mag. The Very Large Array 1.4 GHz source catalogs of Simpson et al. (2006) (SXDS), Schinnerer et al. (2007) (COSMOS), and Miller et al. (2013) (CDFS) are used for the radio data. These radio data reach an rms noise level of ~ 10 μJy beam^{-1}. We find that a majority of our bright LAEs are detected in the multiwavelength data, and summarize the numbers of these LAEs in Table 3.1. Under the column of "culled sample" in Table 3.1 , we show the numbers of LAEs with no counterpart detection(s) in the X-ray, UV, and radio data. As shown in Table 3.1, the SXDS and COSMOS fields have the data that cover all of the X-ray, UV, and radio wavelengths. Moreover, the X-ray, UV, and radio data spatially cover the entire fields of SXDS and COSMOS with the similar sensitivities. We make a subsample that is composed of all 1576 LAEs found in the SXDS and COSMOS fields, and refer to this subsample as SXDS+COSMOS/All. We then make another

subsample consisting of 1538 LAEs with no multiwavelength counterpart detection(s) in the SXDS and COSMOS fields, which is dubbed SXDS+COSMOS/Culled.

In the bottom panel of Figure 4.4, we plot the Lyα LFs derived from the subsamples of SXDS+COSMOS/All and SXDS+COSMOS/Culled. We fit the Schechter function to these Lyα LFs and the complementary Lyα LF data of Blanc et al. (2011) and Cassata et al. (2011), and presents the best-fit Schechter parameter sets and the error contours in Table 4.3 and Figure 4.5, respectively. Comparing the Lyα LF of the SXDS+COSMOS/All subsample with that of the full sample, in Figures 4.4 and 4.5, we find that the Lyα LF of the SXDS+COSMOS/All subsample is consistent with that of the full sample within the uncertainties. Figure 4.5 indicates that the Schechter fitting results of the full sample and the SXDS+COSMOS/All subsample are very similar with the one of the SXDS+COSMOS/Culled subsample, which are determined in the wide luminosity range of $\log L_{\mathrm{Ly}\alpha}$ [erg s^{-1}] $= 41.7 - 44.4$. However, there are no objects in SXDS+COSMOS/Culled subsample that has $\log L_{\mathrm{Ly}\alpha}$ [erg s^{-1}] > 43.4. The Lyα LF of SXDS+COSMOS/Culled subsample does not have a bright-end hump such found in those of the full sample and the SXDS+COSMOS/All subsample. These comparisons suggest that the bright-end hump of the $z = 2.2$ Lyα LF is originated from AGNs that are bright in the X-ray, UV, and/or radio wavelength(s). We discuss more details of the bright-end hump in Sections 7.1 and 7.2.

We compare our best-estimate Lyα LF with those from previous studies at $z \sim 2$. In Figure 4.6, we plot the Lyα LFs obtained by narrowband imaging surveys (Hayes et al. 2010; Ciardullo et al. 2012; see also Guaita et al. 2010) and blank-field spectroscopic surveys (Blanc et al. 2011; Cassata et al. 2011; Ciardullo et al. 2014). Hayes et al. (2010) carry out deep imaging with two narrowband filters covering Lyα and Hα lines, and report the Lyα LF as well as the Lyα escape fraction of $z = 2.2$ LAEs. Ciardullo et al. (2012) derive the Lyα LF of $z = 2.1$ LAEs based on the narrowband data of Guaita et al. (2010). In both studies, the Lyα EW criterion of narrowband excess colors is $\mathrm{EW}_0 = 20$Å, comparable to our studies. Blanc et al. (2011) and Ciardullo et al. (2014) obtain the Lyα LFs by the spectroscopic observations of the Hobby Eberly Telescope Dark Energy Experiment (HETDEX) Pilot Survey for LAEs at $1.9 < z < 3.8$ and $1.90 < z < 2.35$, respectively. Cassata et al. (2011) make a spectroscopic sample of LAEs at $2 < z < 6.6$ with the VIMOS VLT Deep Survey. In these spectroscopic surveys, most of LAEs have a Lyα EW greater than 20Å. Table 4.4 summarizes the best-fit Schechter parameters (and Lyα

luminosity ranges of the observations) given by our and the previous studies.

In Figure 4.6 and Table 4.4, we find that our $z = 2.2$ Lyα LF is generally consistent with those of the previous studies in the measurement ranges of the Lyα luminosity overlaps. However, there exist some noticeable differences. The Lyα LF of Ciardullo et al. (2012) is not similar to ours and Blanc et al. (2011) at the bright end, but similar to ours and Cassata et al. (2011) at the faint end. In contrast, the Lyα LF of Ciardullo et al. (2014) is not consistent with ours and Cassata et al. (2011) at the faint end, but consistent with ours and Blanc et al. (2011) at the bright end. Because Ciardullo et al. (2012) and Ciardullo et al. (2014) cover the reasonably wide Lyα luminosity ranges of $42.1 < \log L_{\mathrm{Ly}\alpha}$ [erg s^{-1}] < 42.7 and $41.9 < \log L_{\mathrm{Ly}\alpha}$ [erg s^{-1}] < 43.7, respectively, the origins of these differences at the bright and faint ends are not clear.

As clarified in Table 4.4, most of the previous studies fit the Schechter function to their Lyα LFs, assuming a fixed parameter. Hayes et al. (2010) constrain three Schechter parameters simultaneously, but the uncertainties of these parameters are large due to small statistics (see also Gronwall et al. 2007 for $z \sim 3$). Our study constrains three Schechter parameters simultaneously, using the large LAE sample of 3137 LAEs covering the wide Lyα luminosity range ($\log L_{\mathrm{Ly}\alpha}$ [erg s^{-1}] $= 41.7 - 44.4$).

4.4.2 Redshift 5.7

The blue filled circles in Figure 4.7 represent our $z = 5.7$ Lyα LF, which is derived from the Subaru/HSC data. Here, we correct the $z = 5.7$ Lyα LFs for the f_{cont} value (Section 4.1.2). Our Lyα LF covers a Lyα luminosity range of $\log L(\mathrm{Ly}\alpha)$ [erg s^{-1}] $= 42.9 - 43.8$. This luminosity range is relatively brighter than those of previous studies (e.g., Shimasaku et al. 2006; Ouchi et al. 2008; Hu et al. 2010), because bright LAEs can be efficiently identified by the wide-area survey with Subaru/HSC.

For the fitting of our Lyα LF with the Schechter function, we include the faint-end Lyα LF of Ouchi et al. (2008). This is because the faint-end Lyα LF of Ouchi et al. (2008) covers a faint Lyα luminosity range of $\log L(\mathrm{Ly}\alpha)$ [erg s^{-1}] $= 42.4 - 42.8$ that we do not reach, and our Lyα LF is derived by following the procedure of Ouchi et al. (2008). The faint-end Lyα LF data points are also corrected for the f_{cont} value (Section 4.1.2). Similarly, in our fitting for the $z = 6.6$ Lyα LF, we include the faint-end Lyα LF of Ouchi et al. (2010) ($\log L(\mathrm{Ly}\alpha)$ [erg s^{-1}] $= 42.4 - 43.0$; see

Section 4.4.3). Again, as described above, we fix a power-law slope of $\alpha = -1.8$ for the fitting to our $z = 5.7$ Lyα LF. We obtain the best-fit Schechter parameters of $L^*_{\mathrm{Ly}\alpha} = 8.92^{+0.99}_{-0.89} \times 10^{42}$ erg s^{-1} and $\phi^*_{\mathrm{Ly}\alpha} = 2.21^{+0.68}_{-0.50} \times 10^{-4}$ Mpc^{-3} with the fixed $\alpha = -1.8$. We list these best-fit parameters in Table 4.2, and show the best-fit Schechter function in Figure 4.7. Interestingly, from our $z = 5.7$ Lyα LF data points and best-fit Schechter function in Figure 4.7, we find no significant bright-end hump at $z = 5.7$, although there is such a bright-end hump in our $z = 2.2$ Lyα LF shown in Section 4.4.1.

We compare our Lyα LF at $z = 5.7$ with those obtained by previous studies in Figure 4.7, and find that our Lyα LF is generally consistent with those of the previous studies.

4.4.3 Redshift 6.6

In Figure 4.8, the red filled circles show our Lyα LF at $z = 6.6$ with the contamination correction, which is derived from the Subaru/HSC data. Our $z = 6.6$ Lyα LF covers a bright Lyα luminosity range of $\log L(\mathrm{Ly}\alpha)$ [erg s^{-1}] $= 43.0 - 43.8$ due to the Subaru/HSC survey with a wide-field area of 21.2 deg^2.

Again, for the fitting of the Schechter function to our $z = 6.6$ Lyα LF, we include the faint-end Lyα LF data points ($\log L(\mathrm{Ly}\alpha)$ [erg s^{-1}] $= 42.4 - 43.0$) of Ouchi et al. (2010), which is corrected for the f_{cont} value. We fix a power-law slope of $\alpha = -1.8$, as described above, and obtain the best-fit Schechter parameters of $L^*_{\mathrm{Ly}\alpha} = 6.42^{+0.74}_{-0.59} \times 10^{42}$ erg s^{-1} and $\phi^*_{\mathrm{Ly}\alpha} = 2.51^{+0.83}_{-0.68} \times 10^{-4}$ Mpc^{-3}. Table 4.2 lists these best-fit parameters. We present the best-fit Schechter function with the red thick solid line in Figure 4.8. Comparing our $z = 6.6$ Lyα LF measurements with the best-fit Schechter function in Figure 4.8, we find that there is a significant bright-end hump of the $z = 6.6$ Lyα LF at $\log L_{\mathrm{Ly}\alpha}$ [erg s^{-1}] $\gtrsim 43.5$ at the 4.0σ confidence level. Based on the results shown in Sections 4.4.1 and 4.4.2, the bright-end hump in Lyα LFs emerges at $z = 6.6$, and disappears at $z = 5.7$. Then, the hump appears again at $z = 2.2$. We discuss more details of the bright-end hump found in our $z = 6.6$ Lyα LF in Section 7.1.

We compare our Lyα LF at $z = 6.6$ with those obtained by previous studies in Figure 4.8, and find that our Lyα LF is generally consistent with those of the previous studies.

4.4.4 Redshift 7.3

Figure 4.9 presents the Lyα LF of our $z = 7.3$ LAEs in the entire fields of SXDS and COSMOS. In Figure 4.9, we plot the Lyα LFs from two independent fields of SXDS and COSMOS. Because these Lyα LFs are consistent within the statistical+cosmic variance uncertainties in these fields, we confirm that our errors of the entire-field Lyα LF explain the cosmic variance effects based on the real observational data of SXDS and COSMOS on the independent sky. Here, we correct the Lyα LF at $z = 7.3$ with the $f_{\rm cont}$ value same as that of $z = 5.7$ and 6.6 (30%; see Section 4.1.2), because spectroscopic follow-up observations have not been sufficiently conducted for the LAE sample. We regard this contamination rate of $f_{\rm cont} = 30\%$ as the representative value.

We fit the Schechter function to our $z = 7.3$ Lyα LF by minimum χ^2 fitting. Again, because the Lyα luminosity range of our LF is not wide, the parameter of α in the Schechter function cannot be determined. We fix a power-law slope of $\alpha = -1.8$, which is derived from our $z = 2.2$ Lyα LF in Section 4.4.1. We obtain the best-fit Schechter parameters of $L^*_{\rm Ly\alpha} = 3.23^{+25.0}_{-1.63} \times 10^{42}$ erg s^{-1} and $\phi^* = 1.97^{+12.3}_{-1.89} \times 10^{-4}$ Mpc^3 with the fixed $\alpha = -1.8$, and present these best-fit values in Table 4.2. The best-fit Schechter function is shown in Figure 4.9 with the red solid line.

We compare our $z = 7.3$ Lyα LF with those obtained by previous studies for LAEs at $z = 7.0 - 7.7$, assuming that the Lyα LF does not significantly evolve at $z = 7.3 \pm 0.4$. In Figure 4.10, we plot the previous Subaru measurements of the Lyα LF at $z = 7.0$ (Iye et al. 2006; Ota et al. 2008, 2010) and 7.3 (Shibuya et al. 2012) that include spectroscopic results. These previous Subaru results are consistent with the bright-end of our Lyα LF within the uncertainties, while these previous Subaru studies typically reach $L({\rm Ly\alpha}) \sim 10^{43}$ erg s^{-1} that is significantly shallower than our ultra-deep survey. Similarly, the black solid line of Figure 4.10 presents the upper limits of the Lyα LF given by the VLT observations that identify no LAEs at $z = 7.7$ (Clément et al. 2012). These upper limits of the Lyα LF are consistent with our results.

On the other hand, we find discrepancies between these Subaru+VLT results including ours and the previous 4m-telescope results of $z = 7.7$ LAEs that are reported by Hibon et al. (2010), Tilvi et al. (2010), and Krug et al. (2012). In Figure 4.10, the number densities of the Lyα LF of the 4m-telescope results are about a factor of several or an order of magnitude larger than those of the Subaru+VLT results beyond

the uncertainties. We discuss these discrepancies of $z \simeq 7.3$ Lyα LF measurements between the Subaru+VLT and 4m-telescope results. There is a possibility to explain the discrepancies by the cosmic variance effects. However, all of these 4m-telescope LF measurements fall above the Subaru+VLT LF estimates. It is difficult to reconcile all of the 4m-telescope measurements by the chance fluctuations of cosmic variance. Another possibility is contamination. Clément et al. (2012) mention the results of the VLT/X-Shooter spectroscopic follow-up observations for the brightest five out of seven photometric LAE candidates of Hibon et al. (2010), and report that no Lyα emission lines from these Hibon et al.'s candidates are identified (see J. G. Cuby et al. in preparation). More recently, Faisst et al. (2014) conduct the spectroscopic follow-up observations for the brightest two out of four photometric candidates of Krug et al. (2012), and they detect no Lyα emission line from the Krug et al.'s candidates (see also Jiang et al. 2013). There is a similar spectroscopic study that reports no detection of Lyα from $z > 7$ LAEs whose sample is made with 4m-telescope data (Matthee et al. 2014). Thus, the photometric samples of Hibon et al. (2010) and Krug et al. (2012) include a significant number of contamination sources that are probably more than a half of their LAE candidates, which are indicated by the spectroscopic follow-up studies. Spectroscopic observations for the LAE candidates of Tilvi et al. (2010) have not been carried out so far. However, it is possible that the Tilvi et al.'s sample includes a large number of contamination, because of the sample selection from the 4m-telescope data similar to those of Hibon et al. (2010) and Krug et al. (2012). We conclude that our Lyα LF is consistent with those from the Subaru and VLT studies whose results are supported by the spectroscopic observations (Iye et al. 2006; Ota et al. 2008, 2010; Shibuya et al. 2012; Clément et al. 2012), and that our Lyα LF agrees with the results of the recent deep spectroscopic follow-up observations for the LAE candidates from the 4m-telescope data (Clément et al. 2012; Faisst et al. 2014; Jiang et al. 2013).

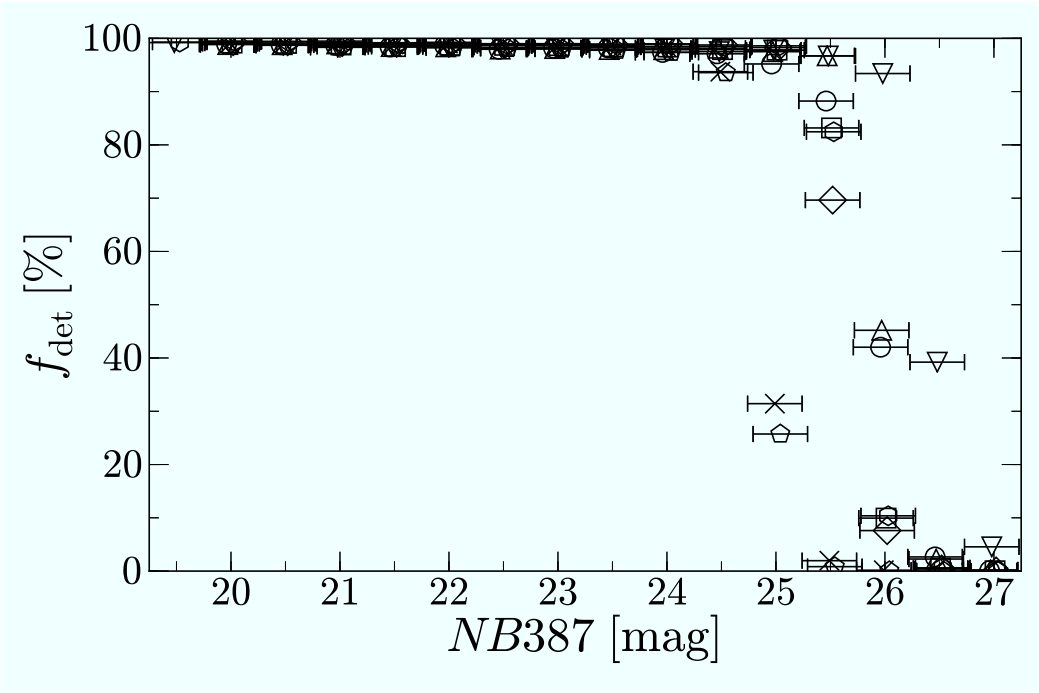

Figure 4.1 Detection completeness, $f_{\rm det}$, of our *NB387* images taken with Subaru/Suprime-Cam. The symbols represent the completeness in a magnitude bin of $\Delta m = 0.5$ mag for the SXDS-C (squares), SXDS-N (diamonds), SXDS-S (hexagons), SXDS-W (pentagons), COSMOS (circles), CDFS (inverted triangles), HDFN (triangles), and SSA22 (cross marks) fields. For presentation purposes, we slightly shift all the points along the abscissa.

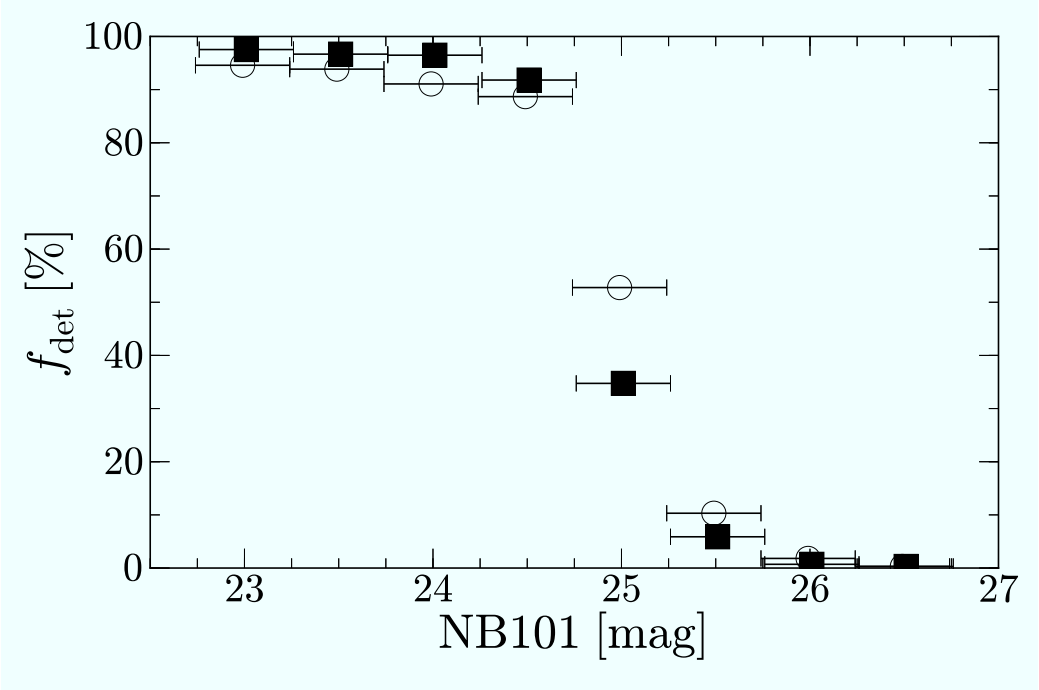

Figure 4.2 Same as Figure 4.1, but for our *NB101* images of Subaru/Suprime-Cam. The filled squares and open circles represent the completeness in the SXDS and COSMOS fields, respectively.

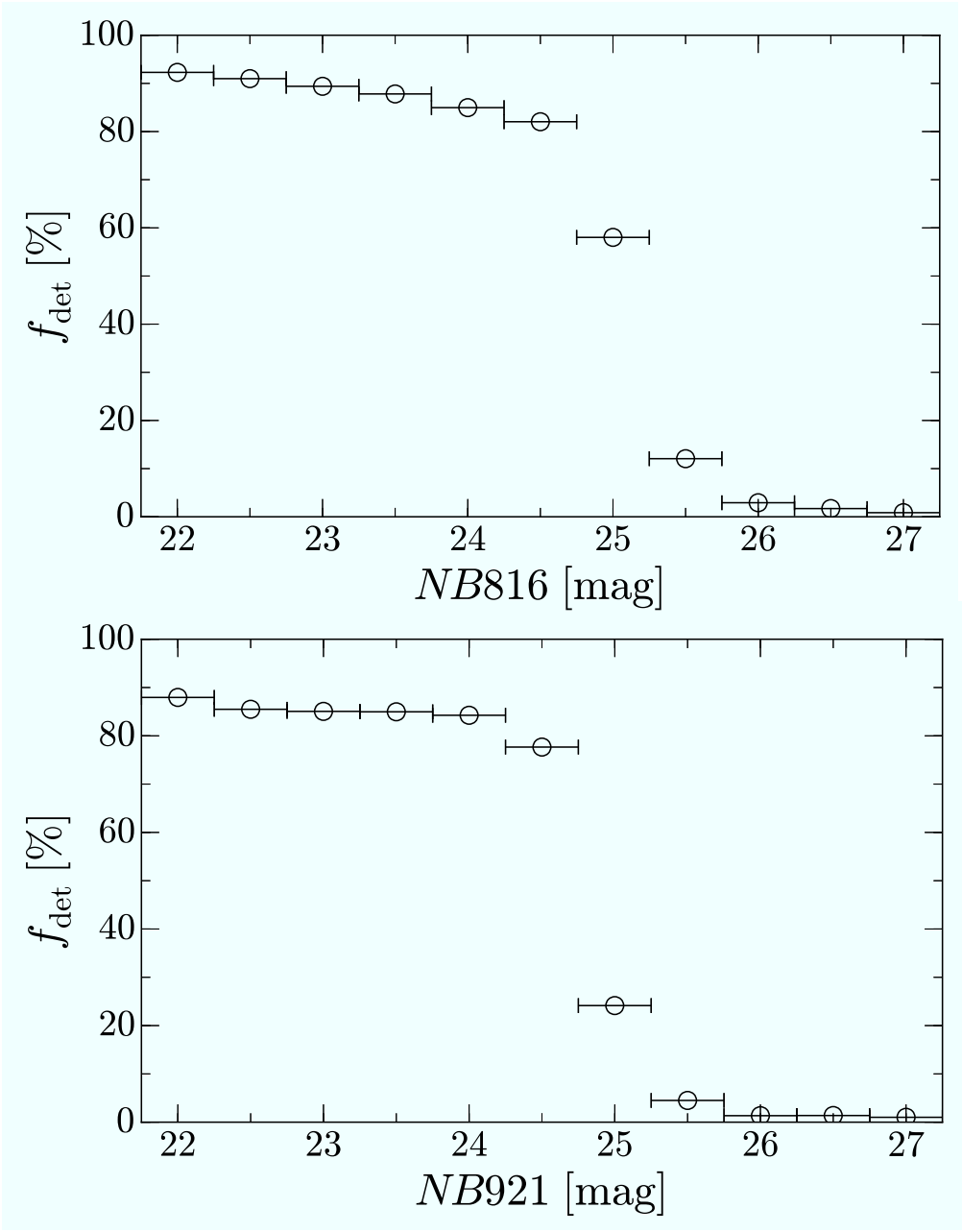

Figure 4.3 Same as Figures 4.1 and 4.2, but for the *NB816* (top) and *NB921* (bottom) images taken with Subaru/HSC. The open circles in the top and bottom figures represent the completeness in the D-DEEP2-3 field, where the 5σ limiting magnitudes of the *NB816* and *NB921* images are 25.2 and 24.9, respectively.

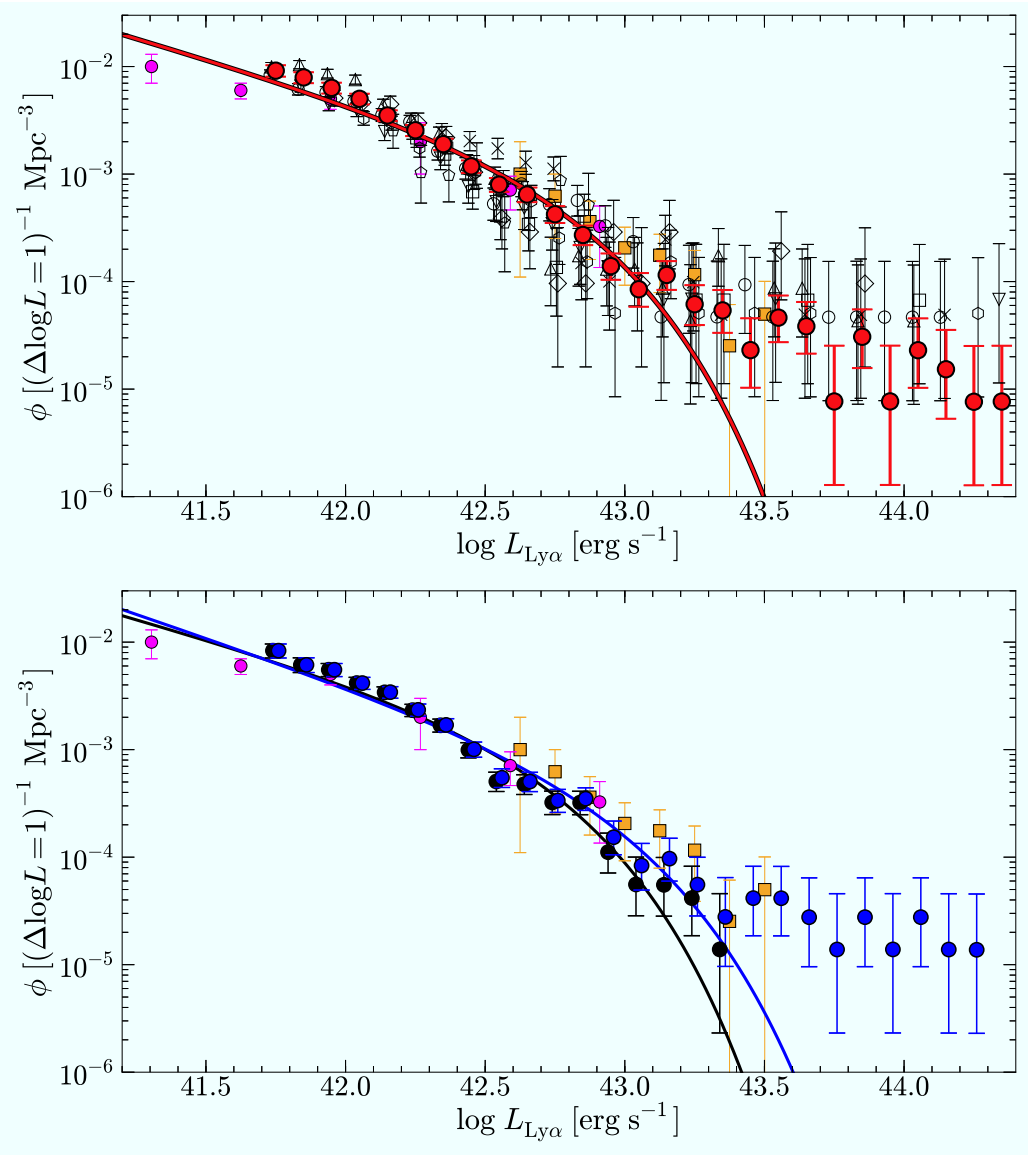

Figure 4.4 *Top*: Lyα LFs of our $z = 2.2$ LAEs with a luminosity bin of $\Delta \log L_{\mathrm{Ly}\alpha} = 0.1$. The red filled circles represent the Lyα LF derived from the full sample and the red solid curve denotes the best-fit Schechter function. The black open symbols show the Lyα LFs in the SXDS-C (squares), SXDS-N (diamonds), SXDS-S (hexagons), SXDS-W (pentagons), COSMOS (circles), CDFS (inverted triangles), HDFN (triangles), and SSA22 (cross marks) fields. For clarity, we slightly shift all the points along the abscissa. The magenta filled circles and orange filled squares are the results from Cassata et al. (2011) and Blanc et al. (2011), respectively. *Bottom*: Lyα LFs at $z = 2.2$ derived from the SXDS and COSMOS fields. The blue and black filled circles represent the Lyα LFs from the SXDS+COSMOS/All and SXDS+COSMOS/Culled subsamples, respectively. The blue and black solid curves show the best-fit Schechter functions of our best-estimate Lyα LFs using the SXDS+COSMOS/All and SXDS+COSMOS/Culled subsamples, respectively. The magenta filled circles and orange filled squares are the same as the top panel of this figure.

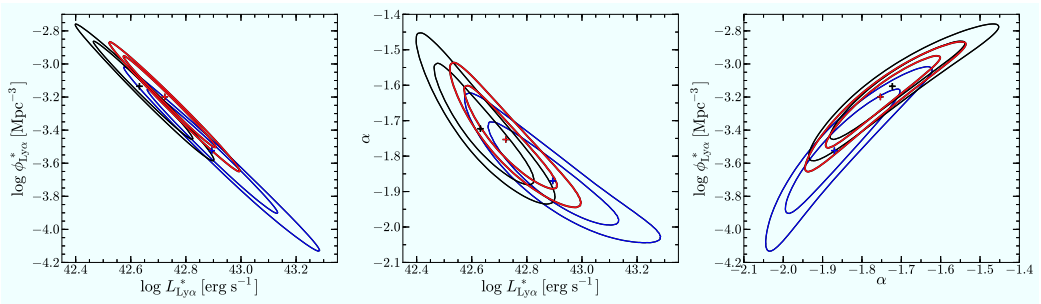

Figure 4.5 Error contours of Schechter parameters, $L^*_{\mathrm{Ly}\alpha}$, $\phi^*_{\mathrm{Ly}\alpha}$ and α. The red contours represent our best-estimate Lyα LF based on the full sample. The blue and black contours show our best-estimate Lyα LFs using the SXDS+COSMOS/All and SXDS+COSMOS/Culled subsamples, respectively. The inner and outer contours denote the 68% and 90% confidence levels, respectively. The red, blue and black crosses are the best-fit Schechter parameters for our best-estimate Lyα LFs based on the full sample, SXDS+COSMOS/All subsample, and SXDS+COSMOS/Culled subsample, respectively.

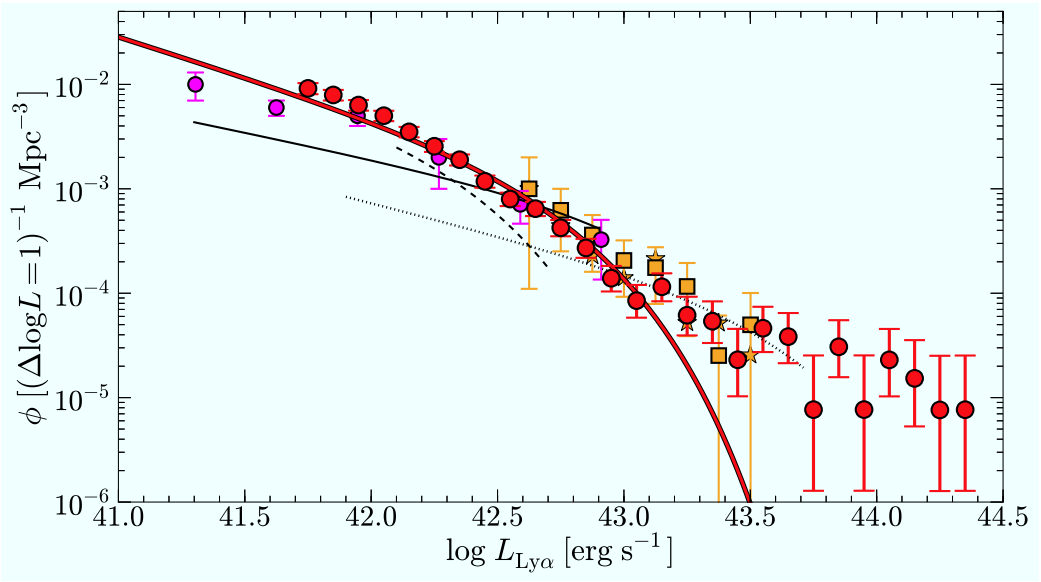

Figure 4.6 Comparison of our $z = 2.2$ Lyα LF with the previous measurements of Lyα LF at $z \sim 2$. The red filled circles denote our Lyα LF and the red solid curve is the best-fit Schechter function, which are the same as the top panel of Figure 4.4. The magenta filled circles represent the Lyα LF given by Cassata et al. (2011) at $2 < z < 3.2$. The orange stars and squares show the LFs by Blanc et al. (2011) based on the spectroscopic surveys of LAEs at $1.9 < z < 2.8$ and $1.9 < z < 3.8$, respectively. The black solid, dashed, and dotted lines are the best-fit Schechter functions obtained by Hayes et al. (2010), Ciardullo et al. (2012), and Ciardullo et al. (2014), respectively. Since the previous Lyα LF estimates are limited in the ranges of $\log L_{\mathrm{Ly}\alpha}$ [erg s^{-1}] $= 41.3 - 42.9$ (Hayes et al. 2010), $42.1 - 42.7$ (Ciardullo et al. 2012), and $41.9 - 43.7$ (Ciardullo et al. 2014), we show the black lines within these ranges.

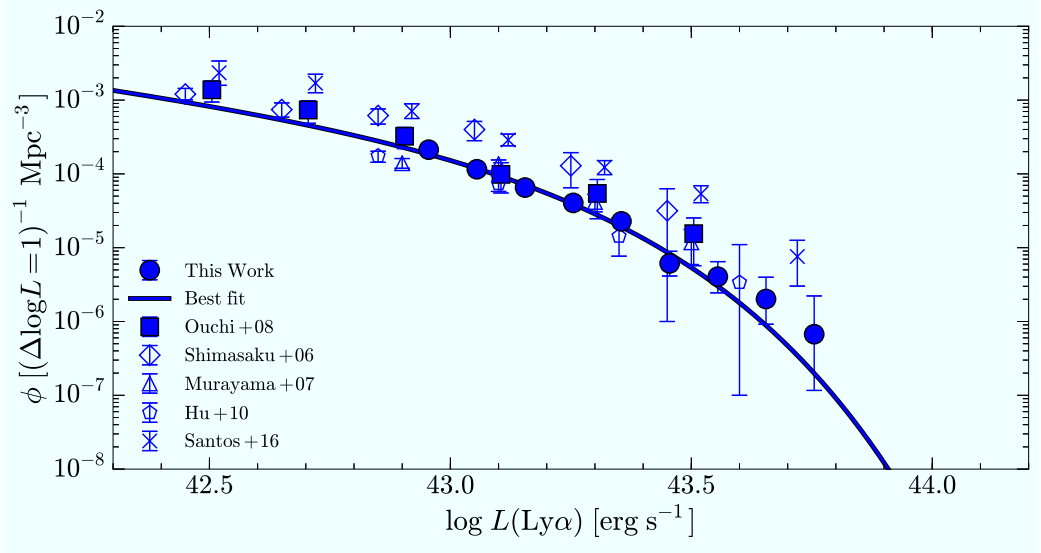

Figure 4.7 Lyα LFs of $z = 5.7$ LAEs. The blue filled circles represent our $z = 5.7$ Lyα LF derived with the Subaru/HSC data, and the blue filled squares denote the Lyα LF given by Ouchi et al. (2008). The blue open diamonds, triangles, pentagons, and crosses are the Lyα LFs of Shimasaku et al. (2006), Murayama et al. (2007), Hu et al. (2010), and Santos et al. (2016), respectively. The best-fit Schechter function for the Lyα LFs of our and Ouchi et al.'s studies are shown with the blue solid curve.

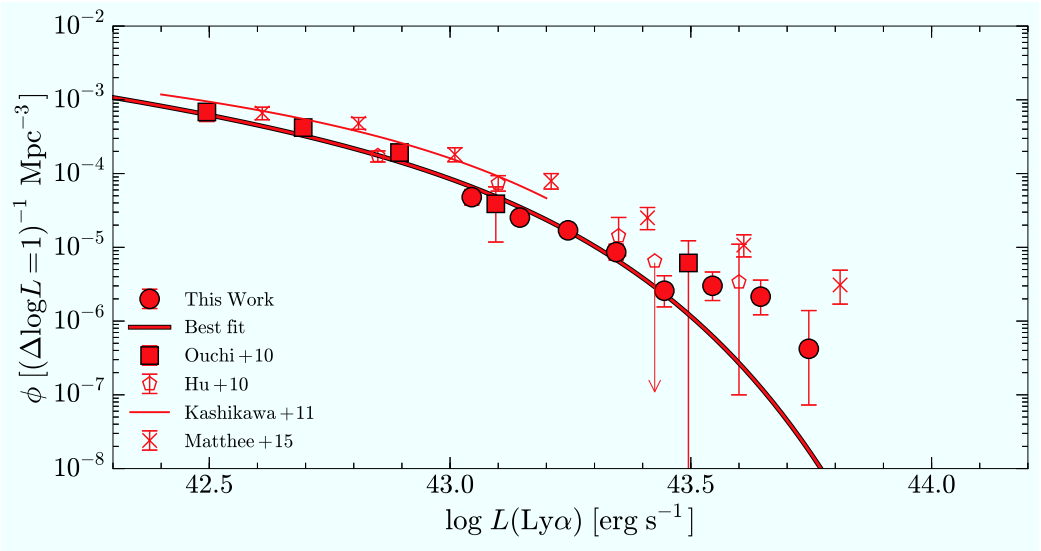

Figure 4.8 Lyα LFs of $z = 6.6$ LAEs. The red filled circles represent our $z = 6.6$ Lyα LF derived with the Subaru/HSC data, and the red filled squares denote the Lyα LF given by Ouchi et al. (2010). The red open pentagons and crosses are the Lyα LFs of Hu et al. (2010), and Matthee et al. (2015), respectively. The red thin line is the best-fit Schechter function obtained by Kashikawa et al. (2011). The best-fit Schechter functions for the Lyα LFs of our and Ouchi et al.'s studies are shown with the red thick solid curve.

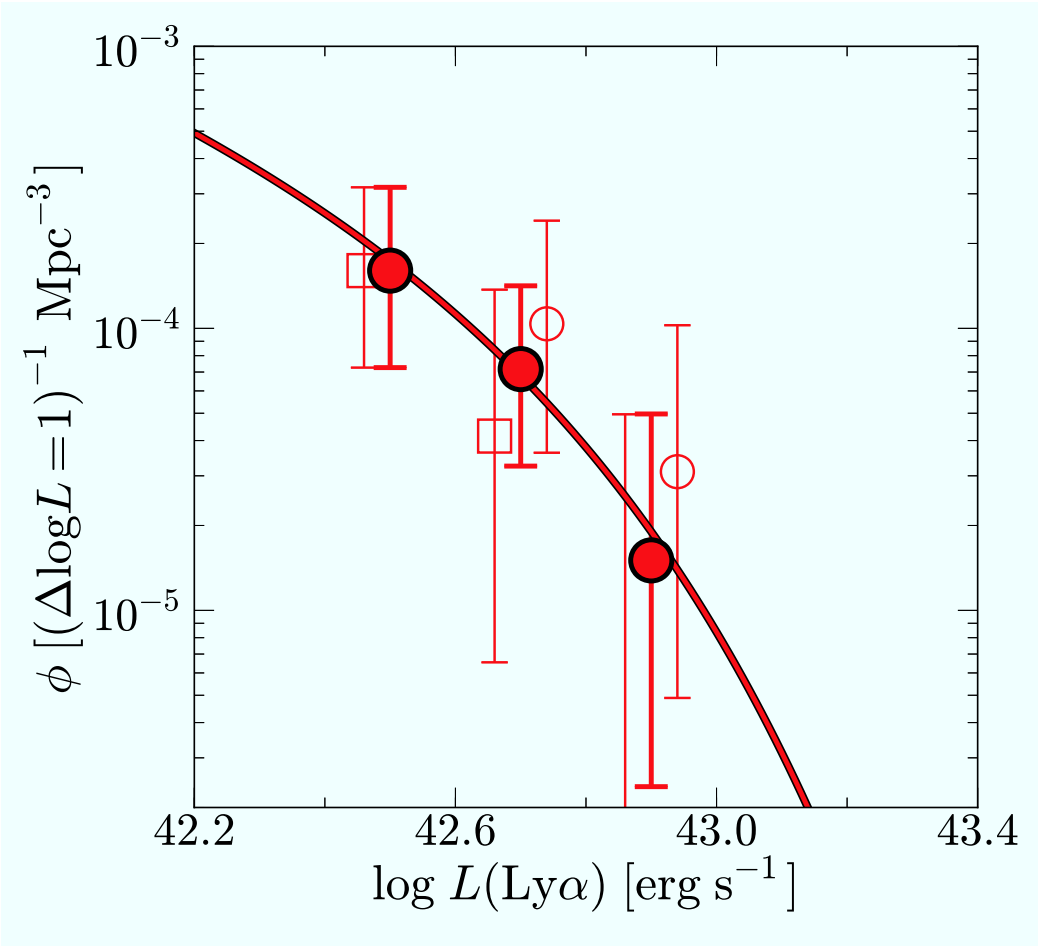

Figure 4.9 Lyα LFs of our $z = 7.3$ LAEs. The red filled circles represent the Lyα LF derived with the data of the entire fields, i.e. both the SXDS and COSMOS fields. The red open circles and squares denote our Lyα LFs estimated with the data of the SXDS and COSMOS fields, respectively. In the brightest luminosity bin, we also plot the upper error of the Lyα LF in COSMOS field. The best-fit Schechter function for the Lyα LF of the entire fields is shown with the red curve.

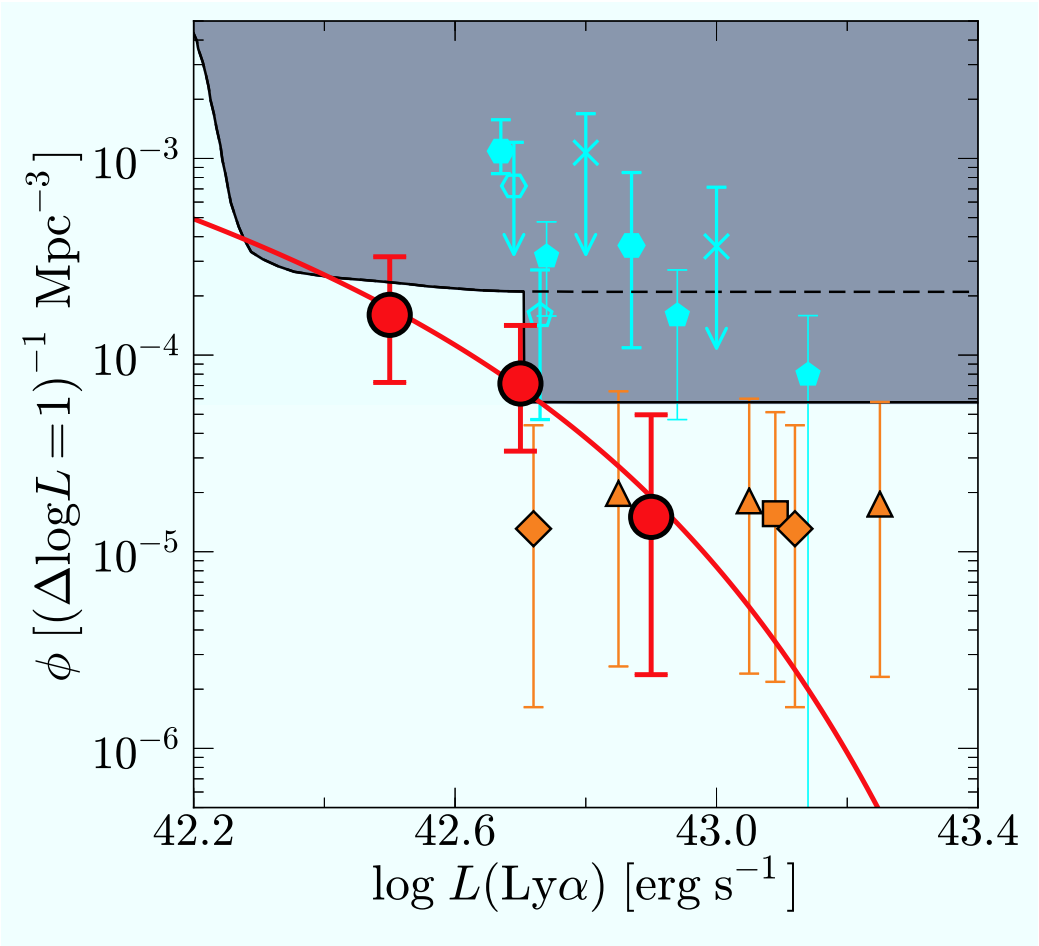

Figure 4.10 Comparison of our $z = 7.3$ Lyα LF with the previous measurements of Lyα LF at $z = 7.3 \pm 0.4$. The red circles denote our $z = 7.3$ Lyα LF, and the red curve is the best-fit Schechter function. The orange diamonds, square, and triangles represent the Subaru measurements of the Lyα LF at $z = 7.0 - 7.3$ given by Shibuya et al. (2012), Iye et al. (2006), and Ota et al. (2010), respectively. The gray region indicates the parameter space of $z = 7.7$ Lyα LF ruled out by the VLT observations (Clément et al. 2012). The black dashed line is the upper limit of the number density determined by the VLT photometric observations, while the black solid line represents the upper limits from the combination of the VLT photometric and spectroscopic data (Clément et al. 2012). The cyan filled pentagons, hexagons, and crosses denote the 4m-telescope estimates of the Lyα LF at $z = 7.7$ obtained by Hibon et al. (2010), Krug et al. (2012), and Tilvi et al. (2010), respectively. The cyan open pentagons and hexagons are the same as the cyan filled pentagons and hexagons, but for the results of no emission-line detection of the spectroscopic follow-up observations for the 4m-telescope samples, which are presented in Clément et al. (2012) and Faisst et al. (2014), respectively.

Table 4.1. Magnitudes of our $z = 7.3$ LAE Candidates in the Different Epoch

ID	*NB101*[a] (2010)[b]	*NB101*[a] (2012)[b]	*NB101*[a] (2013)[b]
NB101-SXDS-2904	$24.51^{+0.22}_{-0.18}$	$24.38^{+0.26}_{-0.21}$	—
NB101-SXDS-46782	$24.74^{+0.28}_{-0.22}$	$25.03^{+0.54}_{-0.36}$	—
NB101-SXDS-59407	$24.79^{+0.30}_{-0.23}$	$24.76^{+0.40}_{-0.29}$	—
NB101-COSMOS-5156	$25.03^{+0.31}_{-0.24}$	$24.65^{+0.71}_{-0.43}$	$24.86^{+0.40}_{-0.29}$
NB101-COSMOS-37050	$24.64^{+0.21}_{-0.17}$	$24.69^{+0.75}_{-0.44}$	$25.48^{+0.84}_{-0.47}$
NB101-COSMOS-37548	$25.19^{+0.37}_{-0.27}$	$24.07^{+0.36}_{-0.27}$	$24.92^{+0.42}_{-0.30}$
NB101-COSMOS-103966	$25.11^{+0.34}_{-0.26}$	$24.92^{+1.04}_{-0.52}$	$24.76^{+0.35}_{-0.27}$

[a]The magnitudes with the 1σ error measured with an aperture whose diameter is $2\times$ PSF FWHM.

[b]The values in parenthesis present the epochs of data used for the stacked images. 2010, 2012, and 2013 indicate the epochs of 2010 − 2011, 2012, and 2013 observing periods, respectively.

Table 4.2. Best-fit Schechter Parameters of Our Lyα LFs at $z = 2 - 7$

Redshift	α	$L^*_{\mathrm{Ly}\alpha}$ (10^{42} erg s^{-1})	$\phi^*_{\mathrm{Ly}\alpha}$ (10^{-4} Mpc^{-3})
2.2	$-1.75^{+0.10}_{-0.09}$	$5.29^{+1.67}_{-1.13}$	$6.32^{+3.08}_{-2.31}$
5.7	-1.8 (fix)	$8.92^{+0.99}_{-0.89}$	$2.21^{+0.68}_{-0.50}$
6.6	-1.8 (fix)	$6.42^{+0.74}_{-0.59}$	$2.51^{+0.83}_{-0.68}$
7.3	-1.8 (fix)	$3.23^{+25.0}_{-1.63}$	$1.97^{+12.3}_{-1.89}$

Table 4.3. Schechter Parameters for Full and Culled Samples at $z = 2.2$

Sample	α	$L^*_{\mathrm{Ly}\alpha}$ (10^{42} erg s^{-1})	$\phi^*_{\mathrm{Ly}\alpha}$ (10^{-4} Mpc^{-3})
Full[a,b]	$-1.75^{+0.10}_{-0.09}$	$5.29^{+1.67}_{-1.13}$	$6.32^{+3.08}_{-2.31}$
SXDS+COSMOS/All[c]	$-1.87^{+0.10}_{-0.08}$	$7.83^{+3.22}_{-2.34}$	$2.99^{+2.26}_{-1.27}$
SXDS+COSMOS/Culled[d]	$-1.72^{+0.12}_{-0.11}$	$4.28^{+1.47}_{-0.99}$	$7.33^{+3.89}_{-2.83}$

[a] The full sample, which is constructed from the SXDS, COSMOS, CDFS, HDFN, and SSA22 fields.

[b] In the case that we do not include the data at $\log L_{\mathrm{Ly}\alpha}$ [erg s^{-1}] > 43.4 with the bright-end hump for our fitting, the best-fit Schechter parameters are $\alpha = -1.72 \pm 0.09$, $L^*_{\mathrm{Ly}\alpha} = 4.80^{+1.21}_{-0.86} \times 10^{42}$ erg s^{-1} and $\phi^*_{\mathrm{Ly}\alpha} = 7.40^{+2.84}_{-2.31} \times 10^{-4}$ Mpc^{-3}.

[c] The sample of LAEs found in the SXDS and COSMOS fields.

[d] The sample of LAEs with no multiwavelength counterpart detection(s) in the SXDS and COSMOS fields.

Table 4.4. Schechter Parameters of Previous $z \sim 2$ LAE Studies

Study	α	$L^*_{\mathrm{Ly}\alpha}$ (10^{42} erg s^{-1})	$\phi^*_{\mathrm{Ly}\alpha}$ (10^{-4} Mpc^{-3})	$\log L_{\mathrm{Ly}\alpha}$ range
This work	$-1.75^{+0.10}_{-0.09}$	$5.29^{+1.67}_{-1.13}$	$6.32^{+3.08}_{-2.31}$	$41.7 - 44.4$
Hayes et al. (2010)	-1.49 ± 0.27	$14.5^{+15.7}_{-7.54}$	$2.34^{+5.42}_{-1.64}$	$41.3 - 42.9$
Blanc et al. (2011)	-1.7 (fixed)	$16.3^{+94.6}_{-10.8}$	$1.0^{+5.4}_{-0.9}$	$42.6 - 43.6$
Cassata et al. (2011)	-1.6 ± 0.12	5.0 (fixed)	$7.1^{+2.4}_{-1.8}$	$41.2 - 43.1$
Ciardullo et al. (2012)	-1.65 (fixed)	$2.14^{+0.68}_{-0.52}$	$13.8^{+1.7}_{-1.5}$	$42.1 - 42.7$
Ciardullo et al. (2014)	-1.6 (fixed)	$39.8^{+98.2}_{-16.4}$	0.36[a]	$41.9 - 43.7$

[a] Ciardullo et al. (2014) do not show the errors of $\phi^*_{\mathrm{Ly}\alpha}$, although they present the uncertainties of the total number densities of LAEs integrated down to $\log L_{\mathrm{Ly}\alpha}$ [erg s^{-1}] = 41.5, $\phi_{\mathrm{tot}} = 9.77^{+3.11}_{-2.36} \times 10^{-4}$ Mpc^{-3}.

CHAPTER 5
EVOLUTION OF LYα LUMINOSITY FUNCTION

5.1 Evolution of Lyα Luminosity Function at $z \sim 0-6$

In this section, we first examine the evolution of Lyα LFs at $z \sim 2-3$ and then investigate the evolution from $z \sim 0$ to 6 with the compilation of the Lyα LF data taken from the literature.

For the $z \sim 3$ data, we use the Lyα LF of Ouchi et al. (2008) corrected with the $f_{\rm cont}$ value (Section 4.1.2). This value is consistent with that obtained by their spectroscopic follow-up observations. The $z = 3.1$ Lyα LF of Ouchi et al. (2008) is derived in the same manner as ours (see Sections 4.2–4.4). Because the EW criterion of Ouchi et al. (2008) is EW $\gtrsim$ 60Å, we compare the Lyα LF obtained from our EWgt60 sample (Section 3.1). The Lyα LF and the best-fit Schechter function (parameters) for the EWgt60 sample are presented in the left panel of Figure 5.1 (Table 5.1). The left panel of Figure 5.1 indicates that the Lyα LFs increase from $z \sim 2$ to 3.

To quantify this evolutionary trend, we show the error contours of the Schechter parameters of our $z = 2.2$ Lyα LF (red contours) and the $z = 3.1$ Lyα LF (blue contours) in the right panel of Figure 5.1. Here, we apply our best-fit $z = 2.2$ Lyα LF slope of $\alpha = -1.8$ (Section 4.4.1) to the $z = 3.1$ LF result, because α is not determined in the $z = 3.1$ Lyα LF. Comparing the $z = 2.2$ and 3.1 error contours in the right panel of Figure 5.1, we find that the Lyα LF increases from $z = 2.2$ to 3.1 at the $> 90\%$ confidence level. However, this increase is not large, only within a factor of ~ 2 (see Table 5.1). Note that there exist no systematic errors raised by the analysis technique in the comparison of our $z = 2.2$ and Ouchi et al.'s $z = 3.1$ Lyα LFs, because our $z = 2.2$ Lyα LF is derived in the same manner as Ouchi et al. (2008) based on the similar Subaru narrowband data (Sections 4.2–4.4).

We extend our investigation of Lyα LF evolution from $z = 2-3$ to $z = 0-6$. The left panel of Figure 5.1 compares our best-estimate Lyα LF at $z = 2.2$ and 5.7 with the Lyα LFs at $z = 0.3$, 0.9, 3.1, 3.7 taken from the literature. The right panel of Figure 5.1 shows the error contours of our Schechter function fitting, where we fix the α value to our best-fit slope $\alpha = -1.8$ of our $z = 2.2$ Lyα LF. The Lyα LFs at $z = 0.3$ and 0.9 are derived by the spectroscopic surveys with the *GALEX* FUV and NUV grism data, respectively (Cowie et al. 2010; Barger et al. 2012). We show the Lyα

LF measurements at $z = 3.7$ given by Ouchi et al. (2008). The Lyα LF at $z = 3.7$ is also corrected for the $f_{\rm cont}$ value (Section 4.1.2). We summarize the best-fit Schechter parameters at $z = 0 - 6$ in Table 5.1. Note that $\rm EW_0$ limits for the selection of LAEs are $\rm EW_0 \gtrsim 10-30$Å for all of the samples listed in Table 5.1 except for those of Ouchi et al.'s $z = 3.1$ and 3.7 samples and our EWgt60 sample. In the right panel of Figure 5.1, there is a significant increase of Lyα LFs in $L^*_{\rm Ly\alpha}$ and/or $\phi^*_{\rm Ly\alpha}$ from $z \sim 0$ to 3, albeit with the uncertain decrease of $\phi^*_{\rm Ly\alpha}$ from $z = 0.3$ to 0.9, which is first claimed by Deharveng et al. (2008). The right panel of Figure 5.1 also suggests no significant evolution of the Lyα LFs at $z = 3 - 6$ that is concluded by Ouchi et al. (2008).

5.2 Decrease in Lyα Luminosity Function at $z > 6$

In this section, we first investigate the evolution of the Lyα LF at $z = 5.7-6.6$. Ouchi et al. (2008, 2010) derive the Lyα LFs at $z = 5.7$ and 6.6 based on their ~ 1 deg^2 narrowband imaging data taken with Subaru/Suprime-Cam, and find the decrease of the Lyα LF at $z = 5.7$ to 6.6. The same results are obtained by other previous studies (e.g., Kashikawa et al. 2006; Hu et al. 2010; Kashikawa et al. 2011; Santos et al. 2016). In Figure 5.2, we can find such evolution from our Lyα LFs at $z = 5.7$ and 6.6, which are obtained from the 13.8 and 21.2 deg^2 sky area of narrowband imaging survey with Subaru/HSC. To evaluate this evolution at $z = 5.7 - 6.6$ quantitatively, we investigate the error distribution of Schechter parameters. Because we fix the Schechter parameter of α to -1.8, we examine the error distribution of $L^*_{\rm Ly\alpha}$ and $\phi^*_{\rm Ly\alpha}$ with the fixed value of $\alpha = -1.8$. Figure 5.3 presents error contours of the Schechter parameters of our $z = 5.7$ and 6.6 Lyα LF shown with cyan and blue ovals, respectively. From this figure, the Schechter parameters of $z = 6.6$ LF are different from those of $z = 5.7$ Lyα LF, and that the Lyα LF decreases from $z = 5.7$ to 6.6 at the $> 90\%$ confidence level. Moreover, in Figure 5.2, the decrease of the Lyα LF from $z = 5.7$ to 6.6 can be seen in a faint Lyα luminosity range of $\log L(\rm Ly\alpha)$ [erg s^{-1}] $\lesssim 43.4$, while there is no evolution of the Lyα LF at the bright end ($\log L(\rm Ly\alpha)$ [erg s^{-1}] $\gtrsim 43.4$). This result is related to the emergence of the bright-end hump at $z = 6.6$, and is suggested by previous studies (e.g., Santos et al. 2016). The physical origin of the Lyα LF evolution at $z = 5.7 - 6.6$ will be discussed in Sections 7.1 and 7.4.

We examine whether the Lyα LF evolves from $z = 6.6$ to 7.3. As described

in Section 3.1, we reach the Lyα limiting luminosity of 2.4×10^{42} erg s^{-1} that is comparable with those of previous Subaru $z = 3.1 - 6.6$ studies (Shimasaku et al. 2006; Kashikawa et al. 2006, 2011; Ouchi et al. 2008, 2010; Hu et al. 2010). Moreover, the size of survey area for $z = 7.3$ LAEs, $\simeq 0.5$ deg^2, is comparable with these Subaru studies. Our ultra-deep observations in the large areas allow us to perform a fair comparison of the Lyα LFs at different redshifts. We compare our Lyα LF at $z = 7.3$ with those at $z = 5.7$ and 6.6 in Figure 5.4, and summarize the best-fit Schechter parameters at $z = 5.7$, 6.6, and 7.3 in Table 4.2. For the $z = 5.7$ and 6.6 data, we use our Lyα LF measurements based on the Subaru/HSC data. In Figure 5.4, we find a significant decrease of the Lyα LFs from $z = 6.6$ to 7.3 beyond the error bars. In our $z = 7.3$ LAE survey, we expect to find ~ 65 $z = 7.3$ LAEs in the case of no Lyα LF evolution from $z = 6.6$ to 7.3, but identify only 7 $z = 7.3$ LAEs by our observations that are about an order of magnitude smaller than the expected LAEs. To quantify this evolution, we evaluate the error distribution of Schechter parameters. Because we fix the Schechter parameter of α to -1.8, as described above, we examine the error distribution of $L^*_{\mathrm{Ly}\alpha}$ and $\phi^*_{\mathrm{Ly}\alpha}$ with the fixed value of $\alpha = -1.8$. Figure 5.3 shows error contours of the Schechter parameters of our $z = 7.3$ Lyα LF with red ovals as well as those of our $z = 5.7$ and 6.6 Lyα LF. Our measurements indicate that the Schechter parameters of $z = 7.3$ LF are different from those of $z = 6.6$ Lyα LF, and that the Lyα LF decreases from $z = 6.6$ to 7.3 at the $> 90\%$ confidence level. Because our $z = 7.3$ Lyα LF is derived with the same procedures as our $z = 5.7$ and 6.6 Lyα LFs, one expects no systematic errors raised by the analysis technique for the comparison of the $z = 5.7$, 6.6, and 7.3 results. From this aspect, it is reliable that the Lyα LF declines at $z = 5.7-6.6$ and $z = 6.6-7.3$ significantly. Moreover, from Figure 5.3, the Lyα LF evolution from $z = 5.7$ to 7.3 is dominated by $L^*_{\mathrm{Ly}\alpha}$ evolution rather than $\phi^*_{\mathrm{Ly}\alpha}$ evolution. The same discussion is also described in Section 6.2. Here, we also discuss the possibility of the LF decrease mimicked by our sample biases. In Section 3.1, we define the selection criterion of the rest-frame Lyα equivalent width of $\mathrm{EW}_0 \gtrsim 0$Å for our $z = 7.3$ LAEs. This criterion of the EW_0 limit is slightly different from that of the LAEs for the $z = 6.6$ Lyα LF estimates. However, the EW_0 limit for the $z = 6.6$ LAEs is $\mathrm{EW}_0 \gtrsim 14$Å (see Section 3.2) that is larger than our EW_0 limit of $z = 7.3$ LAEs. Because our EW_0 limit gives more $z = 7.3$ LAEs to our sample than that of $z = 6.6$ LAEs, the conclusion of the Lyα LF decrease from $z = 6.6$ to 7.3 is unchanged by the EW_0 limit.

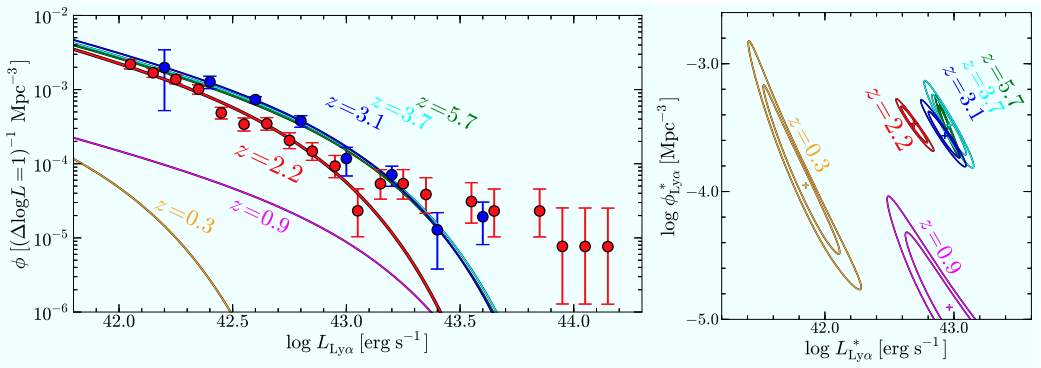

Figure 5.1 *Left*: Evolution of Lyα LF from $z = 0$ to 6. The red filled circles are our $z = 2.2$ Lyα LF of the EWgt60 sample, and the blue filled circles denote the LF at $z = 3.1$ derived by Ouchi et al. (2008). The orange, magenta, red, blue, cyan, and green curves show the best-fit Schechter functions of the Lyα LFs at $z = 0.3$ (Cowie et al. 2010), 0.9 (Barger et al. 2012), 2.2 (this work), 3.1, 3.7 (Ouchi et al. 2008), and 5.7 (this work), respectively. These Schechter functions are derived with a fixed slope value of $\alpha = -1.8$ that is the best-fit value of our $z = 2.2$ Lyα LF. *Right*: Error contours of Schechter parameters, $L^*_{\mathrm{Ly}\alpha}$ and $\phi^*_{\mathrm{Ly}\alpha}$. The orange, magenta, red, blue, cyan, and green contours represent the error contours of the Schechter parameters at $z = 0.3$, 0.9, 2.2, 3.1, 3.7, and 5.7, respectively. The inner and outer contours indicate the 68% and 90% confidence levels, respectively.

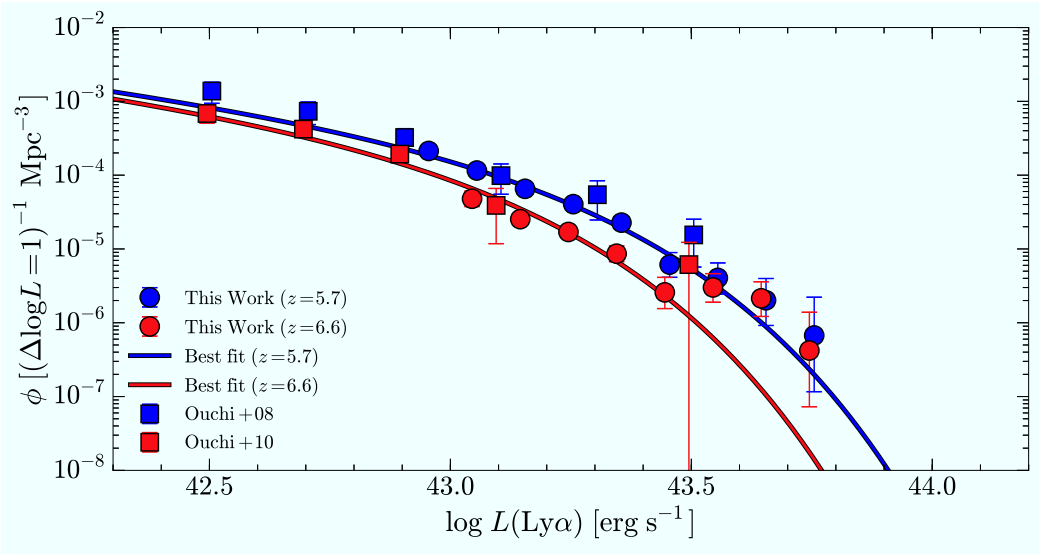

Figure 5.2 Evolution of Lyα LF at $z = 5.7$ and 6.6. The blue and red filled circles are our $z = 5.7$ and 6.6 Lyα LF measurements, respectively, which are derived from the Subaru/HSC data. The blue and red filled squares denote the $z = 5.7$ and 6.6 Lyα LF measurements with the Subaru/Suprime-Cam data given by Ouchi et al. (2008) and Ouchi et al. (2010), respectively. The best-fit Schechter function for the Lyα LF at $z = 5.7$ (6.6) is shown with the blue (red) solid curve.

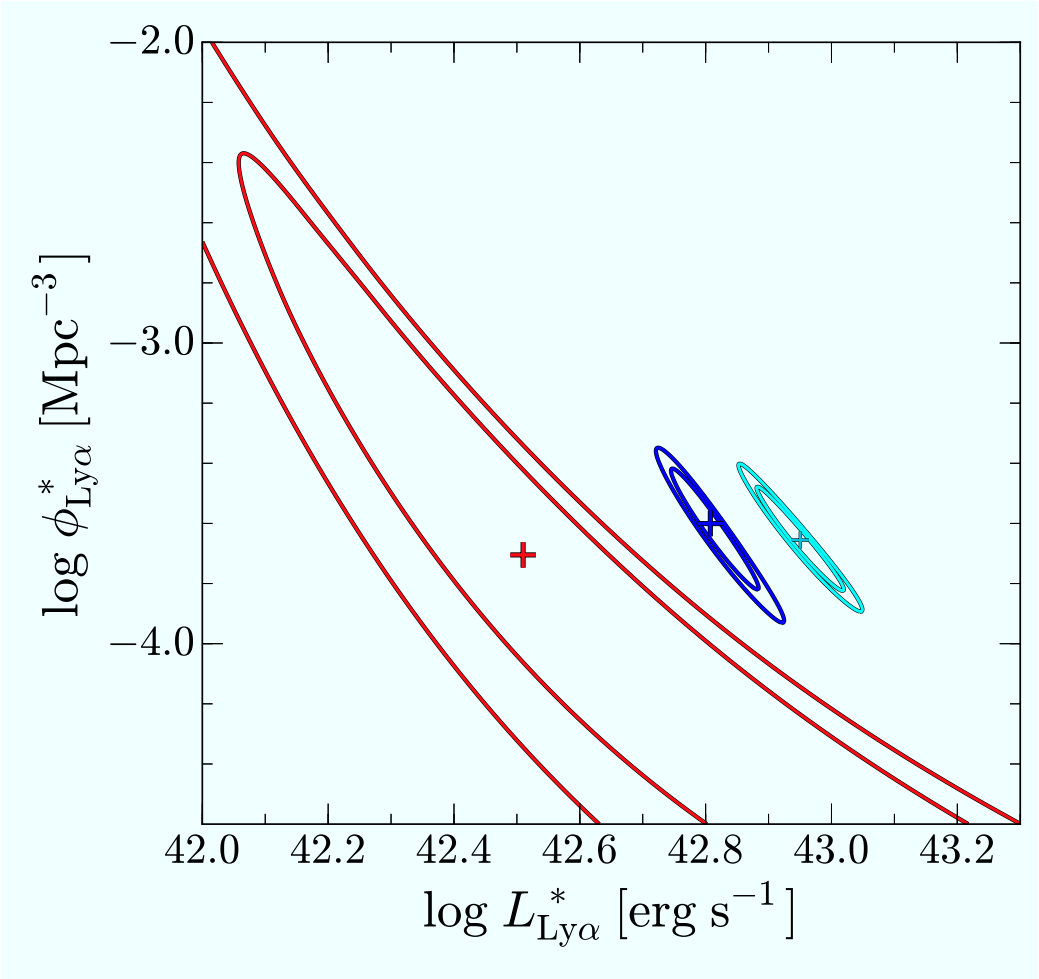

Figure 5.3 Error contours of Schechter parameters, $L^*_{\mathrm{Ly}\alpha}$ and $\phi^*_{\mathrm{Ly}\alpha}$. The red contours represent our Lyα LF at $z = 7.3$ derived with Subaru/Suprime-Cam, while the cyan and blue contours denote the ones at $z = 5.7$ and 6.6, respectively, obtained from the Subaru/HSC survey. The inner and outer contours indicate the 68% and 90% confidence levels, respectively. The cyan, blue, and red crosses show the best-fit Schechter parameters for the Lyα LFs at $z = 5.7$, 6.6, and 7.3, respectively.

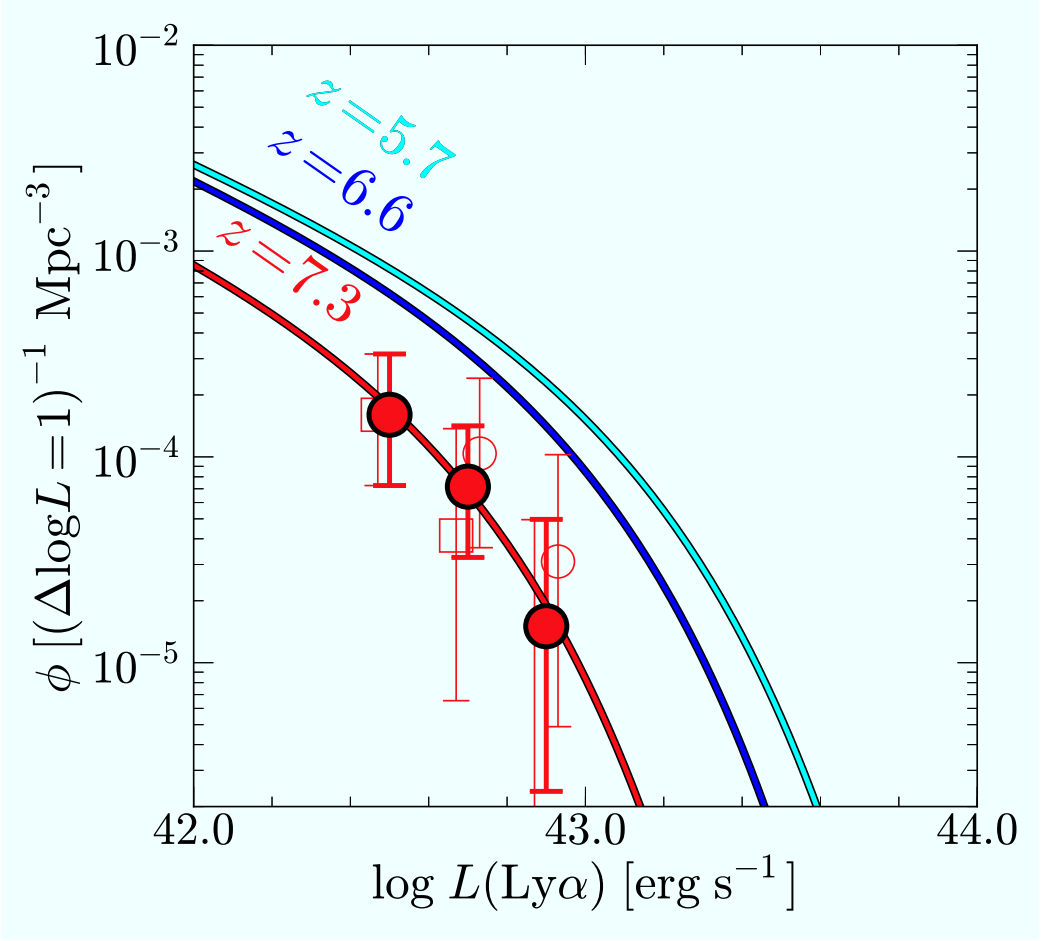

Figure 5.4 Evolution of Lyα LF at $z = 5.7 - 7.3$. The red filled circles are the best estimates of our $z = 7.3$ Lyα LF from the data of entire fields. The red open circles and squares denote our $z = 7.3$ Lyα LFs derived with the data of two independent fields of SXDS and COSMOS, respectively. The red curve is the best-fit Schechter function for the best estimate of our $z = 7.3$ Lyα LF. The cyan and blue curves are the best-fit Schechter functions of our Lyα LFs at $z = 5.7$ and 6.6 derived from the Subaru/HSC data, respectively.

Table 5.1. Best-fit Schechter Parameters and Lyα Luminosity Densities

Redshift	$L^*_{\mathrm{Ly}\alpha}$ (10^{42} erg s^{-1})	$\phi^*_{\mathrm{Ly}\alpha}$ (10^{-4} Mpc^{-3})	$\rho^{\mathrm{Ly}\alpha_{\mathrm{obs}}}$ [a] (10^{39} erg s^{-1} Mpc^{-3})	Reference
0.3	$0.71^{+0.32}_{-0.29}$	$1.12^{+2.45}_{-0.61}$	$0.055^{+0.019}_{-0.014}$	Cowie et al. (2010)
0.9	$9.22^{+15.6}_{-3.80}$	$0.12^{+0.18}_{-0.09}$	$0.165^{+0.067}_{-0.050}$	Barger et al. (2012)
2.2	$5.29^{+1.67}_{-1.13}$	$6.32^{+3.08}_{-2.31}$	$5.93^{+0.23}_{-0.22}$	This work (Best estimate)
2.2	$4.87^{+0.83}_{-0.68}$	$3.37^{+0.80}_{-0.66}$	$2.17^{+0.13}_{-0.13}$	This work (EWgt60 sample)
3.1	$8.49^{+1.62}_{-1.41}$	$2.73^{+0.86}_{-0.62}$	$4.92^{+0.41}_{-0.40}$	Ouchi et al. (2008)
3.7	$9.16^{+2.03}_{-1.67}$	$2.31^{+1.00}_{-0.69}$	$4.57^{+0.68}_{-0.61}$	Ouchi et al. (2008)
5.7	$8.92^{+0.99}_{-0.89}$	$2.21^{+0.68}_{-0.50}$	$4.23^{+0.65}_{-0.54}$	This work
6.6	$6.42^{+0.74}_{-0.59}$	$2.51^{+0.83}_{-0.68}$	$3.19^{+0.59}_{-0.54}$	This work
7.3	$3.23^{+25.0}_{-1.63}$	$1.97^{+12.3}_{-1.89}$	$1.03^{+1.85}_{-0.57}$	This work

Note. — For $z = 2.2$ (Best estimate), the best-fit Schechter parameters are determined with the full sample (Section 3.1), while for the other cases, $L^*_{\mathrm{Ly}\alpha}$ and $\phi^*_{\mathrm{Ly}\alpha}$ are derived with a fixed value of $\alpha = -1.8$, which is consistent with the best-fit value for our Lyα LF at $z = 2.2$. Note that EW_0 limits for the selection of LAEs at $z = 0.3$, 0.9, 2.2 (Best estimate), 2.2 (EWgt60 sample), 3.1, 3.7, 5.7, 6.6, and 7.3 are $\mathrm{EW}_0 = 15$, 20, $\sim 20 - 30$, 60, ~ 60, ~ 40, ~ 30, ~ 10, and ~ 0, respectively.

[a]Lyα luminosity densities obtained by integrating the Lyα LF down to $\log L_{\mathrm{Ly}\alpha}$ [erg s^{-1}] = 41.41.

CHAPTER 6
EVOLUTION OF LYα LUMINOSITY DENSITY

6.1 Lyα Luminosity Density Evolution at $z \sim 0-6$

We calculate the Lyα LDs,

$$\rho_{\rm obs}^{\rm Ly\alpha} = \int_{L_{\rm lim}^{\rm Ly\alpha}}^{\infty} L_{\rm Ly\alpha} \phi_{\rm Ly\alpha}(L_{\rm Ly\alpha}) dL_{\rm Ly\alpha}, \tag{6.1}$$

at $z = 0-8$ with the Lyα LFs shown in Sections 5.1–5.2, where $L_{\rm lim}^{\rm Ly\alpha}$ is the Lyα luminosity limit for the Lyα LD estimates. We choose the common Lyα luminosity limit of $\log L_{\rm lim}^{\rm Ly\alpha}$ [erg s^{-1}] = 41.41 that corresponds to $0.03L^*_{{\rm Ly\alpha},z=3}$. Here, for the Ly$\alpha$ LD calculation, we use the Lyα LFs at $z = 5.7$ and 6.6 derived from Ouchi et al. (2008) and Ouchi et al. (2010), respectively, since the Lyα LDs of Ouchi et al. (2008, 2010) are consistent with those derived from the Subaru/HSC survey data. Note that these Lyα LFs of Ouchi et al. (2008, 2010) do not contain contamination sources, and thus are not corrected with a contamination rate.

There are two systematic uncertainties for estimates of the Lyα LDs. One uncertainty is the choice of Lyα luminosity limits. The Lyα luminosity limit can be lower than $\log L_{\rm lim}^{\rm Ly\alpha}$ [erg s^{-1}] = 41.41 to estimate representative Lyα LDs. However, we confirm that the estimated Lyα LDs are not largely different even if we integrate the Lyα LFs down to a fainter luminosity of $\log L_{\rm Ly\alpha}$ [erg s^{-1}] = 40.0. The largest Lyα LD difference of ~ 0.4 dex is found at $z = 0.3$, because the $L^*_{\rm Ly\alpha}$ value at $z = 0.3$ is significantly smaller than those at the other redshifts. Another uncertainty is Lyα EW limits for selection of LAEs. Lyα LDs are based on LAE samples selected with a Lyα EW limit (i.e., ${\rm EW}_0 \gtrsim 10-30$Å). Ouchi et al. (2008) estimate Lyα LDs for all (EW > 0Å) LAEs and find that the Lyα LDs are slightly larger than those for their EW-limited LAE samples (${\rm EW}_0 \gtrsim 10-30$Å) by ~ 0.1 dex at most. These levels of differences do not change the results of the Lyα LD evolution in this section that is at the level of an order of magnitude. For these Lyα LDs, we do not correct the Lyα flux attenuation by neutral hydrogen (HI) in the IGM. The Lyα LDs represent the amount of Lyα photons escaping not only from ISM of galaxies, but also from the HI IGM.

For comparison, we also use UV LDs taken from the literature (Bouwens et al.

2015). The UV LD is defined by

$$\rho_{\rm obs}^{\rm UV} = \int_{L_{\rm lim}^{\rm UV}}^{\infty} L_{\rm UV}\phi_{\rm UV}(L_{\rm UV})dL_{\rm UV}, \tag{6.2}$$

where $L_{\rm lim}^{\rm UV}$ is the UV luminosity limit for the UV LD estimates, and $\phi_{\rm UV}(L_{\rm UV})$ is the best-fit Schechter function for the UV LF measurements. Here, the value of $L_{\rm lim}^{\rm UV}$ is $0.03L^{*}_{{\rm UV},z=3}$ ($M_{\rm UV} = -17.0$ mag). The upper panel of Figure 6.1 presents the evolution of the Lyα LDs as a function of redshift whose data are summarized in Table 5.1. In the upper panel of Figure 6.1, we also plot the UV LDs of dust-uncorrected and -corrected UV LDs obtained by Bouwens et al. (2015). Similar to the evolutionary trends of Lyα LFs described in Section 4.1, we find the significant increase of Lyα LDs from $z \sim 2$ to 3 beyond the measurement errors. Moreover, there is an rapid increase of Lyα LDs by nearly two order of magnitudes from $z \sim 0$ to 3, and a plateau of Lyα LDs between $z \sim 3$ and 6. The decrease of Lyα LDs at $z \gtrsim 6$ is also found. For more details, see Section 4.1 and the literature (e.g. Deharveng et al. 2008; Ouchi et al. 2008; Cowie et al. 2010, 2011; Ciardullo et al. 2012; Barger et al. 2012; Wold et al. 2014).

The Lyα LD evolution is different from the UV LD evolution in the upper panel of Figure 6.1. There is an increase of UV LDs from $z \sim 0$ to 3, but the increase is only about an order of magnitude that is not as large as the one of Lyα LDs. At $z \sim 3-6$, the UV LDs show a moderate decrease and no evolutionary plateau like the one found in the Lyα LD evolution. At $z \gtrsim 6$, the decrease of Lyα LDs is faster than the one of UV LDs toward high z. We discuss the physical origins of these differences in Section 7.3.2.

6.2 Accelerated Evolution of Lyα Luminosity Function at $z \gtrsim 7$

Figure 5.4 implies that the decrease of the Lyα LF from $z = 6.6$ to 7.3 is larger than that from $z = 5.7$ to 6.6, i.e., there is an accelerated evolution of the Lyα LF at $z = 6.6 - 7.3$. To evaluate this evolution quantitatively, we calculate the Lyα LDs down to the limit of $\log L_{\rm Ly\alpha}$ [erg s^{-1}] = 41.41, as described above. Figure 6.2 presents the evolution of $\rho_{\rm obs}^{\rm Ly\alpha}$, and Table 5.1 summarizes the values of these Lyα LDs at each redshift. Here, we use $\log(1+z)$ for the abscissa in Figure 6.2, because we compare

the evolution of $\rho_{\rm obs}^{{\rm Ly}\alpha}$ with that of UV LDs, $\rho^{\rm UV}$, derived by Oesch et al. (2013) who use $\log(1+z)$ (see Section 7.4). In this figure, we find a rapid decrease of the Lyα LD at $z=6.6-7.3$. To quantify this evolution, we calculate ratios of $\rho_{z_2}^{{\rm Ly}\alpha}/\rho_{z_1}^{{\rm Ly}\alpha}$ that are shown in Table 6.1, where z_1 and z_2 are redshifts. We fit the evolution of $\rho_z^{{\rm Ly}\alpha}$ to the power-law function,

$$\rho_z^{{\rm Ly}\alpha} \propto (1+z)^k, \tag{6.3}$$

and obtain $k=-2.2\pm0.2$ at $z=5.7-6.6$ and $k=-12.9\pm12.4$ at $z=6.6-7.3$. These results suggest that the Lyα LF evolves acceleratingly at $z\gtrsim7$, although these values of k are consistent within the uncertainties.

We also investigate pure-luminosity and number density evolution cases to test whether this rapid Lyα LF evolution is dominated by a L^* or ϕ^* decrease. These evolution cases are examined by the minimum χ^2 fitting. For example, to evaluate the pure-luminosity evolution from $z=6.6$ to 7.3, we take a set of three parameters of $L^*_{z=6.6}$, $L^*_{z=7.3}/L^*_{z=6.6}$, and ϕ^*, where $L^*_{z=6.6}$ and $L^*_{z=7.3}/L^*_{z=6.6}$ are a Schechter parameter of L^* at $z=6.6$ and a ratio of $z=7.3$ L^* to $z=6.6$ L^*, respectively. Here, ϕ^* is a common value in $z=6.6$ and 7.3, and the Schechter parameter of α is fixed to -1.8. We prepare Schechter functions at $z=6.6$ and 7.3 with the sets of three parameters, and search for the best-fit parameters that minimize χ^2 by the simultaneous fit of Schechter functions to $z=6.6$ and 7.3 Lyα LFs. In this way, we obtain the best-fit parameter of $L^*_{z=7.3}/L^*_{z=6.6}$ that corresponds to a fraction of L^* for the pure-luminosity evolution between $z=6.6$ and 7.3. Similarly, we estimate $L^*_{z=7.3}/L^*_{z=5.7}$ and $L^*_{z=6.6}/L^*_{z=5.7}$ at the redshift ranges. We also evaluate the pure-number density evolution with the ratios of ϕ^* in the same manner. We summarize the best-fit parameters for these pure-luminosity and number density evolutions in Table 6.2. Figure 6.3 shows the evolutions of the L^* and ϕ^* ratios from $z=5.7$ to a redshift of z. In Figure 6.3, the shaded area denotes the L^* (and ϕ^*) evolution at $z=5.7-6.6$ with the measurement uncertainties, and indicates the extrapolation of this evolutionary trend to $z=7.3$. We find that the ratios of L^* and ϕ^* drop from $z=6.6$ to 7.3 below the shaded area. Similar to Equation (6.3), we approximate the pure L^* and ϕ^* evolutions by power laws whose indices are l and m:

$$\begin{aligned} L^*_z &\propto (1+z)^l \\ \phi^*_z &\propto (1+z)^m. \end{aligned} \tag{6.4}$$

We summarize the best-fit l and m values in Table 6.2. In either case of the pure-luminosity or number density evolution, the indices of l or m at $z = 6.6 - 7.3$ is significantly smaller than those at $z = 5.7 - 6.6$. These results are consistent with our conclusion of the accelerated evolution of the Lyα LF at $z \gtrsim 7$. The χ^2 values are comparable for the pure-luminosity and number density evolution cases (see Table 6.2), although the χ^2 values of the pure-luminosity evolution are slightly smaller than those of the pure-number density evolution. The available Lyα LF data do not have accuracies to discuss the dominant component of the evolution at $z = 5.7 - 7.3$. Nevertheless, if we assume the Lyα LF evolution is dominated by a pure L^* evolution whose χ^2 values are smaller than those of a pure ϕ^* evolution, we find that, in the pure L^* evolution, the decreases of the Lyα LF are 25% ($= [1 - L^*_{z=6.6}/L^*_{z=5.7}] \times 100$) and 70% ($= [1 - L^*_{z=7.3}/L^*_{z=5.7}] \times 100$) at $z = 5.7 - 6.6$ and $z = 5.7 - 7.3$, respectively. In other words, the typical LAE has gotten brighter by 1.3 times from $z = 6.6$ to 5.7 and 3.3 times from $z = 7.3$ to 5.7.

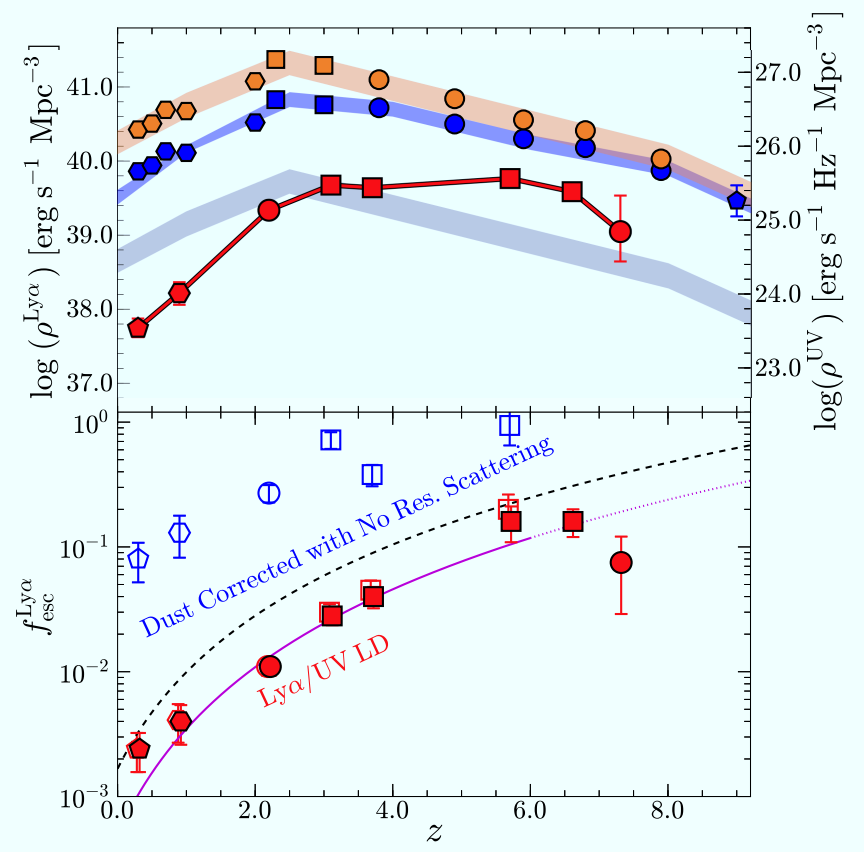

Figure 6.1 *Top*: Evolution of Lyα LDs and UV LDs as a function of redshift. The red circle at $z = 2.2$ shows the Lyα LD obtained by this study. The red pentagon at $z = 0.3$ and hexagon at $z = 0.9$ are the Lyα LDs derived by Cowie et al. (2010) and Barger et al. (2012), respectively. The red squares at $z = 3.1$, 3.7, 5.7, and 6.6 denote the results of Ouchi et al. (2008, 2010), and the red circle at $z = 7.3$ is the measurement given by this study. The blue symbols and shaded area represent the evolution of the dust-uncorrected UV LDs. The blue pentagons at $z = 0 - 2$ and squares at $z = 2 - 3$ are the UV LDs obtained by Schiminovich et al. (2005) and Reddy & Steidel (2009), respectively. The blue circles and pentagon show the UV LDs given by Bouwens et al. (2015) for $z = 3.8$, 4.9, 5.9, 6.8, and 7.9, and Ellis et al. (2013) for $z = 9.0$, respectively. The orange symbols and shaded area are the same as the blue ones, but for the dust-corrected UV LDs. The gray shaded area denotes the evolutionary tendency of the dust-corrected UV LDs scaled to the Lyα LD at $z \sim 3$ for comparison. *Bottom*: Evolution of Lyα escape fraction, $f_{\mathrm{esc}}^{\mathrm{Ly}\alpha}$, as a function of redshift. The red filled symbols show the Lyα escape fractions derived from the observed Lyα LDs and dust-corrected UV LDs (Equation 7.2). The red open symbols represent our Lyα escape fraction values corrected for an IGM absorption using the relation of Madau (1995). The blue open symbols indicate the Lyα escape fractions corrected for dust extinction in the case of no Lyα resonance scattering (Equation 7.6). The magenta solid line is the best-fit function for our Lyα escape fraction evolution from $z = 0$ to 6 ($f_{\mathrm{esc}}^{\mathrm{Ly}\alpha} = 5.0 \times 10^{-4} \times (1+z)^{2.8}$), while the black dashed line is the best-fit function derived by Hayes et al. (2011). The magenta dotted line represents the extrapolation of the magenta solid line to $z > 6$.

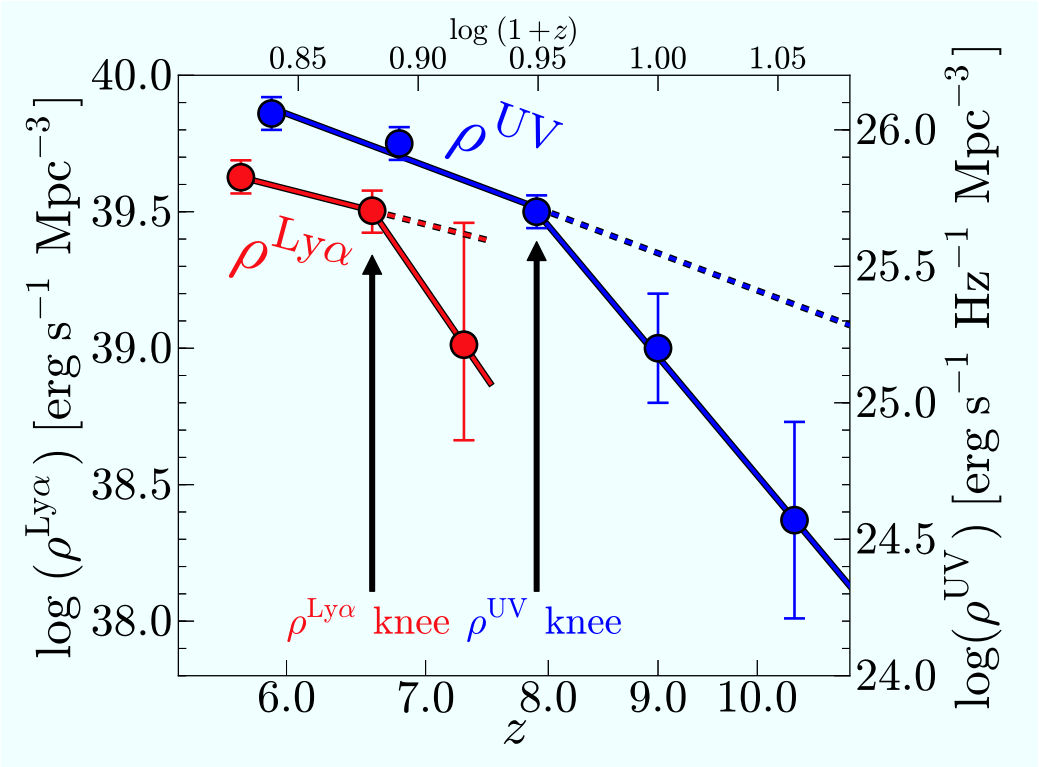

Figure 6.2 Evolution of Lyα and UV LDs at $z \gtrsim 6$. The red circles are the Lyα LDs obtained by this study, Ouchi et al. (2010), and Ouchi et al. (2008) for $z = 7.3$, 6.6, and 5.7, respectively. The blue circles are the UV LDs given by Bouwens et al. (2015) for $z = 5.9$, 6.8, 7.9, and 10.4, and Ellis et al. (2013) for $z = 9.0$. The left ordinate axis is referred for the Lyα LDs, and the right ordinate axis is for the UV LDs. The Lyα LD starts evolving acceleratingly at $z \sim 7$, while the UV LD rapidly decreases at $z \sim 8$ and beyond. The $\rho^{\mathrm{Ly}\alpha}$ and ρ^{UV} knees are indicated with the arrows.

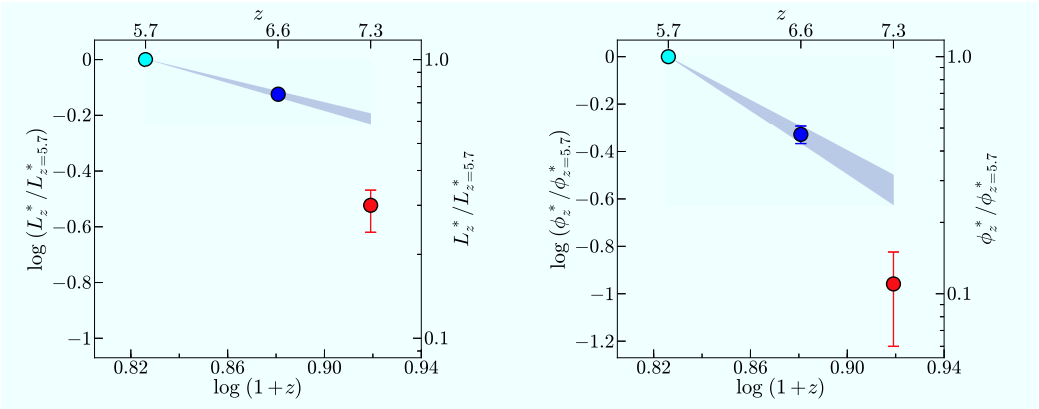

Figure 6.3 $L^*_{\mathrm{Ly}\alpha}$ and ϕ^* as a function of redshift for the cases of pure-luminosity evolution (left panel) and pure-number density evolution (right panel). For the both cases, the values of $z = 5.7$ are used for the normalization. The gray shades denote the L^* or ϕ^* evolution at $z = 5.7 - 6.6$ with the uncertainties, and these evolutionary trends are extrapolated to $z = 7.3$.

Table 6.1. Lyα Luminosity Density Evolution

Redshift Range $z = z_1 - z_2$	$\rho^{\mathrm{Ly}\alpha}$ Evolution[a] $\rho^{\mathrm{Ly}\alpha}_{z_2}/\rho^{\mathrm{Ly}\alpha}_{z_1}$	k[b]
$z = 5.7 - 6.6$	0.75 ± 0.10	-2.2 ± 0.2
$z = 6.6 - 7.3$	0.32 ± 0.07	-12.9 ± 12.4
$z = 5.7 - 7.3$	0.24 ± 0.04	-6.6 ± 5.5

[a]Best-fit values of Lyα LD ratio, $\rho^{\mathrm{Ly}\alpha}_{z_2}/\rho^{\mathrm{Ly}\alpha}_{z_1}$, where the indices of z_1 and z_2 denote redshifts.

[b]Power-law slope k defined with Equation (6.3).

Table 6.2. Best-Fit Parameters for Pure-Luminosity and Number Density Evolution Cases

Redshift Range	$L^*_{\mathrm{Ly}\alpha}$ Evolution[a]			ϕ^* Evolution[d]		
$z_1 - z_2$	$L^*_{z_2}/L^*_{z_1}$	$\chi^2(L^*)$[b]	l[c]	$\phi^*_{z_2}/\phi^*_{z_1}$	$\chi^2(\phi^*)$[e]	m[f]
$z = 5.7 - 6.6$	$0.75^{+0.02}_{-0.02}$	29.7	-2.3 ± 0.2	$0.47^{+0.04}_{-0.04}$	33.9	-6.0 ± 0.7
$z = 6.6 - 7.3$	$0.40^{+0.06}_{-0.07}$	21.9	-10.5 ± 1.6	$0.16^{+0.06}_{-0.08}$	22.1	-20.9 ± 3.6
$z = 5.7 - 7.3$	$0.30^{+0.04}_{-0.06}$	7.8	-5.6 ± 0.6	$0.11^{+0.04}_{-0.05}$	8.2	-10.3 ± 1.5

[a]Best-fit value of $L^*_{z_2}/L^*_{z_1}$, where the indices of z_1 and z_2 indicate redshifts.

[b]χ^2 for the best-fit $L^*_{z_2}/L^*_{z_1}$.

[c]Power-law slope l of Equation (6.4) for pure-luminosity evolution case.

[d]Best-fit value of $\phi^*_{z_2}/\phi^*_{z_1}$.

[e]χ^2 for the best-fit $\phi^*_{z_2}/\phi^*_{z_1}$.

[f]Power-law slope m of Equation (6.4) for pure-number density evolution case.

CHAPTER 7
DISCUSSION

7.1 Bright-end Hump of the Lyα Luminosity Function at $z = 2.2$ and 6.6

In Sections 4.4.1 − 4.4.3, we find bright-end humps in our Lyα LFs at $z = 2.2$ and 6.6, while there is no such bright-end hump in our $z = 5.7$ Lyα LF. Here, we discuss the physical origins of the bright-end humps found at $z = 2.2$ and 6.6.

In the upper panel of Figure 4.4, we find the bright-end hump of our $z = 2.2$ Lyα LF at $\log L_{\mathrm{Ly}\alpha}$ [erg s^{-1}] $\gtrsim 43.4$. The objects in the bright-end hump have UV continuum magnitudes of $M_{\mathrm{UV}} \gtrsim -25$. There are two possibilities to explain this hump at $z = 2.2$. One possibility is the existence of AGNs which have a strong Lyα emission line (e.g., Ouchi et al. 2008). Another possibility is the magnification bias (e.g., Wyithe et al. 2011; Mason et al. 2015). The gravitational lensing of foreground massive galaxies increases luminosities of LAEs at $z = 2.2$ that make the hump at the bright end LF. The lower panel of Figure 4.4 shows that all galaxies brighter than $\log L_{\mathrm{Ly}\alpha}$ [erg s^{-1}] = 43.4 have (a) bright counterpart(s) in X-ray, UV, and/or radio data, suggesting that these galaxies have AGNs. If we remove these galaxies from our sample, the shape of the Lyα LF is explained by the simple Schechter function with no hump (see the black solid line and black filled circles in the lower panel of Figure 4.4). These results indicate that the bright-end hump is almost fully explained by AGNs that have magnitudes of $M_{\mathrm{UV}} \gtrsim -25$. These AGNs are significantly fainter than QSOs, and regarded as faint AGNs. The magnification bias would exist, but it is very weak. The major physical mechanism of the bright-end hump is not the magnification bias.

In Figures 4.7, 4.8, and 5.2, we find a bright-end hump at $z = 6.6$, but no such hump found in our $z = 5.7$ Lyα LF. If this hump at $z = 6.6$ is caused by the magnification bias described above, such hump will emerge also in the Lyα LF at $z = 5.7$. Thus, the magnification bias cannot explain the bright-end hump at $z = 6.6$. There are two possibilities for the emergence of the bright-end hump at $z = 6.6$. One possibility is the existence of AGNs, which is same as the origin of the bright-end hump at $z = 2.2$. Another possibility is the formation of large ionized bubbles in the IGM around bright LAEs during the EoR. Firstly, we discuss the possibility of AGN.

Although the number densities of AGNs rapidly decrease from $z \sim 3$ toward higher redshift (e.g., Haardt & Madau 2012), some previous studies suggest the existence of (faint) AGNs at $z \gtrsim 6$ (e.g., Willott et al. 2010; Mortlock et al. 2011; Kashikawa et al. 2015; Giallongo et al. 2015; Jiang et al. 2016; Matsuoka et al. 2016; Bowler et al. 2016). Thus, AGNs may explain the bright-end hump of our $z = 6.6$ Lyα LF at $\log L_{\mathrm{Ly}\alpha}$ [erg s^{-1}] $\gtrsim 43.5$. We regard $z = 5.7$ and 6.6 LAEs brighter than $\log L_{\mathrm{Ly}\alpha}$ [erg s^{-1}] $= 43.5$ as AGNs, and calculate the number densities of these AGNs at $z = 5.7$ and 6.6. The numbers of the AGNs at $z = 5.7$ and 6.6 are 10 and 13, respectively, and these AGNs have a UV magnitude of $M_{\mathrm{UV}} \gtrsim -21$. The survey volumes for $z = 5.7$ and 6.6 LAEs are 1.16×10^7 and 1.91×10^7 Mpc^{-3}, respectively (see Section 2.2). We simply divide the numbers of the AGNs by the survey volumes, and derive the AGN number densities of 8.6×10^{-7} and 6.8×10^{-7} Mpc^{-3} at $z = 5.7$ and 6.6, respectively. Comparing our AGN number densities with QSO UV LFs at $z \sim 6$ of previous studies (e.g., Willott et al. 2010; Kashikawa et al. 2015; Jiang et al. 2016), we find that our AGN number densities at $z = 5.7$ and 6.6 are consistent with the QSO UV LFs at $z \sim 6$. This result indicates that bright LAEs ($\log L_{\mathrm{Ly}\alpha}$ [erg s^{-1}] $\gtrsim 43.5$) at $z = 5.7$ and 6.6 would be AGNs. Note that our near-infrared spectroscopic follow-up observations for the bright LAEs at $z = 5.7$ and 6.6 imply no signature of AGNs such as strong metal lines (e.g., NV and CIV) and broad emission line (see also T. Shibuya et al. in preparation). Thus, we cannot clearly conclude that bright LAEs at $z \gtrsim 6$ are AGNs.

Secondly, we discuss the possibility of large ionized bubbles. Because bright LAEs will emit a large amount of ionizing photons, the size of ionized bubbles around the bright LAEs will be very large. In that case, Lyα photons from the bright LAEs can easily escape through the IGM. On the other hand, faint LAEs will have the small size of ionized bubbles, and Lyα emission from the faint LAEs is attenuated by the Lyα damping wing of the neutral IGM. Thus, the decrease of Lyα LFs at EoR (i.e., $z \gtrsim 6$) is mainly caused at the faint end rather than at the bright end of the Lyα LFs (see also Figure 8 of Matthee et al. 2015). To quantify the size of ionized bubbles around LAEs at $z = 6.6$, we use the analytic models of Furlanetto et al. (2006). As we will describe in Section 7.4.1, we estimate the neutral hydrogen fraction at $z = 6.6$ of $x_{\mathrm{HI}} = 0.15 \pm 0.15$ from the Lyα LF evolution at $z = 5.7-6.6$. Based on the x_{HI} value and the top panel of Figure 1 of Furlanetto et al. (2006), we obtain the typical size of ionized bubbles at $z = 6.6$ of ~ 30 (comoving) Mpc. This size is comparable to that estimated

by Ouchi et al. (2009), who examine the sky distribution of dropout galaxies at $z \sim 7$. Thus, if bright LAEs at $z = 6.6$ form the ionized bubbles larger than ~ 30 (comoving) Mpc, the bright-end hump will emerge from the $z = 6.6$ Lyα LF. Note that the bright LAEs at $z = 6.6$ typically have a UV magnitude of $M_{\rm UV} \gtrsim -21$, as described above. Haiman (2002) formularizes the radius of the ionized bubble around a source at $z = 6.6$, and gives $R_{\rm S} = 0.8 \times ({\rm SFR}/10\ M_\odot\ {\rm yr}^{-1})^{1/3}(t_*/100\ {\rm Myr})^{1/3}[(1+z_*)/7.56]^{-1}$ (proper) Mpc.[1] From this equation and the UV fluxes of the bright LAEs at $z = 6.6$ (i.e., $M_{\rm UV} \gtrsim -21$), we calculate the size of the ionized bubbles of $R_{\rm S} \lesssim 7$ (comoving) Mpc.[2] This size is smaller than that estimated from the analytic model of Furlanetto et al. (2006) (~ 30 comoving Mpc). This result implies that LAEs may be clustered around bright LAEs, and form such large ionized region by overlapping each ionized bubble around an LAE.

In summary, the bright-end hump of our $z = 2.2$ Lyα LF can be explained by AGNs. At $z = 6.6$, there are two possibilities to explain the bright-end hump; the existence of AGNs and the emergence of large ionized bubbles. It is also likely that the combination of AGNs and ionized bubbles makes the bright-end hump at $z = 6.6$, but we cannot clearly conclude which possibility is correct at present.

7.2 Faint AGN UV Luminosity Function at $z \sim 2$

In Section 7.1, we discuss that the bright-end hump at $z = 2.2$ is made of faint AGNs ($\log L_{{\rm Ly}\alpha}$ [erg s^{-1}] > 43.4), most of which have the counterpart(s) in the X-ray, UV, and radio data. Using the abundance and the UV continuum magnitudes ($M_{\rm UV} \gtrsim -25$) of these faint AGNs, we derive faint AGN UV LFs. These faint AGN UV LFs complement the bright AGN UV LFs obtained by cosmological large scale surveys such as SDSS. To estimate the faint AGN UV LFs, we measure i-band magnitudes at the positions of the faint AGNs. Here, we choose the i-band magnitudes for UV continuum magnitude estimates, because we compare our results with the SDSS AGN study of Ross et al. (2013) who use i-band magnitudes to

[1] In this equation, Haiman (2002) considers an ionizing source at a given redshift (z_*) with a constant SFR and a Salpeter IMF (the $0.1 - 120 M_\odot$ mass range). Haiman (2002) assumes that the source produces ionizing photons during the lifetime (t_*).

[2] From Equation (7.4), the SFR corresponding to $M_{\rm UV} = -21$ is 13.6 $M_\odot$ yr^{-1}. We estimate the ionized bubble size under the assumption that these bright LAEs have a constant SFR of 13.6 $M_\odot$ yr^{-1}, and emit ionizing photons during their age of 100 Myr.

derive their AGN UV LF. All of our faint AGNs are detected at the $> 5\sigma$ levels in our i-band images. Note that the 5σ limiting magnitudes of our i-band images correspond to $M_{\rm UV} = -17.9$, -18.6, -20.2, -19.7, and -18.5 mag for the faint AGNs at $z = 2.2$ in the SXDS, COSMOS, CDFS, HDFN, and SSA22 fields, respectively. We calculate the volume number densities of the faint AGNs in a UV-continuum magnitude bin, dividing the number counts of faint AGNs by our comoving survey volume ($\simeq 1.32 \times 10^6$ Mpc^3). Figure 7.1 presents these UV LFs of our faint AGNs with black open circles that we call raw UV LFs. The errors of the raw UV LFs are the Poisson errors for small number statistics (Gehrels 1986).

Because AGNs do not always have Lyα emission that can be identified by our narrowband observations, the raw UV LFs are incomplete. The raw UV LFs are regarded as the lower limits of the AGN UV LFs. To evaluate the incompleteness, we use the relation of Lyα EWs and UV-continuum magnitudes (the Baldwin effect) given by Dietrich et al. (2002). Dietrich et al. (2002) obtain the median values of Lyα EWs at a given UV-continuum magnitude bin based on 744 AGNs at $z \sim 0 - 5$, where a negligibly small fraction ($\sim 10\%$) of damped Lyα systems and low quality data is removed from their AGN sample. Note that we do not take into account UV continuum indices of AGNs, because our sample is too small to make statistically useful subsamples with the additional parameter of the UV continuum indices. In Figure 7.2, we plot the median values with the black filled diamonds. Because no PDFs of Lyα EWs are presented in Dietrich et al. (2002), the errors of the black filled diamonds represent the measurement uncertainties of Lyα EWs. Figure 7.2 shows a correlation, indicating that UV-continuum faint AGNs have large Lyα EWs. The red and blue lines in Figure 7.2 represent our selection limits of $\log L_{\rm Ly\alpha}$ [erg s^{-1}] > 43.4 (for the objects in the bright-end hump) and the EW$_0$ $\gtrsim 20 - 30$Å (for our LAE sample), respectively. In Figure 7.2, we find that these selection limits (red and blue lines) are far below the median values (black diamonds) at $M_{\rm UV} \lesssim -22.5$. Thus, the faint AGN UV LFs at $M_{\rm UV} \lesssim -22.5$ can be determined with reasonable completeness corrections. Because the Lyα EW PDFs are not given in Dietrich et al. (2002), one cannot simply estimate the incompleteness. However, all of the median values at $M_{\rm UV} \lesssim -22.5$ are placed above the selection limits. The maximum correction factor is ~ 2 in the most extreme case that the Lyα EW PDF has the bottom heavy distribution. This is because about a half of the AGNs at maximum could fall below our selection limits, which can keep the median values as high as

those obtained by Dietrich et al. (2002). For our faint AGNs at $M_{\rm UV} \lesssim -22.5$, we correct the raw UV LFs for the incompleteness with the maximum correction factor, and plot the maximally-corrected UV LFs with the open squares in Figure 7.1. Because the real UV LFs should be placed between the raw UV LFs and the maximally-corrected UV LFs, we define the best-estimate UV LFs by the average of the raw and maximally-corrected UV LFs with the conservative error bars that completely cover the 1σ uncertainties of these two UV LFs. The red circles in Figure 7.1 represent the best-estimate UV LFs. In Figure 7.1 , we also present the AGN UV LFs at $z \sim 2.2$ derived with the SDSS DR9 data (the blue circles; Ross et al. 2013) and the 2dF-SDSS LRG and QSO survey data (the green circles; Croom et al. 2009). There is a magnitude-range overlap of our, Ross et al.'s, and Croom et al.'s AGN UV LF estimates at $M_{\rm UV} \simeq -24.8$. The number densities from our, Ross et al.'s, and Croom et al.'s studies agree very well within the uncertainties at the overlap magnitude, indicating that our AGN UV LF estimates are reliable. We also confirm that the AGN UV LF in our study is also consistent with that in Jiang et al. (2006).

We fit a double power-law function to the AGN UV LFs of ours, Ross et al. (2013), and Croom et al. (2009). The double power-law function for the AGN number density, $\phi_{\rm AGN}(M_{\rm UV})$, is defined by

$$\begin{aligned} &\phi_{\rm AGN}(M_{\rm UV}) \\ &= \frac{\phi^*_{\rm AGN}}{10^{0.4(\alpha_{\rm AGN}+1)(M_{\rm UV}-M^*_{\rm AGN})} + 10^{0.4(\beta_{\rm AGN}+1)(M_{\rm UV}-M^*_{\rm AGN})}}, \end{aligned} \tag{7.1}$$

where $\phi^*_{\rm AGN}$ and $M^*_{\rm AGN}$ are the characteristic number density and magnitude of AGNs, respectively. The parameters of $\alpha_{\rm AGN}$ and $\beta_{\rm AGN}$ determine the faint- and bright-end slopes of the AGN UV LFs. We obtain the best-fit parameters of $\phi^*_{\rm AGN} = 1.8 \pm 0.2 \times 10^{-6}$ Mpc^{-3}, $M^*_{\rm AGN} = -26.2 \pm 0.1$, $\alpha_{\rm AGN} = -1.2 \pm 0.1$, and $\beta_{\rm AGN} = -3.3 \pm 0.1$, and present the best-fit function with the red line in Figure 7.1. Our results suggest that the faint-end slope $\alpha_{\rm AGN}$ is moderately flat at $M_{\rm UV} \simeq -23$ - -25.

Ross et al. (2013) and Croom et al. (2009) show the faint-end slopes at $z \sim 2.2$ are $\alpha_{\rm AGN} = -1.3^{+0.7}_{-0.1}$ and -1.4 ± 0.2, respectively, that are consistent with our result. Because relatively steep faint-end slopes ($\alpha_{\rm AGN} \simeq -1.5$ - -1.8) are obtained for $z = 4-6.5$ AGNs (Ikeda et al. 2011; Giallongo et al. 2015), our moderately flat faint-end slope at $z \sim 2.2$ would suggest that the faint-end slope steepens toward high z. Figure 7.1 displays the two models of a pure luminosity evolution (PLE) model

and a luminosity evolution and density evolution (LEDE) model that are introduced by Ross et al. (2013). Comparing these two models, we find that the LEDE model explains our AGN UV LFs better than the PLE model. This comparison suggests that the AGN UV LF evolution involves both luminosities and densities.

7.3 Lyα Escape Fraction Evolution and the Physical Origins

7.3.1 Evolution of Lyα Escape Fraction at $z \sim 0-8$

In Section 6.1, we compare the evolution of the Lyα and UV LDs, and conclude that the evolutions of Lyα and UV LDs are different. To understand the physical origins of the differences between Lyα and UV LD evolutions, we investigate evolution of Lyα escape fractions, $f_{\rm esc}^{{\rm Ly}\alpha}$. The Ly$\alpha$ escape fraction evolution is investigated by previous studies (e.g., Hayes et al. 2011; Blanc et al. 2011). In this study, we revisit the Lyα escape fraction evolution, because there are significant progresses on the estimates of Lyα LDs from recent Subaru, VLT, and HETDEX pilot surveys (e.g., Cassata et al. 2011; Ciardullo et al. 2014) and UV LDs from HST UDF12, CANDELS, and HFF programs (e.g., Bouwens et al. 2015).

The cosmological volume-averaged Lyα escape fraction is defined by

$$f_{\rm esc}^{{\rm Ly}\alpha} = \rho_{\rm SFRD}^{\rm obs,Ly\alpha} / \rho_{\rm SFRD}^{\rm int,UV}, \tag{7.2}$$

where $\rho_{\rm SFRD}^{\rm obs,Ly\alpha}$ is the star formation rate densities (SFRDs) estimated from the observed Lyα LDs. The variable of $\rho_{\rm SFRD}^{\rm int,UV}$ represents SFRDs calculated from the intrinsic UV LDs that are UV LDs corrected for dust extinction. Note that the contribution from AGN luminosities to Lyα LDs and UV LDs are negligibly small due to the low AGN abundance, and that we regard these Lyα and UV photons are produced by star formation.

We use the Lyα LDs shown in Figure 6.1 (Section 6.1), and derive $\rho_{\rm SFRD}^{\rm obs,Ly\alpha}$. In the estimation of SFRs from the Lyα luminosities, we apply

$${\rm SFR}\ (M_\odot\ {\rm yr}^{-1}) = L_{{\rm Ly}\alpha}\ ({\rm erg\ s}^{-1})/(1.1 \times 10^{42}), \tag{7.3}$$

that is the combination of the Hα luminosity-SFR relation (Kennicutt 1998) and the case B approximation (Brocklehurst 1971). For $\rho_{\rm SFRD}^{\rm int,UV}$ values, we use the dust-

extinction corrected SFRDs derived by Bouwens et al. (2015). The SFRDs are estimated from the UV LDs that are integrated values of UV LFs down to $0.03L^*_{\mathrm{UV},z=3}$ (Section 6.1). The SFRs are estimated from UV luminosities with the equation (Madau et al. 1998),

$$\mathrm{SFR}\ (M_\odot\ \mathrm{yr}^{-1}) = L_{\mathrm{UV}}\ (\mathrm{erg\ s}^{-1}\ \mathrm{Hz}^{-1})/(8\times10^{27}), \tag{7.4}$$

where L_{UV} is the UV luminosity measured at 1500 Å. The dust extinction values are evaluated from the UV-continuum slope measurements with the relation of Meurer et al. (1999). The UV LDs corresponding to these SFRDs are presented in Figure 6.1. Note that a Salpeter IMF with the mass range of $0.1-100M_\odot$ is assumed in Equations (7.3) and (7.4).

From these SFRDs, we estimate Lyα escape fractions with Equation (7.2). The bottom panel of Figure 6.1 presents the Lyα escape fractions at $z\sim0-8$. We fit a power-law function of $\propto(1+z)^n$ to these Lyα escape fraction estimates at $z\sim0-6$, where n is the power law index. We obtain the best-fit function of $f_{\mathrm{esc}}^{\mathrm{Ly}\alpha}=5.0\times10^{-4}\times(1+z)^{2.8}$. The best-fit function is shown in the bottom panel of Figure 6.1. The best-fit function indicates a large increase of Lyα escape fractions from $z\sim0$ to 6 by two orders of magnitude, although the data points of $z\gtrsim6$ depart from the best-fit function. This trend is similar to the one claimed by Hayes et al. (2011). We compare the results of Hayes et al. (2011) with this study in the bottom panel of Figure 6.1. Although the general evolutionary trend is the same in Hayes et al.'s and our results, there is an offset between these two results. This offset is explained by the differences of the Lyα and UV luminosity limits for deriving the Lyα and UV LDs from Lyα and UV LFs, respectively. In fact, we obtain Lyα escape fractions consistent with those of Hayes et al. (2011), if we calculate the Lyα escape fractions with the Lyα and UV luminosity limits same as those of Hayes et al. (2011). In other words, the choice of Lyα and UV luminosity limits moderately change the Lyα escape fraction estimates, but the two-order-of-magnitude evolution of Lyα escape fractions is significantly larger than these changes. It should be noted that, if we calculate $f_{\mathrm{esc}}^{\mathrm{Ly}\alpha}$ with our Lyα LF and the Sobral et al.'s Hα LFs at $z=2.2$, we obtain $f_{\mathrm{esc}}^{\mathrm{Ly}\alpha}=0.013$ that is consistent with our original estimate with the UV LFs ($f_{\mathrm{esc}}^{\mathrm{Ly}\alpha}=0.011$). Thus, there are no significant systematics in $f_{\mathrm{esc}}^{\mathrm{Ly}\alpha}$ estimates for the choices of UV and Hα LFs. Recently, Matthee et al. (2016) obtain the $f_{\mathrm{esc}}^{\mathrm{Ly}\alpha}$ value at

$z = 2.2$ from the Lyα/Hα flux measurements of their 17 Hα emitters. They obtain a median value of $f_{\rm esc}^{{\rm Ly}\alpha} = 0.016 \pm 0.005$ that is also consistent with ours.

At $z \gtrsim 6$, there exist the departures of the Lyα escape fraction estimates from the best-fit function (the bottom panel of Figure 6.1). Moreover, the departure becomes larger toward high z. There is a decrease of Lyα escape fractions from $z \sim 6$ to 8 by a factor of ~ 2. Because the redshift range of $z \gtrsim 6$ corresponds to EoR, this decrease of Lyα escape fractions at $z \gtrsim 6$ is explained by the increase of Lyα scattering of HI in the IGM at EoR. In other words, it is likely that the physical origin of the $f_{\rm esc}^{{\rm Ly}\alpha}$ decrease at $z \gtrsim 6$ is cosmic reionization. This result is in the different form of the previous results that claim the signature of cosmic reionization based on the Lyα luminosity function decrease at $z > 6$ (e.g. Kashikawa et al. 2006; Ouchi et al. 2010; Kashikawa et al. 2011; Shibuya et al. 2012; Jiang et al. 2013) and the Lyα-emitting galaxy fraction decrease at $z > 6$ (e.g. Pentericci et al. 2011; Ono et al. 2012; Treu et al. 2013; Schenker et al. 2014).

7.3.2 Physical Origins of the Lyα Escape Fraction Evolution

Here, we discuss the physical mechanism of the large, two-order-of-magnitude increase of $f_{\rm esc}^{{\rm Ly}\alpha}$ from $z \sim 0$ to 6. Note that $f_{\rm esc}^{{\rm Ly}\alpha}$ is defined as the ratio of the Lyα LD to the UV LD of star-forming galaxies. Since these LDs are mainly contributed by continuum faint galaxies with $M_{\rm UV} \gtrsim -19$, majority of which show Lyα in emission (Stark et al. 2010), we regard LAEs as a dominant population of high-z star-forming galaxies in the following discussion.

There are four possible physical mechanisms for the large $f_{\rm esc}^{{\rm Ly}\alpha}$ increase from $z \sim 0$ to 6: evolutions of stellar population, outflow, dust extinction, and Lyα scattering of HI in the galaxy's ISM. It should be noted that the IGM absorption of Lyα becomes strong from $z \sim 0$ to 6, and that the evolution of the IGM absorption suppresses $f_{\rm esc}^{{\rm Ly}\alpha}$ (see below for the quantitative arguments), which cannot be a physical mechanism for the $f_{\rm esc}^{{\rm Ly}\alpha}$ increase toward high z. For the possibility of stellar population evolution, the estimates of the $f_{\rm esc}^{{\rm Ly}\alpha}$ would increase, if more ionizing photons for a given SFR are produced in galaxies that have very massive stars found in the early stage of star-formation. However, the average/median stellar ages of LAEs for a constant star-formation history are $10 - 300$ Myr at $z = 2 - 6$ (e.g., Gawiser et al. 2006; Pirzkal et al. 2007; Lai et al. 2008; Ono et al. 2010a,b; Guaita et al. 2011), which

are comparable with those at $z \sim 0$ (e.g., Cowie et al. 2011; Hayes et al. 2014). Because there are no systematic differences in stellar ages by redshift, the difference of stellar population does not explain the large increase of $f_{\rm esc}^{{\rm Ly}\alpha}$. For the possibility of outflow, it is likely that gas outflow of galaxies helps Lyα photons' escape from the ISM, because the Lyα resonance wavelength of the ISM is redshifted by the bulk gas motion of outflow. If there is a systematic difference in outflow velocities, the $f_{\rm esc}^{{\rm Ly}\alpha}$ values change. Because the typical outflow velocities of LAEs are $50 - 200$ km s^{-1} that show no systematic change over the redshift range of $z \sim 0 - 6$ (Hashimoto et al. 2013; Wofford et al. 2013; Erb et al. 2014; Shibuya et al. 2014; Stark et al. 2015; Rivera-Thorsen et al. 2015)[3], the galaxy outflow would not be a major reason of the large $f_{\rm esc}^{{\rm Ly}\alpha}$ increase. For the possibility of dust extinction evolution, it is thought that the amount of dust in galaxies decreases from $z \sim 0$ to 6, and that galaxies with small dust extinction have large $f_{\rm esc}^{{\rm Ly}\alpha}$ values. Because the dust attenuation of Lyα is enhanced by the resonance scattering of HI in the galaxy's ISM that depends on the HI density, we first obtain crude estimates of dust extinction effects with no resonance scattering. We estimate the luminosity averaged stellar extinction, $E(B-V)_\star$, from the dust-corrected and uncorrected UV LDs by the equation,

$$\rho_{\rm SFRD}^{\rm int,UV} = 10^{0.4 \times E(B-V)_\star \times k_{\rm UV}} \times \rho_{\rm SFRD}^{\rm uncorr,UV}, \tag{7.5}$$

where $\rho_{\rm SFRD}^{\rm uncorr,UV}$ is the dust-uncorrected UV SFRDs (Section 6.1) calculated with Equation (7.4). The value of $k_{\rm UV}$ is the extinction coefficient at 1500 Å, which is derived with the Calzetti's extinction law (Calzetti et al. 2000), $k_{\rm UV} = 10.3$. We thus obtain $E(B-V)_\star$ values over $z \sim 0 - 6$. From these $E(B-V)_\star$ values, we estimate $f_{\rm esc,dust}^{{\rm Ly}\alpha}$ with

$$f_{\rm esc,dust}^{{\rm Ly}\alpha} = 10^{-0.4 \times k_{1216} \times E(B-V)_{\rm gas}}, \tag{7.6}$$

where k_{1216} is the extinction coefficient at 1216Å, $k_{1216} = 12.0$, estimated with the Calzetti et al.'s law. Here we adopt $E(B-V)_{\rm gas} = E(B-V)_\star / 0.44$ (Calzetti et al. 2000). The blue open symbols in Figure 6.1 present the Lyα escape fraction values corrected for dust extinction, $f_{\rm esc}^{{\rm Ly}\alpha} / f_{\rm esc,dust}^{{\rm Ly}\alpha}$, in the case of no resonance scattering. The

[3]These outflow velocity measurements are obtained for UV-continuum bright galaxies, except for a few lensed galaxies. Because the outflow velocities of LAEs are similar to those of LBGs (150-200 km s^{-1}; e.g., Hashimoto et al. 2013; Erb et al. 2014; Shibuya et al. 2014), UV-continuum faint galaxies would have the outflow velocity comparable to that of UV-bright galaxies.

dust-corrected Lyα escape fractions are nearly unity at $z \sim 6$, while these fractions significantly drop from $z \sim 4$ to $z \sim 0$. At $z \sim 0$, the dust-corrected Lyα escape fraction is about an order of magnitude smaller than unity. There is a clear redshift dependence. We find that the large evolution of Lyα escape fraction can be partly explained by dust extinction with no resonance scattering, but that there still remains the large discrepancy at $z < 4$. Thus, the large $f_{\rm esc}^{\rm Ly\alpha}$ evolution requires the evolution of Lyα scattering of HI in the galaxy's ISM from $z \sim 0$ to 6 that enhances the dust attenuation. Due to the resonance nature of the Lyα line, an increase of the HI density provides longer path lengths that strengthen the effects of the ISM scattering with a small amount of dust. Indeed, several studies suggest that the high HI density of star-forming galaxies largely scatter Lyα photons (Shapley et al. 2003; Pentericci et al. 2007; Verhamme et al. 2008; Atek et al. 2009; Pardy et al. 2014).

Here, we estimate the HI column density, $N_{\rm HI}$, of ISM that needs to explain the large $f_{\rm esc}^{\rm Ly\alpha}$ increase from $z \sim 0$ to 6 with the non-resonant extinction values obtained by the observational data. We use the 3D Lyα Monte Carlo radiative transfer code, MCLya of Verhamme et al. (2006) and Schaerer et al. (2011). The MCLya code computes the Lyα radiative transfer in an expanding homogeneous shell of ISM HI and dust that surrounds a central Lyα source. The dust extinction effects are self-consistently calculated for the resonance line of Lyα. The MCLya code has four physical parameters to describe the physical properties of the shell: $N_{\rm HI}$, the nebular dust extinction $E(B-V)_{\rm gas}$, the radial expansion velocity $v_{\rm exp}$, and the Doppler parameter b that includes both thermal and turbulent gas motions within the shell. At each redshift shown in Figure 6.1, we derive the best-estimate $N_{\rm HI}$ value, using the $E(B-V)_{\rm gas}$ values obtained above. We set $b = 12.8$ km s^{-1} that is a fiducial value, although the b parameter negligibly changes our results. For $v_{\rm exp}$, we adopt the average outflow velocity of galaxies at $z \sim 0-6$, $v_{\rm exp} = 150$ km s^{-1} (Jones et al. 2012; Hashimoto et al. 2013; Shibuya et al. 2014; Stark et al. 2015; Rivera-Thorsen et al. 2015). Because the outflow velocity measurements, available to date, have large uncertainties, we allow the moderately large range of outflow velocities, $v_{\rm exp} = 50-200$ km s^{-1}, that includes most of outflow velocity measurements for the low-z and high-z LAEs and LBGs so far obtained (Jones et al. 2012; Hashimoto et al. 2013; Shibuya et al. 2014; Stark et al. 2015; Rivera-Thorsen et al. 2015).

We obtain the best-estimate $N_{\rm HI}$ values with the three fixed parameters for the MCLya code, calculating the Lyα escape fractions that agrees with those of the

observational estimates. For the observational estimates of the Lyα escape fractions, we use the Lyα escape fraction that is corrected for the IGM absorption, $f_{\rm esc}^{{\rm Ly}\alpha}/f_{\rm esc,IGM}^{{\rm Ly}\alpha}$ (red open symbols in the bottom panel of Figure 6.1), where $f_{\rm esc,IGM}^{{\rm Ly}\alpha}$ is the Lyα escape fraction contributed only by the IGM HI Lyα absorption. We estimate $f_{\rm esc,IGM}^{{\rm Ly}\alpha}$ with the formalism of Madau (1995)[4], assuming no effects of Lyα damping wing absorption that is negligible in the redshift range of $z = 0 - 6$ after the cosmic reionization. In Figure 7.3, we show the best-estimate $N_{\rm HI}$ values for the average outflow velocity of $v_{\rm exp} = 150$ km s^{-1}. We fit a function of $N_{\rm HI} = n^*(z^*/\exp(z))^p \exp(-\exp(z)/z^*)/z^*$ to these $N_{\rm HI}$ estimates at $z = 0 - 6$, where p, n^*, and z^* are free parameters. We obtain the best-fit parameters of $n^* = 1.25 \times 10^{21}$ cm^{-2}, $p = 0.52$, and $z^* = 329$. In Figure 7.3, the black solid curve represents the best-fit function, and the gray shaded area exhibits the $N_{\rm HI}$ range of the best-fit function that is allowed in the outflow velocity range of $v_{\rm exp} = 50 - 200$ km s^{-1}. Figure 7.3 indicates that $N_{\rm HI}$ decreases from $z \sim 0$ to 6, and the best-estimate $N_{\rm HI}$ values at $z \sim 0$, 2, and 6 are $\sim 7 \times 10^{19}$, $\sim 3 \times 10^{19}$, and $\sim 1 \times 10^{18}$ cm^{-2}, respectively. Our $N_{\rm HI}$ estimates agree with the one obtained by the independent approach of Pardy et al. (2014), which is presented in Figure 7.3. Pardy et al. (2014) measure $N_{\rm HI}$ of star-forming galaxies at $z \sim 0.1$ with the HI imaging and spectroscopic data of the 100m Green Bank Telescope. Hashimoto et al. (2015) also estimate $N_{\rm HI}$ with Lyα line profiles of galaxies at $z \sim 2$ based on the high resolution spectra, and these $N_{\rm HI}$ estimates are similar to those of our study. The agreements between our results and these studies suggest that our $N_{\rm HI}$ estimates are reasonably reliable. In Figure 7.3, we find that the $N_{\rm HI}$ decrease with dust extinction of Lyα resonant scattering can explain the large $f_{\rm esc}^{{\rm Ly}\alpha}$ increase at $z \sim 0 - 6$, even if we allow the uncertainty of the outflow velocity measurements. The picture of the $N_{\rm HI}$ decrease is consistent with the increase of the ionization parameter toward high z suggested by Nakajima & Ouchi (2014). Because high-z galaxies with a high ionization parameter may have density-bounded nebulae (see Figure 12 of Nakajima & Ouchi 2014), a large fraction of HI in ISM is ionized, which shows a small $N_{\rm HI}$. The $N_{\rm HI}$ decrease is also consistent with the picture that the ionizing photon escape fraction increases toward high z (e.g., Inoue et al. 2006; Ouchi et al. 2009; Dijkstra et al. 2014; Nakajima & Ouchi 2014). Our results suggest that the large $f_{\rm esc}^{{\rm Ly}\alpha}$ increase is self-consistently explained by the decreasing $N_{\rm HI}$, which weakens the ISM dust attenuation through the Lyα resonance scattering. If we assume the expanding shell models, the typical

[4]We extrapolate the Madau (1995) formalism at $z \sim 2 - 4$ to $z \sim 6$ (cf. Inoue et al. 2014).

$N_{\rm HI}$ decreases from $\sim 7 \times 10^{19}$ ($z \sim 0$) to $\sim 1 \times 10^{18}$ cm^{-2} ($z \sim 6$).

7.4 Implications from the Accelerated Evolution of Lyα Luminosity Function at $z > 7$

In Section 6.2, we find that the Lyα LF shows the accelerated evolution at a redshift beyond $z \sim 7$. We refer to the redshift starting the rapid decrease of the Lyα LDs as "$\rho^{\rm Ly\alpha}$ knee" that is indicated in Figure 6.2. In contrast with this evolution of the Lyα LF, there is no such a rapid decrease in the UV LF at $z \sim 7$, but only at $z > 8$, if any (Oesch et al. 2013; Bouwens et al. 2015). Figure 6.2 compares the evolution of $\rho^{\rm Ly\alpha}$ (red symbols) and $\rho^{\rm UV}$ (blue symbols). Although the rapid decrease of the UV LF at $z > 8$ is still an open question (see, e.g., Ellis et al. 2013; Robertson et al. 2013), we refer to the redshift starting this possible rapid decrease of the UV LF as "$\rho^{\rm UV}$ knee". Again, there is a significant redshift difference between $\rho^{\rm Ly\alpha}$ and $\rho^{\rm UV}$ knees (Figure 6.2). Because the evolution of $\rho^{\rm UV}$ correlates with the cosmic SFR history, the accelerated evolution of the Lyα LF found at $z \sim 7$ is not originated from a rapid decrease of the SFRD. To explain this accelerated evolution of the Lyα LF, there should exist physical mechanisms related to the Lyα production and escape processes. The simple interpretation of the Lyα LF decrease is that the Lyα damping wing of the IGM given by cosmic reionization absorbs Lyα of galaxies strongly toward high redshifts. To investigate this simple scenario of cosmic reionization, we first estimate the neutral hydrogen fraction, $x_{\rm HI}$, at $z = 6.6$ and 7.3 in Section 7.4.1. We estimate $x_{\rm HI}$ value at $z = 6.6$ from our Lyα LFs at $z = 5.7$ and 6.6, which are derived with the Subaru/HSC data. We compare our $x_{\rm HI}$ estimates with Thomson scattering optical depth obtained by *WMAP* and *Planck* in Section 7.4.2.

7.4.1 Constraints on $x_{\rm HI}$ at $z = 6.6$ and 7.3

In Sections 7.4.1-7.4.2, we discuss the simple scenario of cosmic reionization that contributes to the accelerated evolution of the Lyα LF at $z \gtrsim 7$. We define $T^{\rm IGM}_{{\rm Ly}\alpha,z}$ as a Lyα transmission through the IGM at a redshift of z, and first calculate $T^{\rm IGM}_{{\rm Ly}\alpha,z=7.3}/T^{\rm IGM}_{{\rm Ly}\alpha,z=5.7}$ to estimate $x_{\rm HI}$ at $z = 7.3$. Because cosmic reionization has been completed at $z = 5.7$ (Fan et al. 2006), the Lyα damping wing absorption of the IGM is negligible at $z = 5.7$.

Section 6.2 presents the estimates of the Lyα LDs from the Lyα LFs of this study

at $z = 5.7$ and 7.3 (Table 5.1). With the values shown in Table 5.1, we obtain $\rho^{\mathrm{Ly}\alpha,\mathrm{tot}}_{z=7.3}/\rho^{\mathrm{Ly}\alpha,\mathrm{tot}}_{z=5.7} = 0.24$.

Because the Lyα LF evolution is made not only by cosmic reionization, but also by the SFR change of galaxy evolution, we subtract the effect of the SFRD evolution from the Lyα LD evolution. An SFR of galaxy is correlated with the UV luminosity. The UV luminosity of $z = 7.3$ LAE in principle can be estimated by the subtraction of the Lyα line flux from the z'-band flux. However, we cannot derive the reliable UV luminosities from our data. This is because there exist the large uncertainties of the z'-band magnitude and the contamination of unknown amount of the IGM absorption that make a significant bias in the estimate of the UV continuum as demonstrated in the simulations of Shimasaku et al. (2006). To derive a reliable UV LF of $z \gtrsim 6$ LAEs, one needs deep near-infrared data, such as J and H images, which cover the continuum emission longward of the Lyα line for most of LAEs, but no such data are available for LAE studies, to date. Since we cannot derive a reliable UV LF of $z = 7.3$ LAE from our data, we quantify ρ^{UV} at $z = 5.7 - 7.3$ given by the other observations. We use ρ^{UV} measured with the samples of dropout galaxies (Bouwens et al. 2009, 2011), and estimate ρ^{UV} at $z = 5.7$ and 7.3 by the interpolation of this evolution. We, thus, obtain $\rho^{\mathrm{UV}}_{z=7.3}/\rho^{\mathrm{UV}}_{z=5.7} = 0.70$.

Following the procedure of Ouchi et al. (2010), we estimate $T^{\mathrm{IGM}}_{\mathrm{Ly}\alpha,z=7.3}/T^{\mathrm{IGM}}_{\mathrm{Ly}\alpha,z=5.7}$ and x_{HI}. The value of $\rho^{\mathrm{Ly}\alpha}$ is given by

$$\rho^{\mathrm{Ly}\alpha} = \kappa \; T^{\mathrm{IGM}}_{\mathrm{Ly}\alpha} \; f^{\mathrm{esc}}_{\mathrm{Ly}\alpha} \; \rho^{\mathrm{UV}}, \tag{7.7}$$

where κ is a factor converting from UV to Lyα luminosities, which depends on stellar population. $f^{\mathrm{esc}}_{\mathrm{Ly}\alpha}$ is a fraction of Lyα emission escape from a galaxy through the ISM absorption including galactic neutral hydrogen and dust attenuation. With Equation (7.7), $T^{\mathrm{IGM}}_{\mathrm{Ly}\alpha,z=7.3}/T^{\mathrm{IGM}}_{\mathrm{Ly}\alpha,z=5.7}$ is written as

$$\frac{T^{\mathrm{IGM}}_{\mathrm{Ly}\alpha,z=7.3}}{T^{\mathrm{IGM}}_{\mathrm{Ly}\alpha,z=5.7}} = \frac{\kappa_{z=5.7}}{\kappa_{z=7.3}} \frac{f^{\mathrm{esc}}_{\mathrm{Ly}\alpha,z=5.7}}{f^{\mathrm{esc}}_{\mathrm{Ly}\alpha,z=7.3}} \frac{\rho^{\mathrm{Ly}\alpha}_{z=7.3}/\rho^{\mathrm{Ly}\alpha}_{z=5.7}}{\rho^{\mathrm{UV}}_{z=7.3}/\rho^{\mathrm{UV}}_{z=5.7}}. \tag{7.8}$$

Assuming that the stellar population of LAEs is the same at $z = 5.7$ and 7.3 (i.e., $\kappa_{z=5.7}/\kappa_{z=7.3} = 1$), and the physical state of ISM is not evolved at $z = 5.7 - 7.3$ (i.e.,

$f^{\rm esc}_{{\rm Ly}\alpha,z=5.7}/f^{\rm esc}_{{\rm Ly}\alpha,z=7.3}=1$), we obtain

$$\frac{T^{\rm IGM}_{{\rm Ly}\alpha,z=7.3}}{T^{\rm IGM}_{{\rm Ly}\alpha,z=5.7}}=\frac{\rho^{{\rm Ly}\alpha}_{z=7.3}/\rho^{{\rm Ly}\alpha}_{z=5.7}}{\rho^{\rm UV}_{z=7.3}/\rho^{\rm UV}_{z=5.7}}. \tag{7.9}$$

From the ratios of the Lyα and UV luminosity densities described above, we estimate $T^{\rm IGM}_{{\rm Ly}\alpha,z=7.3}/T^{\rm IGM}_{{\rm Ly}\alpha,z=5.7}$ to be 0.34.

We use theoretical models to constrain $x_{\rm HI}$ at $z=7.3$ with our estimates of $T^{\rm IGM}_{{\rm Ly}\alpha,z=7.3}/T^{\rm IGM}_{{\rm Ly}\alpha,z=5.7}=0.34$. In the analytic model of Santos (2004), the Lyα transmission fraction of the IGM is related to $x_{\rm HI}$ in two cases of no galactic wind and a galactic outflow that give shifts of Lyα line from a systemic velocity by 0 and 360 km/s, respectively. The value of $T^{\rm IGM}_{{\rm Ly}\alpha,z=7.3}/T^{\rm IGM}_{{\rm Ly}\alpha,z=5.7}=0.34$ corresponds to $x_{\rm HI}$ ~ 0.0 and ~ 0.7 in the former and the latter case, respectively. Because recent studies have reported that the Lyα line emission of LAE at $z=2.2$ is redshifted by ~ 200 km/s (Hashimoto et al. 2013; Shibuya et al. 2014), we take $x_{\rm HI}\sim 0.5$ that is the $x_{\rm HI}$ value interpolated by the Lyα velocity shift in Figure 25 of Santos (2004). McQuinn et al. (2007) predict Lyα LFs for various $x_{\rm HI}$ values with radiative transfer simulations. By the comparison of our Lyα LF with these simulation results in Figure 4 of McQuinn et al. (2007), we obtain $x_{\rm HI}\sim 0.7$. In the models of Dijkstra et al. (2007a,b), the Lyα transmission fraction of the IGM is related to the size of typical ionized bubbles, and Furlanetto et al. (2006) predict $x_{\rm HI}$ from the size of the ionized bubble with the analytic model. Based on Figure 6 of Dijkstra et al. (2007b), our estimates of the Lyα transmission fraction of the IGM at $z=5.7-7.3$ suggest that the typical size of the ionized bubble is very small, ~ 3 comoving Mpc, and the estimated neutral hydrogen fraction is ~ 0.6 from the top panel of Figure 1 of Furlanetto et al. (2006). Based on these results of $x_{\rm HI}$, we conclude the neutral hydrogen fraction is relatively high, $x_{\rm HI}=0.3-0.8$ at $z=7.3$ that includes the uncertainties of the various model predictions and the Lyα transmission fraction estimated from the observations.

Similarly, we obtain $\rho^{{\rm Ly}\alpha,{\rm tot}}_{z=6.6}/\rho^{{\rm Ly}\alpha,{\rm tot}}_{z=5.7}=0.75$ based on our $z=5.7$ and 6.6 Lyα LFs in Sections 4.4.2 and 4.4.3, and $\rho^{\rm UV}_{z=6.6}/\rho^{\rm UV}_{z=5.7}=0.74$ from the UV LF measurements of Bouwens et al. (2015). Under the assumption of $\kappa_{z=5.7}/\kappa_{z=6.6}=1$ and $f^{\rm esc}_{{\rm Ly}\alpha,z=5.7}/f^{\rm esc}_{{\rm Ly}\alpha,z=6.6}=1$, we calculate $T^{\rm IGM}_{{\rm Ly}\alpha,z=6.6}/T^{\rm IGM}_{{\rm Ly}\alpha,z=5.7}=1.0$ from Equation (7.9). Using the ratio of the IGM transmission at $z=6.6$ to at $z=5.7$ and simple theoretical models described above, we estimate $x_{\rm HI}=0.0-0.3$ at $z=6.6$, which includes the

uncertainties of both the LD calculations and the various model predictions.

In Figure 7.4, we plot our estimates of $x_{\rm HI}$ at $z = 6.6$ and 7.3, and compare them with those from the previous studies. The measurements of the Lyα LF imply $x_{\rm HI} < 0.63$ at $z = 7.0$ (Ota et al. 2010), and this result is consistent with our estimates of $x_{\rm HI} = 0.0 - 0.3$ at $z = 6.6$ and $x_{\rm HI} = 0.3 - 0.8$ at $z = 7.3$. The studies of Lyα emitting fraction by Pentericci et al. (2011), Schenker et al. (2012), Ono et al. (2012), Treu et al. (2012), Caruana et al. (2012, 2014), Pentericci et al. (2014), and Schenker et al. (2014) indicate $x_{\rm HI} \gtrsim 0.5$ at $z \sim 7$, and these estimates are also comparable with ours within the uncertainties. Moreover, the Lyα damping wing absorption of QSO continuum suggests $x_{\rm HI} \gtrsim 0.1$ at $z = 7.1$ (Mortlock et al. 2011; Bolton et al. 2011) that is, again, consistent with our estimates.

In Section 5.2, we find that the decrease of the Lyα LF at $z = 6.6 - 7.3$ is larger than that at $z = 5.7 - 6.6$. This accelerated evolution could be also found in Figure 7.4, albeit with the large uncertainties, by the comparison of our $z = 6.6$ and 7.3 results (red filled circles). While we find that the Lyα LF decreases from $z = 6.6$ to 7.3 at the $> 90\%$ confidence level, the difference of the $x_{\rm HI}$ estimates between $z = 6.6$ and 7.3 is only within the 1σ level that is less significant than the Lyα LF evolution result. This is because the error bar of $x_{\rm HI}$ at $z = 7.3$ is not only from the uncertainties of the Lyα LF estimates, but also from the errors of the UV LF measurements and the variance of the theoretical model results.

It is implied that the amount of the IGM neutral hydrogen may increase acceleratingly at $z \sim 7$. However, the results of the $x_{\rm HI}$ evolution are based on various assumptions that should be examined carefully. In this section, for example, we assume $f^{\rm esc}_{{\rm Ly}\alpha,z=5.7}/f^{\rm esc}_{{\rm Ly}\alpha,z=7.3} = 1$. In Section 7.3.1, we show that the Lyα escape fraction of LAEs increases from $z \sim 0$ to ~ 6, i.e., $f^{\rm esc}_{{\rm Ly}\alpha,z=0}/f^{\rm esc}_{{\rm Ly}\alpha,z=6} < 1$ (see also Ouchi et al. 2008; Ono et al. 2010a; Hayes et al. 2011). If this trend continues to $z = 7.3$, the intrinsic Lyα escape fraction with no IGM absorption would be $f^{\rm esc}_{{\rm Ly}\alpha,z=5.7}/f^{\rm esc}_{{\rm Ly}\alpha,z=7.3} < 1$. In this case, we obtain the value of $T^{\rm IGM}_{{\rm Ly}\alpha,z=7.3}/T^{\rm IGM}_{{\rm Ly}\alpha,z=5.7}$ is smaller than our estimate above (see Equation 7.8) and an $x_{\rm HI}$ estimate higher than our result of $x_{\rm HI} = 0.3 - 0.8$ at $z = 7.3$.

7.4.2 Comparison with Thomson Scattering Optical Depth Measurements

In this section, we investigate whether the cosmic reionization history derived by our $x_{\rm HI}$ estimates at $z = 6.6$ and 7.3 can explain the Thomson scattering optical depth, $\tau_{\rm el}$, measurements given by *WMAP* and *Planck*. Because one needs to know $x_{\rm HI}$ evolution at $z = 0 - 1100$ to derive $\tau_{\rm el}$, we use three models of the $x_{\rm HI}$ evolution (Choudhury et al. 2008) that cover typical scenarios of the early and relatively-late cosmic reionization history. We refer to these three $x_{\rm HI}$ evolution models as models A, B, and C corresponding to the minimum halo masses for reionization sources that are $\sim 10^9$, $\sim 10^8$, and $\sim 5 \times 10^5$ $M_\odot$, respectively, at $z = 6$ in the semi-analytic models of Choudhury et al. (2008). We present the $x_{\rm HI}$ evolution of models A, B, and C in Figure 7.4, and $\tau_{\rm el}$ as a function of redshift for these models in Figure 7.5. In Figure 7.5, the hatched and gray regions represent the 1σ range of $\tau_{\rm el}$ measured by *WMAP* and *Planck*, respectively, and the optical depth measured by *Planck* is significantly lower than the one of the *WMAP* measurement.

We first compare our $x_{\rm HI}$ evolution with the $\tau_{\rm el}$ given by *WMAP*, and discuss the physical mechanisms of the accelerated evolution of the Lyα LF at $z \gtrsim 7$. While the model B is consistent with our $x_{\rm HI}$ estimate not only at $z = 6.6$ but also at $z = 7.3$ in Figure 7.4, the model B falls far below the $\tau_{\rm el}$ measurements of *WMAP* in Figure 7.5. These results require reionization that proceeds at an epoch earlier than the model B in the case that we apply the $\tau_{\rm el}$ value measured by *WMAP*. The model C is such an early reionization model that just agrees with the lower end of the error of our $x_{\rm HI}$ estimate at $z = 7.3$ in Figure 7.4. However, the model C is barely consistent with the *WMAP* result within the 1σ error in Figure 7.5. Thus, there is a possible tension between our estimate of high $x_{\rm HI}$ at $z = 7.3$ and the CMB measurements of high $\tau_{\rm el}$ derived by the nine-year *WMAP* data. A similar tension between $\tau_{\rm el}$ and galaxy observation results is also claimed by Robertson et al. (2010) who discuss UV luminosities of reionization sources that are based on observational quantities independent from the Lyα LFs of our study. The physical origin of the accelerated Lyα LF evolution at $z \gtrsim 7$ could be something other than the rapid increase of the neutral hydrogen at $z \gtrsim 7$, because the $\tau_{\rm el}$ measurement obtained by *WMAP* has a tension with the high $x_{\rm HI}$ value at $z = 7.3$ that is estimated with our Lyα LFs under the assumption that the Lyα LF evolution is given by the combination of cosmic

reionization and cosmic SFRD evolution. Similarly, large values of $x_{\rm HI}$ estimates at $z \simeq 6-7$ are obtained from the Lyα damping wing absorption techniques with LAEs (Kashikawa et al. 2006, 2011; Ota et al. 2008, 2010; Ouchi et al. 2010; Shibuya et al. 2012), LBGs (Pentericci et al. 2011; Schenker et al. 2012; Ono et al. 2012; Treu et al. 2012; Caruana et al. 2012, 2014; Pentericci et al. 2014; Schenker et al. 2014), QSOs (Bolton et al. 2011), and GRBs (Totani et al. 2014). Recent theoretical studies suggest a few physical pictures that explain the $\tau_{\rm el}$ measurements by *WMAP* and the large $x_{\rm HI}$ estimates given by the Lyα damping wing absorption measurements. The first picture is the presence of clumpy neutral hydrogen clouds in ionized bubbles at the end of reionization epoch. Lyα line and UV continuum from objects would be attenuated by a number of optically thick absorption systems that have large HI column densities such as Lyman limit systems (Bolton & Haehnelt 2013; Xu et al. 2014; Kakiichi et al. 2016). The absorption systems of the clumpy HI clouds do not contribute to the volume-limited value of $x_{\rm HI}$ significantly, but to the attenuation of Lyα-line and UV-continuum emitted from objects. Interestingly, recent ALMA observations report a possible HI cloud emitting [CII]158μm near a star-forming galaxy at $z = 6.6$ (Ono et al. 2014), supporting this physical picture. If this picture is correct, our finding of the accelerated Lyα LF evolution indicates that the number of such clumpy HI clouds rapidly increases at $z \gtrsim 7$. The second picture is the increase of ionizing photon escape fraction toward high z (Dijkstra et al. 2014). Lyα photons are produced by recombination following photoionization in ionized gas of a galaxy. The more the ionizing photons escape from the galaxy, the smaller an amount of recombination is. Under the significant escape of the ionizing photons, Lyα emission is not efficiently produced by ionized clouds in a galaxy. This picture reconciles with the increase of the ionizing photon escape fraction suggested by Nakajima & Ouchi (2014) from the ionization parameter evolution. If this picture is correct, the accelerated Lyα LF evolution would suggest either the sudden decrease of the gas covering fraction of galaxies or the boosting of the ionization parameter that would make density-bounded clouds in galaxies. However, in this picture, the high $x_{\rm HI}$ values given by the UV-continuum studies of QSOs and GRBs are not explained. Additional physical mechanisms would be required for these $x_{\rm HI}$ results of the UV-continuum studies.

Although we have discussed some physical mechanisms to explain the tension between our rapid $x_{\rm HI}$ evolution and the high $\tau_{\rm el}$ measurement obtained by *WMAP*, the latest results from the *Planck* observations show that the Thomson scattering

optical depth measured by *Planck* becomes $\tau_{\rm el} = 0.058 \pm 0.009$ (Planck Collaboration et al. 2016) significantly lower than that obtained by *WMAP*. From Figure 7.4, the model B is consistent with our $x_{\rm HI}$ estimates at both $z = 6.6$ and 7.3, and also explain the Thomson scattering optical depth obtained by the latest *Planck* 2016 data in Figure 7.5. Although the model A can explain the $\tau_{\rm el}$ value, this model is inconsistent with our $x_{\rm HI}$ estimate at $z = 6.6$. The model C can barely explain our $x_{\rm HI}$ values at $z = 6.6$ and 7.3, but is placed above the $\tau_{\rm el}$ of *Planck* beyond the 1σ error (Figure 7.5). Thus, these results show that the cosmic reionization history such as the model B can explain both our $x_{\rm HI}$ estimates and the $\tau_{\rm el}$ value from the latest *Planck* data. In this case, the accelerated Lyα LF evolution indicates the rapid increase of the neutral hydrogen in the IGM at $z \gtrsim 7$, albeit with the large uncertainty of the $x_{\rm HI}$ estimate at $z = 7.3$.

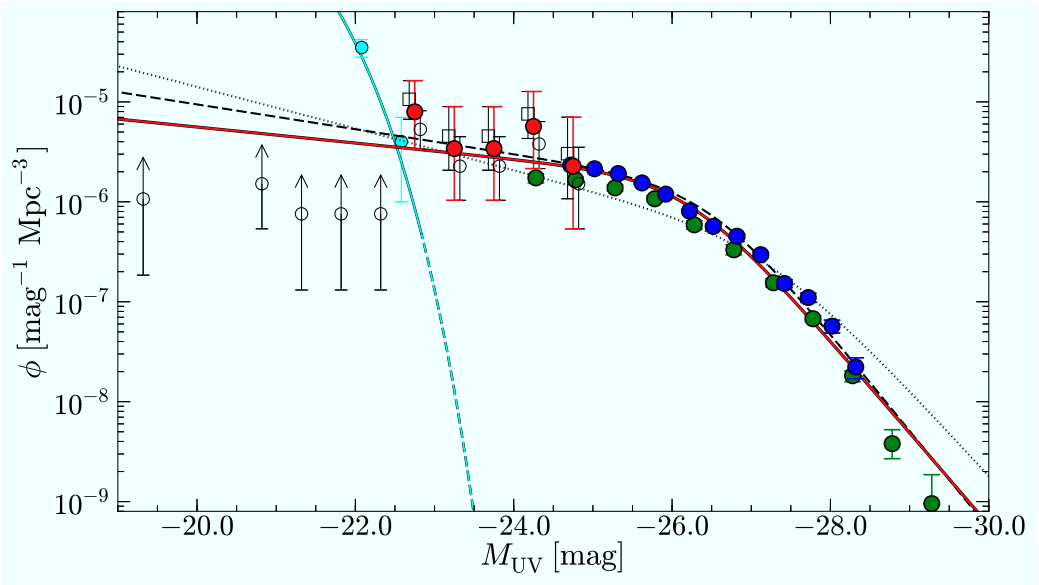

Figure 7.1 UV LF of faint AGNs. The red filled circles denote the best-estimate AGN UV LFs and the black open circles and squares represent the raw and maximally-corrected AGN UV LFs, respectively (see the text for details). At $M_{\rm UV} \gtrsim -22.5$, we plot only the raw UV LF as lower limits with black arrows, because one cannot estimate the incompleteness at this range (see the text for details). For display purposes, we slightly shift the black symbols along the abscissa. The blue and green circles are the AGN UV LFs at $z \sim 2.2$ derived from the SDSS DR9 dataset (Ross et al. 2013) and the 2dF-SDSS LRG and QSO survey dataset (Croom et al. 2009), respectively. The red curve shows the best-fit function for the AGN UV LFs of ours, Ross et al. (2013), and Croom et al. (2009). The black dotted and dashed curves represent the best-fit functions under the assumptions of the PLE and LEDE models introduced by Ross et al. (2013), respectively. We also display the UV LF of $z = 2$ LBGs obtained by Reddy & Steidel (2009) with the cyan circles. The cyan solid curve represents the best-fit Schechter function of the LBG UV LF within a range of the observed UV-continuum magnitude (i.e., $M_{\rm UV} > -22.8$), while the cyan dashed curve denotes the function extrapolated to $M_{\rm UV} < -22.8$.

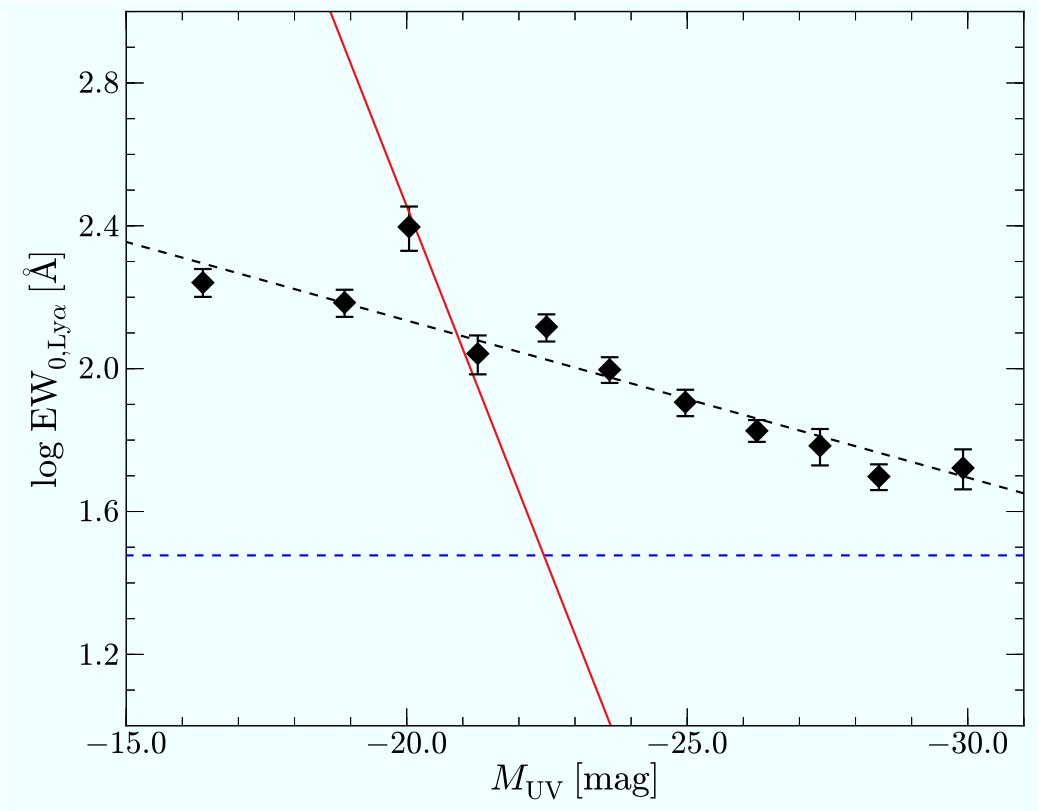

Figure 7.2 Lyα EW$_0$ as a function of UV-continuum magnitude of AGN. The black diamonds represent the median values of the observed Lyα EW$_0$ at a given UV-continuum magnitude, and the black dashed line is a best-fit linear function obtained by Dietrich et al. (2002). The error bars of the black diamonds indicate the measurement uncertainties of the Lyα EWs. The red solid line shows a locus of the luminosity for $\log L_{\mathrm{Ly}\alpha}$ [erg s^{-1}] = 43.4, which is a selection criterion for our faint AGNs. The blue dashed line denotes the EW$_0$ threshold for selection of our $z = 2.2$ LAEs (i.e., $\sim 20 - 30$Å).

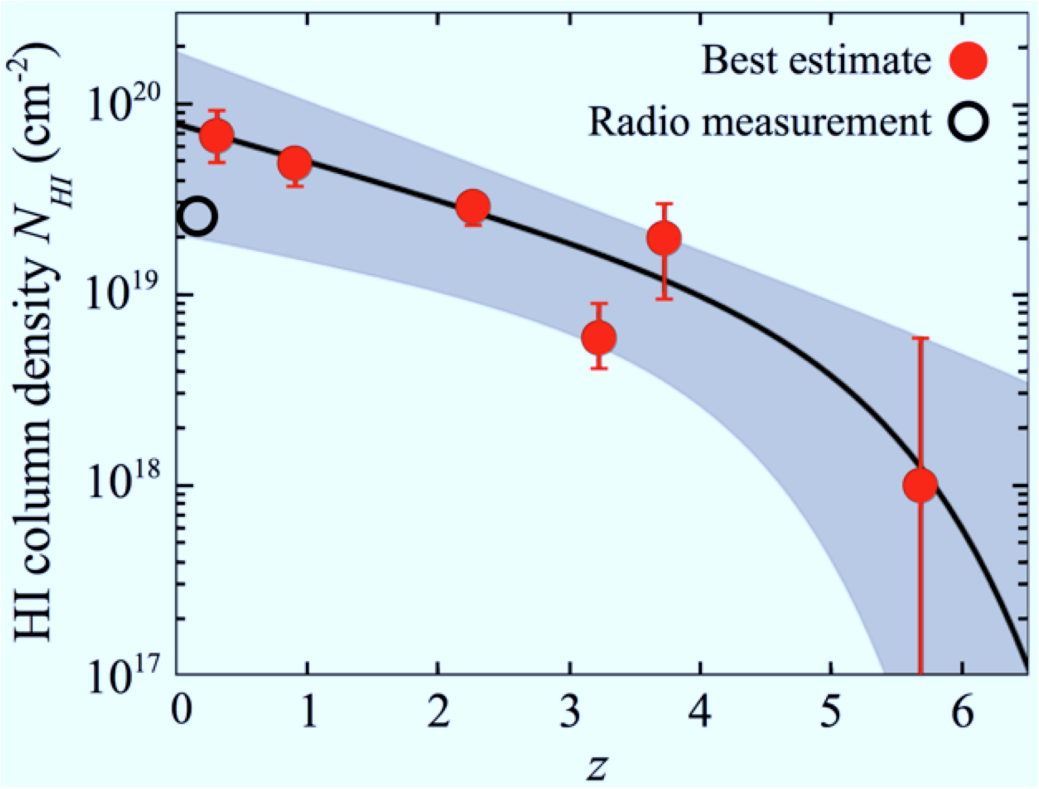

Figure 7.3 Evolution of the HI column density, $N_{\rm HI}$, of LAEs, as derived from the 3D Lyα Monte Carlo radiative transfer code, MCLya. The red filled circles show the best-estimate $N_{\rm HI}$ values for the average outflow velocity of $v_{\rm exp} = 150$ km s^{-1} (see the text). The black solid curve is the best-fit function for these $N_{\rm HI}$ values. The gray shaded area represents the $N_{\rm HI}$ range of the best-fit function allowed for the outflow velocity range of $v_{\rm exp} = 50 - 200$ km s^{-1}. The black open circle denotes the mean $N_{\rm HI}$ value at $z \sim 0.1$ from the radio observations (Pardy et al. 2014).

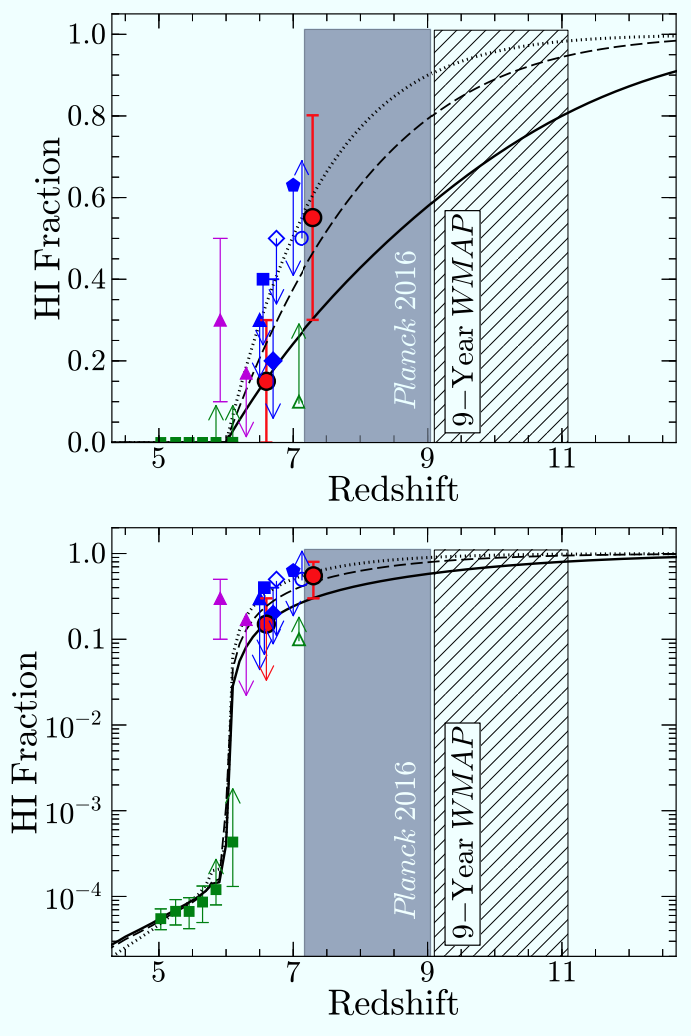

Figure 7.4 Evolution of neutral hydrogen fraction of the IGM. Top and bottom panels are the same plots, but with the ordinate axes of linear and logarithmic scales, respectively. The red filled circles are the $x_{\rm HI}$ estimates from our Lyα LFs at $z = 6.6$ and 7.3. The blue filled triangle, square, diamond, and pentagon denote the $x_{\rm HI}$ values from the Lyα LF evolution presented in Malhotra & Rhoads (2004), Kashikawa et al. (2011), Ouchi et al. (2010), and Ota et al. (2010), respectively. The blue open diamond and circle indicate the $x_{\rm HI}$ constraints given by the clustering of LAEs (Ouchi et al. 2010) and the Lyα emitting galaxy fraction (Pentericci et al. 2011; Schenker et al. 2012; Ono et al. 2012; Treu et al. 2012; Caruana et al. 2012, 2014; Pentericci et al. 2014; Schenker et al. 2014), respectively. The magenta filled triangles show the $x_{\rm HI}$ measurements from the optical afterglows of GRBs (Totani et al. 2006, 2014). The green filled squares and open triangle are the $x_{\rm HI}$ constraints provided from the GP test of QSOs (Fan et al. 2006) and the size of QSO near zone (Mortlock et al. 2011; Bolton et al. 2011), respectively. The hatched and gray regions represent the 1σ ranges for the instantaneous reionization redshifts obtained by nine-year *WMAP* (Hinshaw et al. 2013; Bennett et al. 2013) and *Planck* (Planck Collaboration et al. 2016), respectively. The doted, dashed and solid lines show the models A, B, and C, respectively (Choudhury et al. 2008).

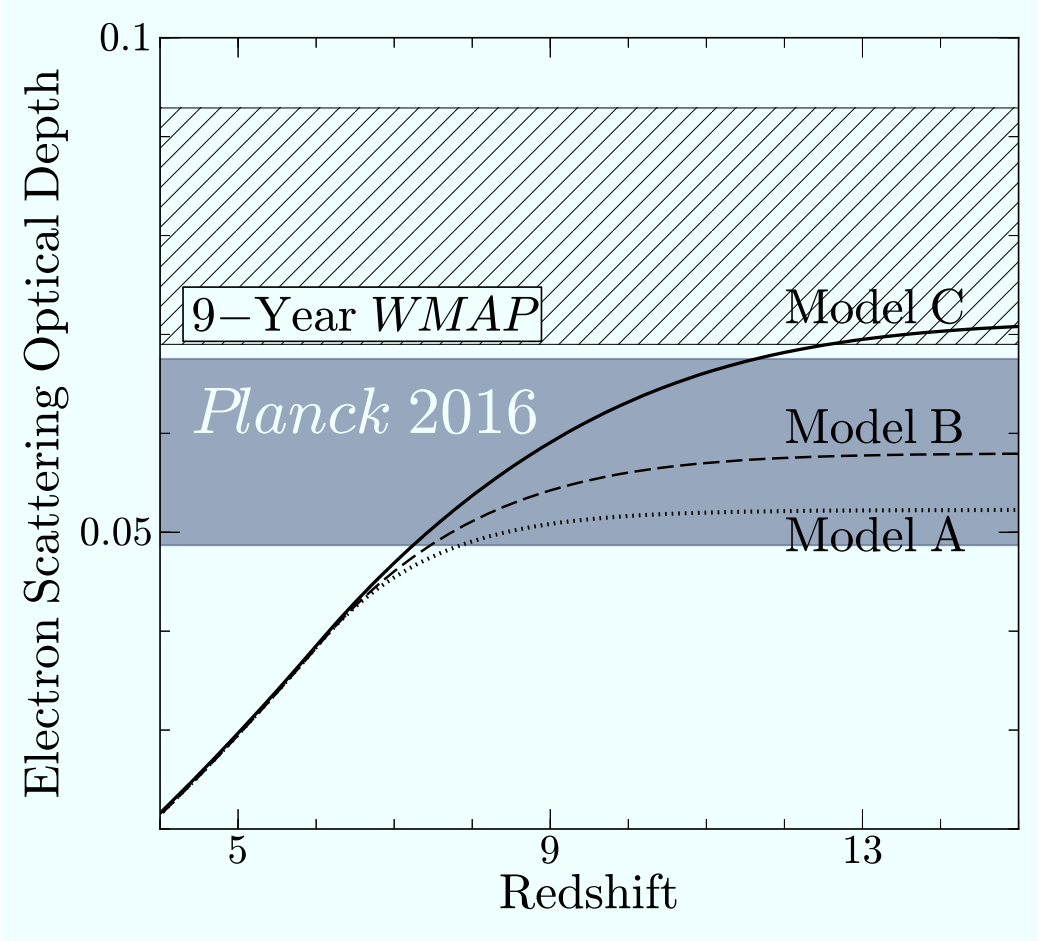

Figure 7.5 Evolution of Thomson scattering optical depth, $\tau_{\rm el}$. The hatched and gray regions indicate the 1σ ranges of the $\tau_{\rm el}$ measurements of $\tau_{\rm el}= 0.081 \pm 0.012$ and $\tau_{\rm el}= 0.058 \pm 0.009$ obtained by nine-year *WMAP* (Hinshaw et al. 2013; Bennett et al. 2013) and the latest *Planck* data (Planck Collaboration et al. 2016), respectively. The doted, dashed, and solid curves represent the models A, B, and C, respectively (Choudhury et al. 2008).

CHAPTER 8
CONCLUSIONS

We have conducted the wide-field (~ 1 deg^2) and ultra-deep Subaru/Suprime-Cam imaging surveys for $z = 2.2$ and 7.3 LAEs with our custom narrowband filters, *NB387* and *NB101*, respectively. To identify $z = 5.7$ and 6.6 LAEs, we have used the Subaru/HSC imaging survey data with the narrowband filters, *NB816* and *NB921*, respectively, whose areas are $\sim 10 - 20$ deg^2. We make the samples consisting 3137, 1081, 1273, and 7 LAEs at $z = 2.2$, 5.7, 6.6, and 7.3, respectively. These samples are the largest ones, to date, and the luminosity ranges of the LAE samples fall in $\log L_{\mathrm{Ly}\alpha}$ [erg s^{-1}] $\sim 42 - 44$.

We firstly list our major results about galaxy evolution below:

1. Using our large $z = 2.2$ LAE sample, we derive the Lyα LFs at $z = 2.2$ with small uncertainties including Poisson statistics and cosmic variance errors (Figure 4.6). We fit a Schechter function to our Lyα LF at $z = 2.2$, and obtain the best-fit Schechter parameters of $L^*_{\mathrm{Ly}\alpha} = 5.29^{+1.67}_{-1.13} \times 10^{42}$ erg s^{-1}, $\phi^*_{\mathrm{Ly}\alpha} = 6.32^{+3.08}_{-2.31} \times 10^{-4}$ Mpc^{-3}, and $\alpha = -1.75^{+0.10}_{-0.09}$ with no priori assumptions in the parameters. We find a steep faint-end slope of the Lyα LF at $z \sim 2$, which is comparable to that of UV-continuum LFs at $z \sim 2$.

2. In our best-estimate Lyα LF at $z = 2.2$, we find a bright-end hump at $\log L_{\mathrm{Ly}\alpha}$ [erg s^{-1}] $\gtrsim 43.4$, where the Lyα LF significantly exceeds beyond the best-fit Schechter function (Figure 4.6). We find that a majority of the LAEs at $\log L_{\mathrm{Ly}\alpha}$ [erg s^{-1}] > 43.4 are detected in the X-ray, UV, or radio band. This result indicates that the bright-end hump is not originated from the gravitational lensing magnification bias, but AGNs. Based on the LAEs in the bright-end hump, we derive the AGN UV-continuum LF at $z \sim 2$ down to the faint magnitude limit of $M_{\mathrm{UV}} \sim -22.5$ (Figure 7.1). We find that our AGN UV LF covers a magnitude range fainter than the previous studies with an overlap at $M_{\mathrm{UV}} \simeq -24.8$, and confirm that our AGN UV LF agrees well with the previous results at the overlap magnitude. Fitting the double-power law function to the AGN UV LF data obtained by our and previous studies, we constrain the faint-end slope of the AGN UV LF at $z \sim 2$, $\alpha_{\mathrm{AGN}} = -1.2 \pm 0.1$, that is flatter than those at $z = 4 - 6.5$ ($\alpha_{\mathrm{AGN}} \simeq -1.5$ - -1.8).

3. We identify a moderate but significant increase of the Lyα LF by a factor of $\lesssim 2$ from $z \sim 2$ to 3 (Figure 5.1). We extend our investigation from $z = 2-3$ to $z = 0-6$ and present the overall evolutionary trends of Lyα LFs: the large increase of the Lyα LFs from $z \sim 0$ to 3, and no evolution of the Lyα LFs at $z \sim 3-6$. A similar evolutional tendency is seen in the Lyα LDs, which are obtained by the integration of these Lyα LFs. This increase of the Lyα LDs from $z \sim 0$ to 3 is significantly faster than the one of UV-continuum LDs (Figure 6.1).

4. We estimate $f_{\rm esc}^{{\rm Ly}\alpha}$ values from the Lyα and UV LDs at $z \sim 0-6$ given by our and previous studies. We find a large $f_{\rm esc}^{{\rm Ly}\alpha}$ increase from $z \sim 0$ to 6 by two orders of magnitude (Figure 6.1). This large $f_{\rm esc}^{{\rm Ly}\alpha}$ increase can be explained neither by stellar population nor outflow because previous studies present no significant evolutions in stellar population and outflow in LAEs at $z \sim 0-6$. Although the dust extinction with no Lyα resonance scattering can partly explain the $f_{\rm esc}^{{\rm Ly}\alpha}$ increase at $z \sim 0-6$, there remains a significantly large discrepancy at $z < 4$. We use uniform expanding shell models, MCLya, based on the average $E(B-V)_{\rm gas}$ values for non-resonance nebular lines estimated with the observational data. Our models suggest that the typical HI column density decreases from $N_{\rm HI} \sim 7 \times 10^{19}$ ($z \sim 0$) to $\sim 1 \times 10^{18}$ cm^{-2} ($z \sim 6$) to explain the large $f_{\rm esc}^{{\rm Ly}\alpha}$ increase (Figure 7.3). Thus, the Lyα resonance scattering in HI ISM is an important effect to explain the large $f_{\rm esc}^{{\rm Ly}\alpha}$ increase.

We secondly list our major results about cosmic reionization below:

1. Fixing the faint-end slope of $\alpha = -1.8$ that is derived from our $z = 2.2$ Lyα LF, we obtain the best-fit Schechter parameters of $L^*_{{\rm Ly}\alpha} = 8.92^{+0.99}_{-0.89} \times 10^{42}$ erg s^{-1} and $\phi^*_{{\rm Ly}\alpha} = 2.21^{+0.68}_{-0.50} \times 10^{-4}$ Mpc^{-3} at $z = 5.7$, and $L^*_{{\rm Ly}\alpha} = 6.42^{+0.74}_{-0.59} \times 10^{42}$ erg s^{-1} and $\phi^*_{{\rm Ly}\alpha} = 2.51^{+0.83}_{-0.68} \times 10^{-4}$ Mpc^{-3} at $z = 6.6$. Comparing our Lyα LFs with these best-fit Schechter functions, we find that a bright-end hump at $\log L^*_{{\rm Ly}\alpha}$ [erg s^{-1}] $\gtrsim 43.5$ can be seen at $z = 6.6$, although there is no significant hump found in our $z = 5.7$ Lyα LF (Figure 5.2). These results indicate that LAEs brighter than $\log L^*_{{\rm Ly}\alpha}$ [erg s^{-1}] $\gtrsim 43.5$ are AGNs, which is the same conclusion as the bright-end hump found in our $z = 2.2$ Lyα LF. Another possibility is the emergence of large ionized bubbles in the IGM around bright LAEs, which

allow Lyα photons to escape from the partly ionized IGM at EoR. Because faint LAEs reside in small-size ionized bubbles in the IGM, Lyα photons from faint LAEs suffer the Lyα damping wing absorption. This causes the decrease of the faint-end Lyα LF at $z = 6.6$.

2. Although we expect to find a total of ~ 65 LAEs at $z = 7.3$ by our survey in the case of no evolution of Lyα LF from $z = 6.6$ to 7.3, we detect only seven LAEs at $z = 7.3$. We derive the Lyα LF at $z = 7.3$ with our data, carefully evaluating uncertainties of Poisson statistics and cosmic variance from the two independent blank fields (Figure 4.9). We fit the Schechter functions to our Lyα LF, and obtain the best-fit Schechter parameters, $L^*_{\rm Ly\alpha} = 3.23^{+25.0}_{-1.63} \times 10^{42}$ erg s^{-1} and $\phi^* = 1.97^{+12.3}_{-1.89} \times 10^{-4}$ Mpc^{-3} with the fixed $\alpha = -1.8$. We compare our Lyα LF with the previous measurements of the Lyα LF at $z \simeq 7.3$. Our Lyα LF measurements are consistent with those of the previous Subaru and VLT studies, but significantly smaller than those of the 4m-telescope observations (Figure 4.10). The significant differences of the Lyα LFs between the 4m-telescope programs and Subaru+VLT studies including ours could not be explained by cosmic variance. It is possible that the 4m-telescope results are derived with the highly contaminated LAE samples, as suggested by the recent spectroscopic follow-up observations that find no emission lines in the LAEs of the 4m-telescope samples.

3. We confirm the decreases of the Lyα LFs at $z = 5.7 - 6.6$ and $6.6 - 7.3$ at the $> 90\%$ confidence level (Figure 5.3). Using our Lyα LFs at $z = 5.7 - 7.3$, we find the rapid decrease of the Lyα LF indicated by the evolution of the Lyα LD ratios (Figure 6.2). Approximating the evolution of the Lyα LDs with the power-law function, $(1 + z)^k$, we obtain $k = -2.2 \pm 0.2$ at $z = 5.7 - 6.6$ and $k = -12.9 \pm 12.4$ at $z = 6.6 - 7.3$. These results indicate that there is the accelerated evolution of the Lyα LF at $z \gtrsim 7$, although these values of k are consistent within the uncertainties

4. Because no accelerated evolution of the UV-continuum LF or the cosmic star-formation rate (SFR) is found at $z \sim 7$, this accelerated Lyα LF evolution is not explained by the SFR decreases of galaxies, but related to the Lyα production and escape in the process of cosmic reionization. We discuss the simple scenario

of cosmic reionization that contributes to the accelerated evolution of the Lyα LF. Subtracting the galaxies' SFR evolution effect from the Lyα LD decrease, we estimate the ratio of Lyα transmission of the IGM to be $T^{\rm IGM}_{{\rm Ly}\alpha,z=6.6}/T^{\rm IGM}_{{\rm Ly}\alpha,z=5.7} = 1.0$ and $T^{\rm IGM}_{{\rm Ly}\alpha,z=7.3}/T^{\rm IGM}_{{\rm Ly}\alpha,z=5.7} = 0.34$. By the comparison of theoretical models, we obtain $x_{\rm HI} = 0.0-0.3$ and $0.3-0.8$ at $z = 6.6$ and 7.3, respectively, whose large uncertainties include the variance of the theoretical model predictions. These results are consistent with previous $z \sim 7$ studies that use the Lyα damping wing absorption. The $x_{\rm HI}$ evolution can explain the Thomson scattering optical depth measurements from the latest *Planck* 2016 data. This suggests that the physical origin of the accelerated Lyα LF evolution would be the rapid increase of $x_{\rm HI}$ at $z \gtrsim 7$, albeit with $\sim 30\%$ level uncertainties for the $x_{\rm HI}$ determinations.

REFERENCES

Adams, J. J., Blanc, G. A., Hill, G. J., et al. 2011, ApJS, 192, 5

Ajiki, M., Mobasher, B., Taniguchi, Y., et al. 2006, ApJ, 638, 596

Alavi, A., Siana, B., Richard, J., et al. 2014, ApJ, 780, 143

Alexander, D. M., Bauer, F. E., Brandt, W. N., et al. 2003, AJ, 126, 539

Atek, H., Schaerer, D., & Kunth, D. 2009, A&A, 502, 791

Atek, H., Kunth, D., Schaerer, D., et al. 2014, A&A, 561, A89

Axelrod, T., Kantor, J., Lupton, R. H., et al. 2010, Proc. SPIE, 7740, 774015

Bardeen, J. M., Bond, J. R., Kaiser, N., et al. 1986, ApJ, 304, 15

Barger, A. J., Cowie, L. L., & Wold, I. G. B. 2012, ApJ, 749, 106

Bennett, C. L., Larson, D., Weiland, J. L., et al. 2013, ApJS, 208, 20

Bertin, E. & Arnouts, S. 1996, A&AS, 117, 393

Blanc, G. A., Adams, J. J., Gebhardt, K., et al. 2011, ApJ, 736, 31

Bohlin, R. C., Colina, L., & Finley, D. S. 1995, AJ, 110, 1316

Bolton, J. S., Haehnelt, M. G., Warren, S. J., et al. 2011, MNRAS, 416, L70

Bolton, J. S. & Haehnelt, M. G. 2013, MNRAS, 429, 1695

Bouwens, R. J., Illingworth, G. D., Franx, M., et al. 2009, ApJ, 705, 936

Bouwens, R. J., Illingworth, G. D., Oesch, P. A., et al. 2011, ApJ, 737, 90

Bouwens, R. J., Illingworth, G. D., Oesch, P. A., et al. 2015, ApJ, 803, 34

Bowler, R. A. A., McLure, R. J., Dunlop, J. S., et al. 2016, ArXiv e-prints, arXiv:1609.00727

Brocklehurst, M. 1971, MNRAS, 153, 471

Bruzual, G. & Charlot, S. 2003, MNRAS, 344, 1000

Calzetti, D., Armus, L., Bohlin, R. C., et al. 2000, ApJ, 533, 682

Capak, P., Cowie, L. L., Hu, E. M., et al. 2004, AJ, 127, 180

Capak, P., Aussel, H., Ajiki, M., et al. 2007, ApJS, 172, 99

Cardamone, C. N., van Dokkum, P. G., Urry, C. M., et al. 2010, ApJS, 189, 270

Carroll, S. M., Press, W. H., & Turner, E. L. 1992, ARA&A, 30, 499

Caruana, J., Bunker, A. J., Wilkins, S. M., et al. 2012, MNRAS, 427, 3055

—. 2014, MNRAS, 443, 2831

Cassata, P., Le Fèvre, O., Garilli, B., et al. 2011, A&A, 525, A143

Cassata, P., Tasca, L. A. M., Le Fèvre, O., et al. 2015, A&A, 573, A24

Choudhury, T. R., Ferrara, A., & Gallerani, S. 2008, MNRAS, 385, L58

Ciardullo, R., Gronwall, C., Wolf, C., et al. 2012, ApJ, 744, 110

Ciardullo, R., Gronwall, C., Adams, J. J., et al. 2013, ApJ, 769, 83

Ciardullo, R., Zeimann, G. R., Gronwall, C., et al. 2014, ApJ, 796, 64

Clément, B., Cuby, J.-G., Courbin, F., et al. 2012, A&A, 538, A66

Cowie, L. L. & Hu, E. M. 1998, AJ, 115, 1319

Cowie, L. L., Barger, A. J., & Hu, E. M. 2010, ApJ, 711, 928

—. 2011, ApJ, 738, 136

Croom, S. M., Richards, G. T., Shanks, T., et al. 2009, MNRAS, 399, 1755

Cuby, J.-G., Hibon, P., Lidman, C., et al. 2007, A&A, 461, 911

Dawson, S., Rhoads, J. E., Malhotra, S., et al. 2007, ApJ, 671, 1227

Deharveng, J.-M., Small, T., Barlow, T. A., et al. 2008, ApJ, 680, 1072

de Vries, W. H., Becker, R. H., White, R. L., et al. 2005, AJ, 129, 615

Dietrich, M., Hamann, F., Shields, J. C., et al. 2002, ApJ, 581, 912

Dijkstra, M., Lidz, A., & Wyithe, J. S. B. 2007a, MNRAS, 377, 1175

Dijkstra, M., Wyithe, J. S. B., & Haiman, Z. 2007b, MNRAS, 379, 253

Dijkstra, M., Wyithe, S., Haiman, Z., et al. 2014, MNRAS, 440, 3309

Ellis, R. S., McLure, R. J., Dunlop, J. S., et al. 2013, ApJ, 763, L7

Elvis, M., Civano, F., Vignali, C., et al. 2009, ApJS, 184, 158

Erb, D. K., Steidel, C. C., Trainor, R. F., et al. 2014, ApJ, 795, 33

Faisst, A. L., Capak, P., Carollo, C. M., et al. 2014, ApJ, 788, 87

Fan, X., Strauss, M. A., Becker, R. H., et al. 2006, AJ, 132, 117

Finkelstein, S. L., Rhoads, J. E., Malhotra, S., et al. 2009, ApJ, 691, 465

Fiore, F., Puccetti, S., Grazian, A., et al. 2012, A&A, 537, A16

Furlanetto, S. R., Zaldarriaga, M., & Hernquist, L. 2006, MNRAS, 365, 1012

Furusawa, H., Kosugi, G., Akiyama, M., et al. 2008, ApJS, 176, 1

Gawiser, E., van Dokkum, P. G., Gronwall, C., et al. 2006, ApJ, 642, L13

Gehrels, N. 1986, ApJ, 303, 336

Giacconi, R., Rosati, P., Tozzi, P., et al. 2001, ApJ, 551, 624

Giallongo, E., Grazian, A., Fiore, F., et al. 2015, A&A, 578, A83

Gronke, M., Dijkstra, M., Trenti, M., et al. 2015, MNRAS, 449, 1284

Grogin, N. A., Kocevski, D. D., Faber, S. M., et al. 2011, ApJS, 197, 35

Gronwall, C., Ciardullo, R., Hickey, T., et al. 2007, ApJ, 667, 79

Guaita, L., Gawiser, E., Padilla, N., et al. 2010, ApJ, 714, 255

Guaita, L., Acquaviva, V., Padilla, N., et al. 2011, ApJ, 733, 114

Gunn, J. E. & Peterson, B. A. 1965, ApJ, 142, 1633

Gunn, J. E. & Stryker, L. L. 1983, ApJS, 52, 121

Haardt, F., & Madau, P. 2012, ApJ, 746, 125

Haiman, Z. 2002, ApJ, 576, L1

Hashimoto, T., Ouchi, M., Shimasaku, K., et al. 2013, ApJ, 765, 70

Hashimoto, T., Verhamme, A., Ouchi, M., et al. 2015, ApJ, 812, 157

Hathi, N. P., Ryan, Jr., R. E., Cohen, S. H., et al. 2010, ApJ, 720, 1708

Hayashino, T., Matsuda, Y., Tamura, H., et al. 2004, AJ, 128, 2073

Hayes, M., Östlin, G., Schaerer, D., et al. 2010, Nature, 464, 562

Hayes, M., Schaerer, D., Östlin, G., et al. 2011, ApJ, 730, 8

Hayes, M., Östlin, G., Duval, F., et al. 2014, ApJ, 782, 6

Hayes, M. 2015, PASA, 32, e027

Hibon, P., Cuby, J.-G., Willis, J., et al. 2010, A&A, 515, A97

Hildebrandt, H., Erben, T., Dietrich, J. P., et al. 2006, A&A, 452, 1121

Hinshaw, G., Larson, D., Komatsu, E., et al. 2013, ApJS, 208, 19

Hopkins, P. F., Hernquist, L., Cox, T. J., et al. 2006, ApJ, 639, 700

Hu, E. M., Cowie, L. L., & McMahon, R. G. 1998, ApJ, 502, L99

Hu, E. M., Cowie, L. L., Capak, P., et al. 2004, AJ, 127, 563

Hu, E. M., Cowie, L. L., Capak, P., et al. 2005, in IAU Colloq. 199: Probing Galaxies through Quasar Absorption Lines, ed. P. Williams, C.-G. Shu, & B. Menard, 363–368

Hu, E. M., Cowie, L. L., Barger, A. J., et al. 2010, ApJ, 725, 394

Ikeda, H., Nagao, T., Matsuoka, K., et al. 2011, ApJ, 728, L25

Inoue, A. K., Iwata, I., & Deharveng, J.-M. 2006, MNRAS, 371, L1

Inoue, A. K., Shimizu, I., Iwata, I., et al. 2014, MNRAS, 442, 1805

Inoue, A. K., Tamura, Y., Matsuo, H., et al. 2016, Science, 352, 1559

Ivezic, Z., Tyson, J. A., Abel, B., et al. 2008, ArXiv e-prints, arXiv:0805.2366

Iye, M., Ota, K., Kashikawa, N., et al. 2006, Nature, 443, 186

Jiang, L., Fan, X., Cool, R. J., et al. 2006, AJ, 131, 2788

Jiang, L., Bian, F., Fan, X., et al. 2013, ApJ, 771, L6

Jiang, L., McGreer, I. D., Fan, X., et al. 2016, ApJ, 833, 222

Jones, T., Stark, D. P., & Ellis, R. S. 2012, ApJ, 751, 51

Jurić, M., Kantor, J., Lim, K., et al. 2015, ArXiv e-prints, arXiv:1512.07914

Kakiichi, K., Dijkstra, M., Ciardi, B., et al. 2016, MNRAS, 463, 4019

Kamata, Y., Miyazaki, S., Nakaya, H., et al. 2008, in Society of Photo-Optical Instrumentation Engineers (SPIE) Conference Series, Vol. 7021, Society of Photo-Optical Instrumentation Engineers (SPIE) Conference Series

Kashikawa, N., Shimasaku, K., Malkan, M. A., et al. 2006, ApJ, 648, 7

Kashikawa, N., Shimasaku, K., Matsuda, Y., et al. 2011, ApJ, 734, 119

Kashikawa, N., Nagao, T., Toshikawa, J., et al. 2012, ApJ, 761, 85

Kashikawa, N., Ishizaki, Y., Willott, C. J., et al. 2015, ApJ, 798, 28

Kennicutt, Jr., R. C. 1998, ApJ, 498, 541

Kinney, A. L., Calzetti, D., Bohlin, R. C., et al. 1996, ApJ, 467, 38

Koekemoer, A. M., Faber, S. M., Ferguson, H. C., et al. 2011, ApJS, 197, 36

Kornei, K. A., Shapley, A. E., Erb, D. K., et al. 2010, ApJ, 711, 693

Krug, H. B., Veilleux, S., Tilvi, V., et al. 2012, ApJ, 745, 122

Kudritzki, R. P., Méndez, R. H., Feldmeier, J. J., et al. 2000, ApJ, 536, 19

Kusakabe, H., Shimasaku, K., Nakajima, K., et al. 2015, ApJ, 800, L29

Lai, K., Huang, J.-S., Fazio, G., et al. 2008, ApJ, 674, 70

Lawrence, A., Warren, S. J., Almaini, O., et al. 2007, MNRAS, 379, 1599

Madau, P. 1995, ApJ, 441, 18

Madau, P., Pozzetti, L., & Dickinson, M. 1998, ApJ, 498, 106

Magnier, E. A., Schlafly, E., Finkbeiner, D., et al. 2013, ApJS, 205, 20

Malhotra, S. & Rhoads, J. E. 2002, ApJ, 565, L71

Malhotra, S. & Rhoads, J. E. 2004, ApJ, 617, L5

Mason, C. A., Treu, T., Schmidt, K. B., et al. 2015, ApJ, 805, 79

Matsuda, Y., Yamada, T., Hayashino, T., et al. 2004, AJ, 128, 569

Matsuoka, Y., Onoue, M., Kashikawa, N., et al. 2016, ApJ, 828, 26

Matthee, J. J. A., Sobral, D., Swinbank, A. M., et al. 2014, MNRAS, 440, 2375

Matthee, J., Sobral, D., Santos, S., et al. 2015, MNRAS, 451, 400

Matthee, J., Sobral, D., Oteo, I., et al. 2016, MNRAS, 458, 449

McCracken, H. J., Capak, P., Salvato, M., et al. 2010, ApJ, 708, 202

McQuinn, M., Hernquist, L., Zaldarriaga, M., et al. 2007, MNRAS, 381, 75

Meurer, G. R., Heckman, T. M., & Calzetti, D. 1999, ApJ, 521, 64

Miller, N. A., Bonzini, M., Fomalont, E. B., et al. 2013, ApJS, 205, 13

Miralda-Escudé, J. 1998, ApJ, 501, 15

Miyazaki, S., Komiyama, Y., Sekiguchi, M., et al. 2002, PASJ, 54, 833

Miyazaki, S., Komiyama, Y., Nakaya, H., et al. 2012, Proc. SPIE, 8446, 84460Z

Mo, H. J. & White, S. D. M. 2002, MNRAS, 336, 112

Mortlock, D. J., Warren, S. J., Venemans, B. P., et al. 2011, Nature, 474, 616

Murayama, T., Taniguchi, Y., Scoville, N. Z., et al. 2007, ApJS, 172, 523

Nakajima, K., Ouchi, M., Shimasaku, K., et al. 2012, ApJ, 745, 12

—. 2013, ApJ, 769, 3

Nakajima, K. & Ouchi, M. 2014, MNRAS, 442, 900

Nakamura, E., Inoue, A. K., Hayashino, T., et al. 2011, MNRAS, 412, 2579

Nilsson, K. K., Tapken, C., Møller, P., et al. 2009, A&A, 498, 13

Nonino, M., Dickinson, M., Rosati, P., et al. 2009, ApJS, 183, 244

Oesch, P. A., Bouwens, R. J., Carollo, C. M., et al. 2010, ApJ, 725, L150

Oesch, P. A., Bouwens, R. J., Illingworth, G. D., et al. 2013, ApJ, 773, 75

Oesch, P. A., van Dokkum, P. G., Illingworth, G. D., et al. 2015, ApJ, 804, L30

Oke, J. B. 1974, ApJS, 27, 21

—. 1990, AJ, 99, 1621

Ono, Y., Ouchi, M., Shimasaku, K., et al. 2010a, ApJ, 724, 1524

—. 2010b, MNRAS, 402, 1580

Ono, Y., Ouchi, M., Mobasher, B., et al. 2012, ApJ, 744, 83

Ono, Y., Ouchi, M., Kurono, Y., et al. 2014, ApJ, 795, 5

Ota, K., Iye, M., Kashikawa, N., et al. 2008, ApJ, 677, 12

—. 2010, ApJ, 722, 803

Ouchi, M., Shimasaku, K., Furusawa, H., et al. 2003, ApJ, 582, 60

Ouchi, M., Shimasaku, K., Okamura, S., et al. 2004, ApJ, 611, 660

Ouchi, M., Shimasaku, K., Akiyama, M., et al. 2008, ApJS, 176, 301

Ouchi, M., Mobasher, B., Shimasaku, K., et al. 2009, ApJ, 706, 1136

Ouchi, M., Shimasaku, K., Furusawa, H., et al. 2010, ApJ, 723, 869

Pardy, S. A., Cannon, J. M., Östlin, G., et al. 2014, ApJ, 794, 101

Parsa, S., Dunlop, J. S., McLure, R. J., et al. 2016, MNRAS, 456, 3194

Partridge, R. B. & Peebles, P. J. E. 1967, ApJ, 147, 868

Pentericci, L., Grazian, A., Fontana, A., et al. 2007, A&A, 471, 433

Pentericci, L., Fontana, A., Vanzella, E., et al. 2011, ApJ, 743, 132

Pentericci, L., Vanzella, E., Fontana, A., et al. 2014, ApJ, 793, 113

Pirzkal, N., Malhotra, S., Rhoads, J. E., et al. 2007, ApJ, 667, 49

Planck Collaboration et al. 2015, ArXiv e-prints, arXiv:1502.01589

Planck Collaboration et al. 2016, ArXiv e-prints, arXiv:1605.02985

Polletta, M., Tajer, M., Maraschi, L., et al. 2007, ApJ, 663, 81

Rauch, M., Haehnelt, M., Bunker, A., et al. 2008, ApJ, 681, 856

Reddy, N. A. & Steidel, C. C. 2009, ApJ, 692, 778

Rhoads, J. E., Malhotra, S., Dey, A., et al. 2000, ApJ, 545, L85

Rhoads, J. E., & Malhotra, S. 2001, ApJ, 563, L5

Rivera-Thorsen, T. E., Hayes, M., Östlin, G., et al. 2015, ApJ, 805, 14

Robertson, B. E., Ellis, R. S., Dunlop, J. S., et al. 2010, Nature, 468, 49

Robertson, B. E., Furlanetto, S. R., Schneider, E., et al. 2013, ApJ, 768, 71

Ross, N. P., McGreer, I. D., White, M., et al. 2013, ApJ, 773, 14

Santos, M. R., Ellis, R. S., Kneib, J.-P., et al. 2004, ApJ, 606, 683

Santos, M. R. 2004, MNRAS, 349, 1137

Santos, S., Sobral, D., & Matthee, J. 2016, MNRAS,

Sawicki, M. 2012, MNRAS, 421, 2187

Schaerer, D., Hayes, M., Verhamme, A., et al. 2011, A&A, 531, A12

Schechter, P. 1976, ApJ, 203, 297

Schenker, M. A., Stark, D. P., Ellis, R. S., et al. 2012, ApJ, 744, 179

Schenker, M. A., Ellis, R. S., Konidaris, N. P., et al. 2014, ApJ, 795, 20

Schiminovich, D., Ilbert, O., Arnouts, S., et al. 2005, ApJ, 619, L47

Schinnerer, E., Smolčić, V., Carilli, C. L., et al. 2007, ApJS, 172, 46

Schlafly, E. F., Finkbeiner, D. P., Jurić, M., et al. 2012, ApJ, 756, 158

Schlegel, D. J., Finkbeiner, D. P., & Davis, M. 1998, ApJ, 500, 525

Scoville, N., Aussel, H., Brusa, M., et al. 2007, ApJS, 172, 1

Shapley, A. E., Steidel, C. C., Pettini, M., et al. 2003, ApJ, 588, 65

Shibuya, T., Kashikawa, N., Ota, K., et al. 2012, ApJ, 752, 114

Shibuya, T., Ouchi, M., Nakajima, K., et al. 2014, ApJ, 788, 74

Shibuya, T., Ouchi, M., & Harikane, Y. 2015, ApJS, 219, 15

Shimasaku, K., Kashikawa, N., Doi, M., et al. 2006, PASJ, 58, 313

Simpson, C., Martínez-Sansigre, A., Rawlings, S., et al. 2006, MNRAS, 372, 741

Sobral, D., Best, P. N., Geach, J. E., et al. 2009, MNRAS, 398, L68

Sobral, D., Smail, I., Best, P. N., et al. 2013, MNRAS, 428, 1128

Sobral, D., Matthee, J., Darvish, B., et al. 2015, ApJ, 808, 139

Song, M., Finkelstein, S. L., Gebhardt, K., et al. 2014, ApJ, 791, 3

Stark, D. P., Ellis, R. S., Chiu, K., et al. 2010, MNRAS, 408, 1628

Stark, D. P., Richard, J., Charlot, S., et al. 2015, MNRAS, 450, 1846

Steidel, C. C., Adelberger, K. L., Shapley, A. E., et al. 2000, ApJ, 532, 170

Taniguchi, Y., Ajiki, M., Nagao, T., et al. 2005, PASJ, 57, 165

Tapken, C., Appenzeller, I., Gabasch, A., et al. 2006, A&A, 455, 145

Tilvi, V., Rhoads, J. E., Hibon, P., et al. 2010, ApJ, 721, 1853

Tonry, J. L., Stubbs, C. W., Lykke, K. R., et al. 2012, ApJ, 750, 99

Totani, T., Kawai, N., Kosugi, G., et al. 2006, PASJ, 58, 485

Totani, T., Aoki, K., Hattori, T., et al. 2014, PASJ, 66, 63

Treu, T., Trenti, M., Stiavelli, M., et al. 2012, ApJ, 747, 27

Treu, T., Schmidt, K. B., Trenti, M., et al. 2013, ApJ, 775, L29

Ueda, Y., Watson, M. G., Stewart, I. M., et al. 2008, ApJS, 179, 124

van Breukelen, C., Jarvis, M. J., & Venemans, B. P. 2005, MNRAS, 359, 895

van Dokkum, P. G. 2001, PASP, 113, 1420

Verhamme, A., Schaerer, D., & Maselli, A. 2006, A&A, 460, 397

Verhamme, A., Schaerer, D., Atek, H., et al. 2008, A&A, 491, 89

Wang, J. X., Malhotra, S., Rhoads, J. E., et al. 2009, ApJ, 706, 762

Willis, J. P. & Courbin, F. 2005, MNRAS, 357, 1348

Willis, J. P., Courbin, F., Kneib, J. P., et al. 2008, MNRAS, 384, 1039

Willott, C. J., Delorme, P., Reylé, C., et al. 2010, AJ, 139, 906

Wofford, A., Leitherer, C., & Salzer, J. 2013, ApJ, 765, 118

Wold, I. G. B., Barger, A. J., & Cowie, L. L. 2014, ApJ, 783, 119

Wyithe, J. S. B., Yan, H., Windhorst, R. A., et al. 2011, Nature, 469, 181

Xu, Y., Yue, B., Su, M., et al. 2014, ApJ, 781, 97

Xue, Y. Q., Luo, B., Brandt, W. N., et al. 2011, ApJS, 195, 10

Yagi, M., Kashikawa, N., Sekiguchi, M., et al. 2002, AJ, 123, 66

Yamada, T., Nakamura, Y., Matsuda, Y., et al. 2012, AJ, 143, 79

Zamojski, M. A., Schiminovich, D., Rich, R. M., et al. 2007, ApJS, 172, 468

Zitrin, A., Labbé, I., Belli, S., et al. 2015, ApJ, 810, L12

Zheng, Z.-Y., Finkelstein, S. L., Finkelstein, K., et al. 2013, MNRAS, 431, 3589